



JOINT DECODING OF PARALLEL POWER LINE COMMUNICATION AND VISIBLE LIGHT COMMUNICATION SYSTEMS

A dissertation submitted to the Faculty of Engineering and the Built Environment,
University of the Witwatersrand, in fulfilment of the requirements for the degree of
Master of Science in Engineering

Daniel Obinna Onwuatuelo

June 7, 2018

Declaration

I declare that except where due acknowledgment has been made, this dissertation is my own unaided work. It is being submitted for the Degree of Master of Science to the University of the Witwatersrand, Johannesburg. It has not been submitted before for any degree or examination to any other University.

.....

..... day of year

Abstract

Many indoor applications operate at narrowband (3 kHz - 148.5 kHz) speed and for such applications, power line communication (PLC) and visible light communication (VLC) networks can be naturally connected and adapted to complement each other in order to gain more overall system performance in terms of bit error rate (BER) and computational complexity. In this research, the joint decoding of parallel PLC and VLC systems is proposed and its BER performance is compared to that of the PLC and the VLC systems. The joint decoding is applied either at the inner (Viterbi) or at the outer (Reed-Solomon) decoder. The proposed system is adopted according to the PLC G3 physical layer specification but direct current optical orthogonal frequency division multiplexing OFDM (DCO-OFDM) is used in the VLC system to ensure that only positive (unipolar) signals are transmitted. A realistic VLC channel model is adopted in this research by considering the VLC channel as an additive white Gaussian noise (AWGN) channel affected by attenuation in terms of angle of orientation between the source and the receiver and effective surface area of the receiver. Furthermore, the PLC channel is modeled as an AWGN channel with background and impulsive noise generated using Middleton Class-A noise distribution model. It is shown through simulation results and analysis that the proposed joint decoded system outperforms the PLC and the VLC systems in terms of BER performance depending on the distance of separation between the source and the receiver.

Key words: Power line communication (PLC), Visible light communication (VLC), Bit error rate (BER), Joint decoding, Orthogonal frequency division multiplexing (OFDM), DC optical OFDM (DCO-OFDM), Additive white Gaussian noise (AWGN).

Dedication

*This dissertation is dedicated to my family and in loving memory of my
brother Deo-Gratias Ekene Onwuatuolo*

Acknowledgments

First of all, I would like to thank the Almighty God for giving me the strength, patience and perseverance to complete my studies and write this dissertation.

It is my pleasure to thank those who made this dissertation possible. I would like to express my deepest gratitude to my supervisor Professor Ling Cheng for his support, guidance and trust through my candidature at the University. He always made himself available and his energy and enthusiasm in research have been a major source of motivation. My sincere appreciation is extended to Professor T.G. Swart who was my co-supervisor through my candidature. His knowledge, attention to details and priceless advice have contributed immensely in completing my studies. I would also like to express my thanks and appreciation to Dr. Thokozani Shongwe, Dr. Richard Ndjiongue and Dr. Familua Kunle for their unlimited support and help whenever I reached out to them.

Special thanks to my friends and colleagues in the school of Electrical and Information Engineering at the University of the Witwatersrand. I am sincerely thankful to Femi Kolade, Seyi Babalola and Frans Shafuda. Their support and constructive discussions have certainly contributed to the completion of this work and it has been a pleasure to know each and every one of them. Special thanks to Femi Kolade reviewing and editing my dissertation.

The staff at the School of Electrical and Information Engineering (EIE) at the University of the Witwatersrand have been very helpful and cooperative. I would like to thank them all for their kindness and friendliness.

Last but certainly not the least, my deepest and most sincere thanks to my parents and my family for their invaluable and unconditional support, patience and advice which undoubtedly helped me to complete my studies.

Contents

List of Figures	ix
List of Tables	xiii
List of Symbols and Abbreviations	xiv
1 INTRODUCTION	1
1.1 Power Line and Visible Light Communications	1
1.1.1 Power Line Communications	1
1.1.2 Visible Light Communications	2
1.1.3 Integration of Power Line and Visible Light Communications	3
1.2 Joint Decoding Technique	4
1.3 Problem Statement	5
1.4 Research Objective	6
1.4.1 Research Question	7
1.4.2 Research Aims	7
1.5 Research Contributions	8
1.6 Layout of the Dissertation	9
1.7 Summary	11
2 LITERATURE REVIEW	12
2.1 Introduction	12
2.2 Application of Joint Decoding	13
2.3 Combination of PLC and Wireless Systems	14
2.4 Combination of PLC and VLC Systems	18
2.5 Summary	19
3 SYSTEM MODEL	21
3.1 Introduction	21
3.2 Parallel PLC-VLC System	22
3.3 PLC G3 Model	23
3.4 FEC Encoder and Decoder	26
3.4.1 Frame Control Header	28
3.4.2 Scrambler	29

3.4.3	Reed-Solomon Encoder	29
3.4.4	Convolutional Encoder	31
3.4.4.1	State Diagram Representation	32
3.4.4.2	Tree Diagram Representation	34
3.4.4.3	Trellis Diagram Representation	35
3.4.5	Interleaver	36
3.5	OFDM System	37
3.5.1	Binary Phase Shift Keying	39
3.5.2	DCO-OFDM System	41
3.6	The Impulsive Noise Model for PLC Channel	42
3.7	The LOS Propagation Model for VLC Channel	46
3.7.1	LOS Propagation Model	47
3.7.2	SNR Analysis	50
3.8	Summary	52
4	JOINT DECODING SCHEME	53
4.1	Introduction	53
4.2	Benchmark Decoding Scheme	54
4.3	Joint Decoding	54
4.3.1	Joint Decoding at the Convolutional Decoder	55
4.3.2	Joint Decoding at the Reed-Solomon Decoder	56
4.4	Hard Decision Decoding of Convolutional Code	58
4.5	Soft Decision Decoding of Convolutional Code	65
4.6	Hard Decision Decoding of Reed-Solomon Code	70
4.6.1	Syndrome Computation	72
4.6.2	Berlekamp-Massey Algorithm	73
4.6.3	Chien search Algorithm and Error Correction	76
4.7	Erasure Decoding of Reed-Solomon Code	79
4.8	Joint Decoding Scenarios	83
4.9	Summary	86
5	SIMULATION RESULTS AND ANALYSIS	87
5.1	Introduction	87
5.2	BPSK Modulation Scheme	90
5.3	Convolutional and Reed-Solomon Codes	90
5.4	PLC and VLC Channels	91
5.5	Joint Soft Decision Decoding Technique at Different Angles of Orientation	94
5.6	Joint Soft Decision Decoding Technique at Different Effective Receiver Areas	95
5.7	Joint Hard Decision Decoding Technique at Different Angles of Orientation	97
5.8	Joint Hard Decision Decoding Technique at Different Effective Receiver Areas	106
5.9	BER Analysis	115
5.9.1	Decoded BER calculations for the convolutional decoder	116
5.9.2	Decoded BER calculations for the Reed-Solomon decoder	117

5.9.3 Decoded BER calculations for the Joint decoded system	118
5.10 Decoding Complexity Analysis	119
5.10.1 Decoding complexity of the convolutional decoder	119
5.10.2 Decoding complexity of the Reed-Solomon decoder	121
5.11 Summary	122
6 CONCLUSIONS AND FUTURE WORK	124
6.1 Summary of Results	124
6.2 Recommendations for Future Work	128
Bibliography	130

List of Figures

1.1	Indoor visible light communication courtesy of [1]	6
2.1	Wireless-PLC communication using modulation diversity [2]	16
2.2	Wireless-PLC communication using coding diversity [3]	17
3.1	Parallel PLC-VLC system model with OFDM over PLC channel and DCO-OFDM over VLC channel	22
3.2	Transmission system model according to PLC G3 specification [4]	23
3.3	Components of an FEC encoder [4]	27
3.4	Components of an FEC decoder [4]	27
3.5	Data scrambler [4]	29
3.6	A convolutional encoder with $k = 1$, $n = 2$ and $r = 1/2$ [5]	32
3.7	State diagram of a convolutional encoder with $k = 1$, $n = 2$ and $r = 1/2$ [6]	33
3.8	Tree diagram of a convolutional encoder with $k = 1$, $n = 2$ and $r = 1/2$ [7]	35
3.9	Trellis diagram for a 4-state convolutional encoder [8]	36
3.10	Components of an OFDM modulator [3]	38
3.11	Components of an OFDM demodulator [9]	38
3.12	Binary information representation using BPSK modulation scheme [10]	40
3.13	DCO-OFDM system [11]	42
3.14	Middleton Class-A model for two-state PLC channel [12]	44
3.15	Optical intensity direct detection communication channel [13]	46
3.16	Equivalent diagram of VLC channel model using IM/DD [13]	46
3.17	LOS propagation model [14]	49
4.1	Block diagram of separate decoding	54
4.2	Block diagram of joint soft decoding technique at the convolutional decoder	56
4.3	Block diagram of joint hard decoding technique at the convolutional decoder	56
4.4	Block diagram of joint hard decoding technique at the Reed-Solomon decoder	57
4.5	Viterbi decoding - step 1 [15]	61
4.6	Viterbi decoding - step 2 [15]	61
4.7	Viterbi decoding - step 3 [15]	62
4.8	Viterbi decoding - step 4 [15]	62
4.9	Viterbi decoding - step 4, after discarding [15]	63
4.10	Viterbi decoding - step 5, after discarding [15]	63

4.11 Viterbi decoding - step 6, after discarding [15]	64
4.12 Viterbi decoding - step 7 [15]	64
4.13 Signal representation of bits 0 and 1 [16]	65
4.14 (a) Noise of S/N = 2 and (b) Noise of S/N = 4 spread out to spill energy from one decision region to another [6]	66
4.15 Creating four regions for decoding decision [6]	67
4.16 Q-function for determining the probabilities of a normally distributed variable [17]	68
4.17 Reed-Solomon Decoder [18]	71
4.18 Application of joint decoding technique at either Reed-Solomon or convolutional decoder	85
5.1 BPSK modulation over AWGN channel	90
5.2 Effect of (255,239) Reed-Solomon, (7,[133 171]) convolutional and concatenated (255,239) Reed-Solomon and (7,[133 171]) convolutional coding on BPSK system over AWGN channel	91
5.3 BER vs. distance for PLC channel and VLC channel for different angles of orientation between the source and the receiver using concatenated (255,239) Reed-Solomon and (7,[133 171]) convolutional code and BPSK modulation scheme	92
5.4 BER vs. distance for PLC channel and VLC channel for different effective receiver areas using concatenated (255,239) Reed-Solomon and (7,[133 171]) convolutional code and BPSK modulation scheme	92
5.5 The joint soft decision decoding technique is performed at the convolutional decoder with the Reed-Solomon decoder removed for $\theta = 0^\circ$	94
5.6 The joint soft decision decoding technique is performed at the convolutional decoder with the Reed-Solomon decoder removed for $\theta = 10^\circ$	94
5.7 The joint soft decision decoding technique is performed at the convolutional decoder with the Reed-Solomon decoder removed for $\theta = 15^\circ$	95
5.8 The joint soft decision decoding technique is performed at the convolutional decoder with the Reed-Solomon decoder removed for $A = 1 \text{ mm}^2$	96
5.9 The joint soft decision decoding technique is performed at the convolutional decoder with the Reed-Solomon decoder removed for $A = 0.5 \text{ mm}^2$	96
5.10 The joint soft decision decoding technique is performed at the convolutional decoder with the Reed-Solomon decoder removed for $A = 0.1 \text{ mm}^2$	97
5.11 The joint hard decision decoding technique is performed at the convolutional decoder with the Reed-Solomon decoder removed for $\theta = 0^\circ$	98
5.12 The joint hard decision decoding technique is performed at the convolutional decoder. Output of the convolutional decoder is further decoded at the Reed-Solomon decoder for $\theta = 0^\circ$	98
5.13 The joint hard decision decoding technique is performed at the convolutional decoder. Output of convolutional decoder is further decoded at the Reed-Solomon decoder applying the erasure decoding for $\theta = 0^\circ$	99

5.14	Outputs of the PLC and the VLC channels are decoded individually at the convolutional decoders. Outputs the convolutional decoders are combined and the joint hard decision decoding is performed at the Reed-Solomon decoder for $\theta = 0^\circ$	99
5.15	Outputs of the PLC and the VLC channels are decoded individually at the convolutional decoders. Outputs the convolutional decoders are combined and the joint hard decision decoding is performed at the Reed-Solomon decoder applying the erasure decoding for $\theta = 0^\circ$	100
5.16	The joint hard decision decoding technique is performed at the convolutional decoder with the Reed-Solomon decoder removed for $\theta = 10^\circ$	101
5.17	The joint hard decision decoding technique is performed at the convolutional decoder. Output of the convolutional decoder is further decoded at the Reed-Solomon decoder for $\theta = 10^\circ$	101
5.18	The joint hard decision decoding technique is performed at the convolutional decoder. Output of convolutional decoder is further decoded at the Reed-Solomon decoder applying the erasure decoding for $\theta = 10^\circ$	102
5.19	Outputs of the PLC and the VLC channels are decoded individually at the convolutional decoders. Outputs the convolutional decoders are combined and the joint hard decision decoding is performed at the Reed-Solomon decoder for $\theta = 10^\circ$	102
5.20	Outputs of the PLC and the VLC channels are decoded individually at the convolutional decoders. Outputs the convolutional decoders are combined and the joint hard decision decoding is performed at the Reed-Solomon decoder applying the erasure decoding for $\theta = 10^\circ$	103
5.21	The joint hard decision decoding technique is performed at the convolutional decoder with the Reed-Solomon decoder removed for $\theta = 15^\circ$	103
5.22	The joint hard decision decoding technique is performed at the convolutional decoder. Output of the convolutional decoder is further decoded at the Reed-Solomon decoder for $\theta = 15^\circ$	104
5.23	The joint hard decision decoding technique is performed at the convolutional decoder. Output of convolutional decoder is further decoded at the Reed-Solomon decoder applying the erasure decoding for $\theta = 15^\circ$	104
5.24	Outputs of the PLC and the VLC channels are decoded individually at the convolutional decoders. Outputs the convolutional decoders are combined and the joint hard decision decoding is performed at the Reed-Solomon decoder for $\theta = 15^\circ$	105
5.25	Outputs of the PLC and the VLC channels are decoded individually at the convolutional decoders. Outputs the convolutional decoders are combined and the joint hard decision decoding is performed at the Reed-Solomon decoder applying the erasure decoding for $\theta = 15^\circ$	105
5.26	The joint hard decision decoding technique is performed at the convolutional decoder with the Reed-Solomon decoder removed for $A = 1 \text{ mm}^2$	107
5.27	The joint hard decision decoding technique is performed at the convolutional decoder. Output of the convolutional decoder is further decoded at the Reed-Solomon decoder for $A = 1 \text{ mm}^2$	107

5.28	The joint hard decision decoding technique is performed at the convolutional decoder. Output of the convolutional decoder is further decoded at the Reed-Solomon decoder applying the erasure decoding for $A = 1 \text{ mm}^2$.	108
5.29	Outputs of the PLC and the VLC channels are decoded individually at the convolutional decoders. Outputs the convolutional decoders are combined and the joint hard decision decoding is performed at the Reed-Solomon decoder for $A = 1 \text{ mm}^2$	108
5.30	Outputs of the PLC and the VLC channels are decoded individually at the convolutional decoders. Outputs the convolutional decoders are combined and the joint hard decision decoding is performed at the Reed-Solomon decoder applying the erasure decoding for $A = 1 \text{ mm}^2$	109
5.31	The joint hard decision decoding technique is performed at the convolutional decoder with the Reed-Solomon decoder removed for $A = 0.5 \text{ mm}^2$	110
5.32	The joint hard decision decoding technique is performed at the convolutional decoder. Output of the convolutional decoder is further decoded at the Reed-Solomon decoder for $A = 0.5 \text{ mm}^2$	111
5.33	The joint hard decision decoding technique is performed at the convolutional decoder. Output of the convolutional decoder is further decoded at the Reed-Solomon decoder applying the erasure decoding for $A = 0.5 \text{ mm}^2$	111
5.34	Outputs of the PLC and the VLC channels are decoded individually at the convolutional decoders. Outputs the convolutional decoders are combined and the joint hard decision decoding is performed at the Reed-Solomon decoder for $A = 0.5 \text{ mm}^2$	112
5.35	Outputs of the PLC and the VLC channels are decoded individually at the convolutional decoders. Outputs the convolutional decoders are combined and the joint hard decision decoding is performed at the Reed-Solomon decoder applying the erasure decoding for $A = 0.5 \text{ mm}^2$	112
5.36	The joint hard decision decoding technique is performed at the convolutional decoder with the Reed-Solomon decoder removed for $A = 0.1 \text{ mm}^2$	113
5.37	The joint hard decision decoding technique is performed at the convolutional decoder. Output of the convolutional decoder is further decoded at the Reed-Solomon decoder for $A = 0.1 \text{ mm}^2$	113
5.38	The joint hard decision decoding technique is performed at the convolutional decoder. Output of the convolutional decoder is further decoded at the Reed-Solomon decoder applying the erasure decoding for $A = 0.1 \text{ mm}^2$	114
5.39	Outputs of the PLC and the VLC channels are decoded individually at the convolutional decoders. Outputs the convolutional decoders are combined and the joint hard decision decoding is performed at the Reed-Solomon decoder for $A = 0.1 \text{ mm}^2$	114
5.40	Outputs of the PLC and the VLC channels are decoded individually at the convolutional decoders. Outputs the convolutional decoders are combined and the joint hard decision decoding is performed at the Reed-Solomon decoder applying the erasure decoding for $A = 0.1 \text{ mm}^2$	115
5.41	Decoded BER at the output of the convolutional decoder	118
5.42	Decoded BER at the output the Reed-Solomon decoder	119

List of Tables

3.1	Narrowband PLC bands regulated by Europe EN 50065 - 1 [19]	25
3.2	Main parameters of PLC G3 [20]	26
3.3	Mapping procedure for BPSK scheme using two cosine signals [10]	40
4.1	Hamming metric based on what was received and the valid codewords at that state [6]	59
4.2	Computation of soft decision metric [6]	69
4.3	Normalized soft decision metric [21]	69
4.4	BM's iterative procedure for finding $\sigma(X)$ [22]	75
5.1	Error-only decoding complexity of Berlekamp-Massey algorithm [23]	121
5.2	Error and erasure decoding complexity of Berlekamp-Massey algorithm [23]	121

List of Principal Symbols and Abbreviations

T_k	Absolute temperature
ϕ	Angle of radiated signal power
A_{coil}	Area of the lens
τ	Average duration of each impulse
η	Average number of impulses per second
I_B	Background photocurrent
E_b	Bit energy
P_e	Bit error probability
K	Boltzmann constant
f_c	Carrier frequency
C	Channel capacity
h	Channel response
r	Code rate
\otimes	Convolution
H_{LOS}	DC gain
v_t	Decision threshold voltage
d	Distance between the source and the receiver
q	Electric charge
g_m	FET transconductance
Ψ_c	Field of view
Γ	Gaussian to impulsive noise power ratio

N	IFFT size
A	Impulsive index
μ	Impulsive noise mean
Ψ	Incident angle
m_1	Lambertian emission order
R_0	Lambertian radiant intensity
B	Noise bandwidth
σ^2	Noise power
N_0	Noise power spectral density
g	Non-imaging concentrator gain
T_0	Observation period
G_{ol}	Open-loop voltage gain
P_t	Optical transmitted power
A_r	PD area
A_{eff}	PD effective area
R	PD responsivity
I_p	Photocurrent
m	Random noise state
P_r	Received optical power
n	Refractive index
$\Phi_{1/2}$	Semi-angle at half-power
c	Speed of light
SNR	Signal to noise ratio
T_s	Transmission gain
ACO	Asymmetrical clipped optical
AMI	Advanced meter infrastructure
AMR	Automatic meter reading
AWGN	Additive white Gaussian noise
BB	Broadband
BEC	Binary erasure channel
BER	Bit error rate

BPSK	Binary phase shift keying
CAS	Computation, addition and selection
CD	Convolutional decoder
CDMA	Code division multiple access
CENELEC	European Committee for Electrotechnical Standardization
CRC	Cyclic redundancy check
CSMA/CA	Carrier-sense multiple access with collision avoidance
DCO	Direct current optical
ECC	Error correction coding
ED	Erasure decoding
EMI	Electromagnetic interference
ERDF	French electric utility company
FCH	Frame control header
FEC	Forward error correction
FER	Frame error rate
FET	Field effect transistor
FOV	Field of view
FPGA	Field-programmable gate array
FSO	Free-space optical
GF	Galois field
HN	Home network
IFFT	Inverse fast Fourier transform
ISI	Inter-symbol interference
JD	Joint decoding
JHDD	Joint hard decision decoding
JSDD	Joint soft decision decoding
LED	Light emitting diodes
LFSR	Linear feedback shift register
LiFi	Light fidelity
LOS	Line of sight
MIMO	Multiple input multiple output

ML	Maximum likelihood
MRC	Maximal ratio combining
NB	Narrowband
OC	Optimum combining
OFDM	Orthogonal frequency division multiplexing
OOK	On-off keying
OWC	Optical wireless communications
PD	Photodetector
PDF	Probability density function
PLC	Power line communication
PSD	Power spectral density
QoS	Quality of service
QPSK	Quadrature phase shift keying
RC	Repetition coder
RSD	Reed-Solomon decoder
RF	Radio frequency
RS	Reed-Solomon
SCCC	Serial concatenation convolutional codes
SMC	Saturated metric combining
SNR	Signal to noise ratio
SOCPBFSK	Spread orthogonal continuous phase binary frequency shift keying
TCM	Trellis coded modulation
VLC	Visible light communication
Wi-Fi	Wireless fidelity

Chapter 1

INTRODUCTION

1.1 Power Line and Visible Light Communications

The prevalence of new devices for connected multimedia has posed a huge need on indoor communication networks to meet the ever increasing user demand. The use of multiple physical layers in local area networks will become a necessity in future due to requirements for coverage and throughput [3]. Bearing in mind that many media-based devices have already been connected to power distribution networks, it should be said that the combination of PLC and VLC technologies looks very attractive [2].

1.1.1 Power Line Communications

PLC technology uses existing power lines and household wirings to transmit and receive information. It is used for low or high data rate transmission. At different frequencies, it can be used in different application such as computer networks, high tension switchgears, smart metering infrastructure and light control systems. PLC technology can be classified into two categories based on the bandwidth usage, namely narrow-band PLC (NB-PLC) and broadband PLC (BB-PLC) [24]. NB-PLC operates in the band between 3 - 500 kHz and is normally used for smart grid applications such as meter reading and load-control system operating at low data rates. BB-PLC operates in the

band of 2 - 30 MHz and is used for both smart grid applications (including advanced meter infrastructure (AMI) and home networks and internet access [25]). However, new Homeplug devices such as HPAV2 are capable of operating in the band of 2 - 86 MHz using orthogonal frequency division multiplexing (OFDM) with multiple-input multiple-output (MIMO) transmission over multiple wires and are capable of achieving data rates in excess of 500 Mbits/s [26]. However, there are transmission problems that are facing PLC such as signal attenuation, interference (narrowband interference and inter-symbol interference (ISI)), noise disturbances (background and impulsive noise) and electromagnetic waves. In addition to these, PLC is associated with high energy consumption, high heat generation and interference with radio frequency to produce unwanted harmonics [27]. Most of the problems facing PLC can be overcome by using VLC.

1.1.2 Visible Light Communications

VLC is a fusion technology of solid-state lighting and wireless communication. It is regulated by IEEE 802.15.7 which is a standard for short range wireless optical communication using visible spectrum [28]. VLC uses visible light to transmit data through intensity modulation of light emitting diodes (LEDs) as they offer advantages in lighting. VLC is a green technology that is capable of achieving both lighting and communication and is used in many applications such as in hospitals (MRI scans and operating rooms) since it is unaffected by electromagnetic interference (EMI), in aircrafts for the same reason to increase data rates, improve reliability and reduce complexity, for smart house lighting and for intelligent transport system to facilitate inter-vehicle communication [29]. In VLC transmission, LED lighting is used as transmitter making it very important for modulation schemes considered in VLC systems to possess both non-flickering and dimming control. In VLC transmission, multiple reflections resulting from multipath propagation causes time spreading in the received signal [30]. However, the effect of multipath dispersion occurring along the VLC channel can be evaluated using power delay profile (PDP). VLC has many transmission advantages over PLC such as high data

security, low energy consumption, low heat generation, eco-friendly and larger bandwidth (about 10,000 times larger than RF bandwidth) [31]. But VLC is a new technology with under-developed physical layer and is mainly used for line of sight (LOS) transmission since visible light cannot penetrate walls. Therefore, VLC can access PLC for power supply and connections and this makes integration of PLC and VLC a possibility [32].

1.1.3 Integration of Power Line and Visible Light Communications

The exploitation of PLC and VLC has been widely investigated. The key advantage of a PLC system is that no additional wiring is required other than existing power cables. Thus, other networks can safely rely on PLC for connection. Combination of PLC and VLC has been exploited in many applications such as smart lighting, in signboards (airports, hotels, museums, etc.) and indoor positioning systems [33–35]. In these applications, the PLC system serves as a backbone for the VLC system. Thus, the VLC system receives information from the power line that provides its power through a PLC modem [35]. The VLC system is mainly used as the downlink to improve system performance. Recently, hospitals have started adopting E-HEALTH to provide higher diagnostic efficiency and a better patient experience [36]. In this application, VLC is used as a replacement for Wi-Fi or 3G/4G due to its high bandwidth capacity, radiation-free and so on. Another application where this combination was utilized is in smart lighting where VLC not only provides lighting but also provides communication [33]. Furthermore, integration of PLC and VLC is also used in street lighting, traffic lighting, point to point applications, inter building communication, and vehicle safety lighting [34]. To realize a PLC-VLC system, the VLC system must access the PLC system that serves as a backbone network. In this research, PLC G3 physical layer specification for an OFDM system in the CENELEC band is adopted for both the PLC and the VLC systems. The frequency range for PLC G3 is between 35.9 kHz - 90.6 kHz of the CENELEC - A band [4]. PLC G3 physical layer specification is the last of the physical layer specifications that were recently developed for low data rate transmission in the low frequency band. It was published in 2009 and was developed by Maxim Integrated Products and the French

Electric utility company (ERDF) [37]. OFDM-based PLC G3 specification provides advantages such as robust communication in extremely harsh PLC channels, a minimum of 20 kbps effective data rate in the normal mode operation, ability to notch selected frequencies allowing for co-habitation with S-FSK narrowband communication and robust communication through selection of frequencies on the channel with minor interference using dynamic tone adoption capability. Therefore, the improvements provided by PLC G3 physical layer specification will be very useful in realizing the objective of this research investigation [9]. Combination of PLC and Wi-Fi has been extensively investigated [2, 3, 38–42]. More so, there have been many investigations into serial combination of PLC and VLC for hybrid systems [29, 33–36, 43–46]. However, there have been no investigation into the parallel combination of PLC and VLC systems.

1.2 Joint Decoding Technique

The concept of joint decoding has been used in various applications to improve the overall system performance. In [47], it was adopted in compressive multi-view video streaming to improve image quality by reducing the blurring effect that occurs in the reconstructed frames at the receiver. In the presence of limited data training, joint decoding was combined with channel estimation in [48] for linear multiple-input-multiple-output (MIMO) channels to obtain performance that is close to that of a receiver with complete knowledge. Furthermore, joint decoding was applied to a CDMA system in [49] to increase the spectral efficiency of CDMA by supporting multiple active users without overcrowding the receiver. In [50, 51], joint maximum likelihood (ML) was used in overloaded MIMO-OFDM to improve the performance of the receiver. In these applications, joint decoding technique is either applied at the channel output by combining the outputs of both channels or at the receiver before the decoder. At the receiver, the signals can be combined using combiners such as maximal ratio combining (MRC), optimum combining (OC) or saturated metric combining (SMC) [2].

1.3 Problem Statement

Many applications utilize the combination of PLC and Wi-Fi [52, 53] with the purpose of gaining more communication advantages. However, inefficiencies such as low data security, limited bandwidth and high channel interference experienced in Wi-Fi transmission hugely affect the overall system performance [52]. Limited bandwidth in Wi-Fi causes “spectrum crunch” resulting in network throughput degradation as more Wi-Fi users are connected to the network and increased number of users at the same Wi-Fi access point increases the network delay due to the CSMA/CA mechanism described in 802.11 standards [54].

Besides integration of PLC and Wi-Fi, there are other applications that have utilized serial combination of PLC and VLC systems as demonstrated in [33–36]. In these applications, VLC is used in the downlink to improve system performance. However, there are issues facing applications of this nature such as double attenuation of the received signal and dependence of one system on the other [34]. Thus, if one system breaks down, the entire system fails to function.

The problems that are encountered in the combination of PLC and Wi-Fi can be mitigated if not eradicated by replacing Wi-Fi with a VLC system. This is due to many advantages that are offered by the VLC network such as: higher bandwidth that is almost 10,000 times larger than entire radio frequency (RF) spectrum and no interference since visible light do not electromagnetically interfere with other devices [53]. VLC has other advantages over Wi-Fi such as secured data transmission in the physical layer since light waves cannot penetrate walls or solid structures and non-existence of co or adjacent channel interference unlike radio waves that experience co-channel interference which contributes to source of noise [55]. Furthermore, the issues that affect serial concatenation of PLC and VLC systems can be resolved by adopting parallel combination which can allow transmission through one system if the other is not active and the received signal is only attenuated once in each channel [35]. More so, the combination of PLC and VLC systems in parallel offers high data rate and high transmission security [33].

1.4 Research Objective

VLC uses LEDs to transmit data as shown in Fig.1.1 and offers more secured transmission since visible light cannot penetrate walls. Therefore, it is mostly used for line of sight (LOS) transmissions but it suffers from attenuation due to distance between the source and the receiver [28].

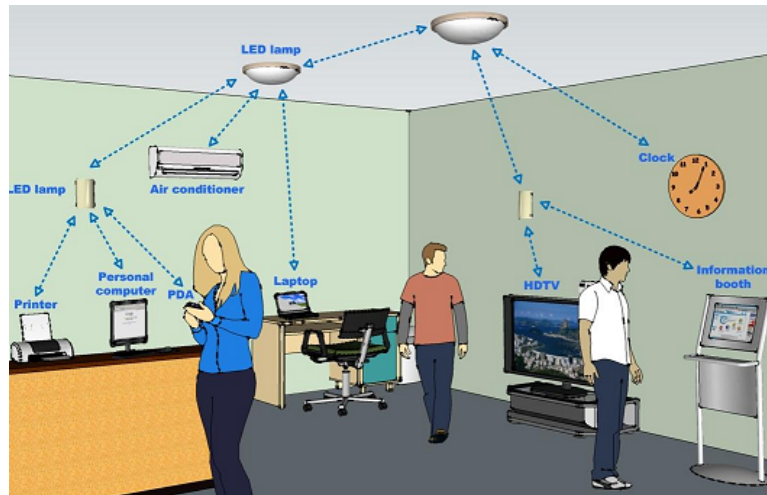


FIGURE 1.1: Indoor visible light communication courtesy of [1]

Thus, to receive a good signal quality, the receiver has to be aligned properly with respect to the source and deviation from such position results in degradation of the signal quality. This limits the freedom of movement of the receiver. But both the source (LED lamp in this case) and receiver (computer) are connected to power line cables. These power line cables are not affected by attenuation for a small distance [27]. This advantage can be exploited to improve the quality of signal received at different positions by combining both networks in parallel. Thus, providing the receiver the freedom to rely on either VLC, PLC or combined system depending on the system that provides better signal quality at a particular position.

This research is aimed at enhancing the overall system performance of a parallel PLC-VLC system in terms of BER and computational complexity. This overall objective is

achieved by first modifying the VLC OFDM to allow only transmission of positive unipolar signals. Second, apply the joint decoding technique at the inner or outer decoder and third, apply the erasure decoding technique at the inner or outer decoder.

1.4.1 Research Question

Based on the problems that are associated with serial combination of PLC and VLC systems and parallel combination of PLC and Wi-Fi systems as described in Section 1.3, therefore this research proposes joint decoding of parallel PLC and VLC systems. Thus, the question that this research attempts to answer is as follows:

For a parallel PLC-VLC communication system that has an identical physical layer specification, what are the effects of applying a joint decoding technique at the inner or outer decoder in terms of BER and computational complexity?

1.4.2 Research Aims

The specific objectives that have to be accomplished in order to answer the research question and as a result achieve the overall research objective are as follows:

- Modeling PLC and VLC physical layers according to PLC G3 specification
- Modifying the VLC OFDM by adopting DCO-OFDM in the VLC system to combat nonnegative signal effects
- Modeling PLC channel as an AWGN channel with impulsive noise distribution represented by Middleton Class-A noise model
- Modeling VLC channel as a line-of-sight (LOS) link affected by attenuation
- Combining both PLC and VLC in parallel and establishing simultaneous transmission through both channels

- Applying joint decoding technique at the inner or outer decoder
- Applying erasure decoding technique at the inner or outer decoder

1.5 Research Contributions

This research makes valuable contributions to the body of knowledge in the field of digital communications, with a focus on joint decoding of parallel PLC-VLC system. There have been a number of works done on the application of joint decoding techniques, combination of PLC and Wi-Fi networks and integration of PLC and VLC networks. However, there has been no work done in the parallel combination of PLC and VLC networks.

The main contributions of this research are summarized below:

- Combine PLC and VLC systems in parallel and establish simultaneous transmission the systems.
- Apply joint decoding technique at the inner or the outer decoder in order to improve system performance. This technique is based on reducing the BER at the receiver.
- Performance analysis of joint decoding technique in improving the overall system performance in terms of signal quality and spectral efficiency is presented in this dissertation.
- Analysis of performance of serial and parallel combination of PLC and Wi-Fi networks in improving system throughput, decoding complexity and implementation complexity are also presented in this dissertation.
- In this dissertation, the performance analysis of combination of PLC and VLC networks in reducing complexity and improving signal coverage is also presented.

- The PLC G3 model for modeling both PLC and VLC physical layers is introduced in this dissertation. This model is based on providing advanced error-correction techniques for combating both random and burst errors.
- PLC channel modeled with impulsive noise and VLC channel modeled with attenuation are studied in this dissertation.
- Examined the performance of bit-interleaved convolutional and Reed-Solomon coded OFDM in PLC in the presence of impulsive noise and DCO-OFDM in VLC in the presence of attenuation.
- Performance analysis of Viterbi and Berlekamp-Massey algorithms are presented in this dissertation. These algorithms aim at maximizing the data rate given specific transmit power and BER constraints. At the same time, the algorithms maintain minimum computational complexity.

1.6 Layout of the Dissertation

This dissertation consists of six chapters. The first chapter provides introduction to the dissertation whereas second chapter presents literature review of works done on joint decoding technique, integration of PLC and Wi-Fi networks and combination of PLC and VLC networks. The rest of this dissertation can be divided into two parts. The first part, including Chapters 3 and 4, focuses on the system model and joint decoding technique respectively. The second part consisting of Chapter 5 focuses on the simulation results of joint decoding technique. The dissertation is organized as follows:

Chapter 2: Literature Review

In this chapter, some of the works that have already been done in the aspect of joint decoding technique and LiFi technology are reviewed. The chapter starts by reviewing some of the applications that have utilized joint decoding technique and the advantage

that was gained by adopting this technique. The chapter continues with the review of both serial and parallel integration of PLC and Wi-Fi networks. The chapter concludes with a review of serial combination of PLC and VLC networks.

Chapter 3: System Model

The system model that is used in this research investigation is presented in this chapter. Next, PLC G3 model is introduced and how our system is adopted from PLC G3 and how the OFDM system is modified to meet VLC transmission requirements is explained. Finally, different components of the system model are described.

Chapter 4: Joint Decoding Scheme

The concept of joint decoding technique is described in details in this chapter. The chapter describes the decoding algorithms that will be used in implementing the joint decoding technique. And finally, finishes by describing where joint decoding is applied in our system and shows a flowchart diagram indicating various scenarios that are considered in the application of the joint decoding technique.

Chapter 5: Simulation Results

In this chapter, the simulation results and detailed analysis of the results are presented. The simulation results show that joint decoded system performs better than PLC and VLC systems at certain distance of separation between the source when joint decoding is applied at the inner decoder.

Chapter 6: Conclusions and Future Work

This chapter summarizes the main conclusions of this dissertation and presents possible future exploitations.

It is worth mentioning that to the best of our knowledge, there has been no investigation into joint decoding of parallel PLC and VLC transmission systems. Thus, this research presents the first study of such a possibility.

1.7 Summary

This chapter consists of six sections. Section 1.1 provided background knowledge on PLC and VLC systems. The importance of these networks in digital communication and the problems that are associated with their utilization were also discussed in this section. It was shown in this section how the emergence of VLC technology has provided a welcome alternative to radio frequency (RF) spectrum owing to its much greater bandwidth. The section concluded by providing background knowledge on the applications that have integrated PLC and VLC networks in order to improve system performance. In Section 1.2, the concept of joint decoding technique was introduced and some applications that have utilized this technique were discussed. The problems that are associated with the serial and parallel combination of PLC and Wi-Fi systems and serial combination of PLC and VLC systems were presented in Section 1.3. This section concluded by describing how replacing Wi-Fi system in this applications with VLC system would improve the system performance. Section 1.4 presented the main objective that this research tends to accomplish. It was shown that to achieve this overall objective, a specific research question has to be answered and several tasks have to be completed as described in the research aims. In Section 1.5, the research contributions were presented. The aim of these contributions is to add valuable knowledge in the field of digital communications. This chapter concluded by presenting the layout of the dissertation in Section 1.6. This section provided a brief explanation of what each chapter has to offer.

Chapter 2

LITERATURE REVIEW

2.1 Introduction

PLC uses the existing electrical power line networks for telecommunication purposes. Over the years, power line networks have served as a medium of transmission and distribution of electric signals [24]. However, the existence of wireless networks and most recently, the emergence of VLC technology have reduced dependency on power line networks [56]. In many applications, the power line networks are combined with either wireless or visible light networks due to ability of these networks to access power line networks as their backbone for connection and power supply [32].

The survey of literature surrounding joint decoding, combination of PLC and wireless networks and integration of PLC and VLC systems are presented in this chapter. This chapter ultimately serves as a knowledge basis that will be used in later chapters of the dissertation to develop a suitable system model that will be used in this research investigation and positions at which joint decoding will be applied in order to obtain better BER performance for the joint decoded system.

2.2 Application of Joint Decoding

In [57], FPGA implementation of LPDC decoders based on joint row-column decoding algorithm was proposed. This algorithm was used to process m rows from the uppermost row to the lowest row during each iteration to ensure that no distinct-column processing was required. Through simulation, joint decoder and traditional decoder was compared. It was discovered that with joint decoder, BER decreases and converges faster to a certain value. This increases the system throughput, thus, improving the performance both in the waterfall and error floor regions. In [58], the authors proposed iterative joint channel decoding of correlated sources employing serial concatenation convolutional codes (SCCC). To decode two packets of data that are correlated, the receiver uses iterative soft decision decoding (SDD) technique to perform joint detection of the transmitted data sequence. Their simulation results show that jointly decoding the two received packets improves the BER and frame error rate (FER) depending on the degree of the correlation between the data packets. The authors in [47] proposed joint decoding of independent encoded compressive multi-view video streams. Different views are encoded and transmitted independently and are then jointly decoded at the receiver. They showed through simulation results that joint decoding reduces the blurring effect that occurs in the reconstructed frames at the receiver, thereby, improving the video quality. Graphical interpretation of the simulation result is shown in [47], Fig.4]. In [48], the authors proposed joint decoding and channel estimation for linear multiple-input-multiple-output (MIMO) channels assuming that the receiver has no a priori knowledge of the channel parameters. At the receiver, they used the Viterbi algorithm to find the maximum likelihood (ML) sequence given the current channel estimate. Their performance analysis show that through joint detection and estimation, the receiver can approach the performance of a receiver with complete knowledge when very limited training data is used. In [49], joint decoding was applied to a CDMA system. The joint decoding technique was achieved through analysis of signaling method for random CDMA channels that combine iterative decoding of error control coding (ECC) with an iterative demodulation processing. The authors realized

through simulations and result analysis that joint decoding increases the spectral efficiency of CDMA by supporting multiple active users without overcrowding the receiver. They also realized that joint decoding can mitigate or in some cases, completely eradicate the detrimental effects of unequal received powers. Maximum likelihood (ML) joint decoding scheme of block coded signals in the overloaded MIMO-OFDM system was proposed in [50, 51]. The performance of this technique was evaluated through experiments in [50]. In their work, they encoded information bit streams using separate encoders and then transmitted them using different antennas. At the receiver, one antenna was used to receive the information coming from multiple transmitting antennas. Joint ML decoding was done through the calculation of joint metrics for every combination of the codewords over the entire signal streams. Their result analysis show performance improvement through joint ML decoding of coded signal streams. However, in [51], multiple antennas were used for transmission and joint detection and decoding was applied at the receiver. Their simulation result show improvement in the BER performance because signal streams are jointly demodulated through ML decoding. All these investigations discussed utilized joint decoding technique and their result analyses show improvement in the overall performance of the system.

2.3 Combination of PLC and Wireless Systems

LiFi technology is a light-based communication that uses light waves instead of radio waves to transmit data and this technology has been widely investigated. In [56, 59], Wi-Fi was used as the uplink system and VLC as the downlink system to increase the overall network capacity. In [56], the authors proposed and implemented a practical hybrid system consisting of Wi-Fi and VLC links that enables data packets requested by the user applications to be transmitted through Wi-Fi and requested data from the server is received through the VLC interface. The authors of [59] proposed an indoor hybrid Wi-Fi and VLC internet access system. Their system model integrates a Wi-Fi access point that conforms to the IEEE 802.11 standards and VLC system as the downlink.

Parallel combination of PLC and wireless transmission adopting a joint decoding technique at the receiver has also been investigated. In [38], the authors studied the performance of error correction probability in binary linear code ensembles when each codeword is divided into subcodewords with each subcodeword transmitted through one of the parallel channels. They investigated the reliable channel region that allows for reliable communication over parallel channels and decoded received subcodewords using one ML decoder. In [39], joint decoding technique was also used to decode subcodewords transmitted over multiple parallel channels. The authors focused on finding new upper bounds on the ML decoding error probability deployed in parallel-channel setting. They obtained inner bounds on the boundary of the channel regions that ensure reliable communication under ML decoding and observed remarkable improvement compared to results reported in [38]. The authors in [40, 41] used joint decoding technique to decode information received from parallel free-space optical (FSO) and radio frequency (RF) channels. In [40], only one channel is operational at a time while the other channel is idle. In [41], joint decoding was also utilized in decoding of rateless coding for a hybrid FSO and RF communication system. By using this technique, they observed that FSO and RF channel resources can be fully utilized without having to reconfigure or redesign the transmitter. Results of both investigations show improvement in the throughput of the system. In [42], the authors implemented joint decoding of two independent binary erasure channels (BECs) using a bit mapper to determine the allocation of coded bits to the channels. Through optimization results, they showed improvement in the decoding threshold or, alternatively, reduction in the spatial chain length.

Having presented works done utilizing joint decoding techniques, serial combination of VLC and Wi-Fi and serial integration of PLC and VLC, there are two notable investigations that exploited parallel transmission using PLC and wireless systems using joint decoding technique at the receiver. The First work was done in 2012 [2], the authors proposed simultaneous transmission over PLC and wireless channels in order to improve

the performance of indoor home networks (HNs). They implemented modulation diversity through the combination of different diversity schemes such as optimum combining (OC), saturated metric combining (SMC), and maximal ratio combining (MRC) that are suitable for wireless/PLC transmission [52]. They studied the performance of different combiners by measuring source of impairment (attenuation) and source of disturbance (noise) in parallel PLC and wireless links and combined them with diversity analysis as shown in Fig. 2.1. In modeling their system, they assumed that an identical OFDM modulated signal was transmitted over the two channels. At the receiver, the OFDM subcarriers were demodulated using separate hardware before combining the received signals [53].

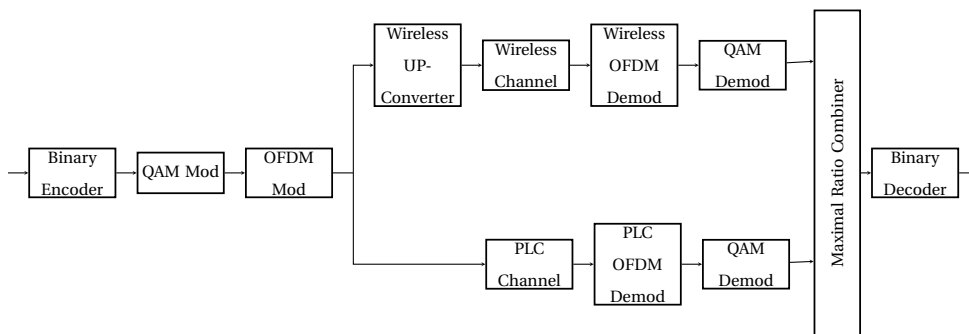


FIGURE 2.1: Wireless-PLC communication using modulation diversity [2]

Multipath propagation that occurs in wireless and PLC channels in an indoor network causing their impulse responses to contain finite delay spread was controlled using an appropriate guard length interval [26]. For this investigation, they assumed guard length interval to be longer than the channel impulse response durations in order to neglect the effect of inter-symbol interference (ISI). They further assumed the bandwidth of the OFDM subcarrier to be small and modeled both channels as frequency flat channels [52]. Their analysis show that wireless channel contains conventional Gaussian noise while PLC channel contains harmful impulsive noise that affects the performance of MRC. Their experimental results show that these two channels can be combined to increase data rate through multiplexing or improve system reliability through diversity combining [2].

The most recent work done in 2014 was based on the comparison of modulation and coding diversity schemes making use of wireless and PLC links. They evaluated the performance of wireless and PLC media diversity in the office environment [3] as shown in Fig. 2.2. Non-identical modulated signal was transmitted over wireless and PLC channels using wireless OFDM and PLC OFDM modulators respectively [38]. At the receiver, the signals from wireless and PLC channels were demodulated separately using wireless and PLC OFDM demodulator respectively. Prior to transmission, the output of the encoder is demultiplexed and mapped into signal points. The outputs of the demodulators are transformed into bit-wise metrics, multiplexed and then fed into a binary decoder [3].

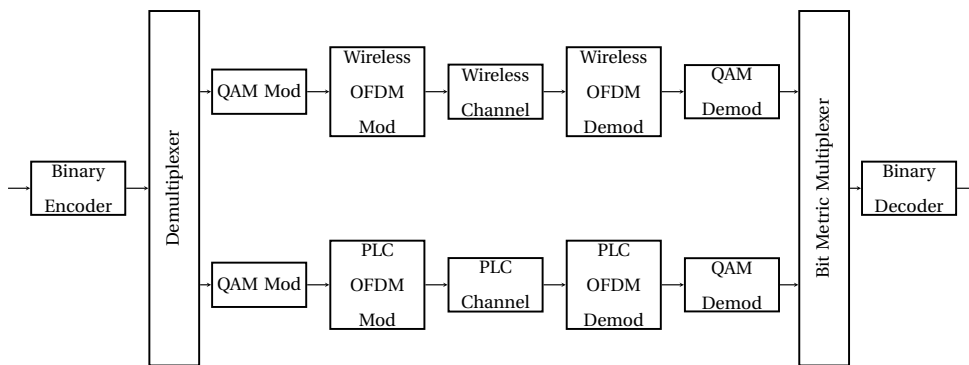


FIGURE 2.2: Wireless-PLC communication using coding diversity [3]

They used empirical SNR values in Monte Carlo simulation to evaluate the throughput advantages of both diversity schemes. From their simulation results, it was concluded that coding diversity outperforms modulation diversity in terms of amount of data that can be achieved [3]. Coding diversity is bit-interleaved coded modulation (BICM) based and is currently used in wireless or PLC systems since different signal constellation can be used for wireless and PLC channels which is not the case in modulation diversity as it uses only one OFDM modulator minimizing its implementation complexity [39]. In both investigations, a narrowband model was used to analyze the performance of several diversity-combining schemes and they presented results from BER analysis to validate their claim [40]. In their investigations, they both focused on broadband PLC transmissions in the 2 - 30 MHz and wireless transmissions in the 2.4 GHz band. Furthermore, they both assumed Middleton Class - A noise for BB-PLC channel and AWGN

for the wireless channel. However, it is worth noting that in modulation diversity, identical modulated signal is transmitted over the two channels while in coding diversity, same coded signal is transmitted over the two channels [2, 3]. The results obtained through measurement data show in both investigations that combining methods and joint decoding can be used to increase the effective SNR and improve system throughput [2].

2.4 Combination of PLC and VLC Systems

PLC and VLC systems can also be combined to improve the performance of indoor applications [33–36]. In [33, 35], PLC and VLC were combined for indoor hospital applications. They proposed E-HEALTH as an efficient complement to traditional healthcare services with the aim of enhancing the efficiency of diagnosis and improving the patient experience [33]. In [34], the authors proposed an indoor broadband broadcasting system based on PLC and VLC with the view of reducing the complexity of VLC network protocols and obtaining a system that requires less modification to the existing infrastructure while at the same time, providing better signal coverage. The proposed system model was adopted for smart house lighting enabling lighting and data communication simultaneously. This application can be used in hospitals, shopping malls, stadiums, music halls, etc. In [36], integration of indoor visible light and power line communication systems was proposed. They combined PLC and VLC systems for indoor applications using the PLC system as backbone for the VLC system. VLC system was utilized in the downlink to improve network efficiency and provide a more economical way of fulfilling the need for broadband access for indoor users [34]. The results obtained from these investigations show improvement in the throughput of the system. More investigations in serial PLC and VLC combination were made in [28, 43–46, 60]. These works combined PLC and VLC systems to develop hybrid systems with improved system performance. Low-complexity SOCPBFSK-OOK interface between PLC and VLC channels for low data rate transmission applications was proposed in [28]. They studied the performance of using a spread orthogonal continuous phase binary frequency

shift keying (SOCPBFSK) receiver combined with an on-off keying (OOK) modulator for low data transmission between PLC and VLC channels. They evaluated the error rate performance of the system using eye diagrams. The authors of [43] proposed a cost-effective approach for ubiquitous broadband access based on a hybrid PLC-VLC system with low-cost modification to the current infrastructure. They were able to achieve broadband access network that supports full duplex transmission through each LED using the decode-and-forward (DF) technique. Their results show that duplex symmetric PLC-VLC system has superior performance compared to conventional PLC-VLC integrated system. In [44] cascaded PLC-VLC channel using OFDM and CSK techniques for full link transmission was investigated. From the BER graphs they obtained through simulations, they concluded that communication between the two channels is possible. In [45], integration system of white LED VLC and PLC was proposed. They implemented a wiring system for optical communication using existing power lines. They achieved high quality of service (QoS) and high quality of communication in all areas of the room. The authors of [46] investigated the integration of PLC and VLC for an indoor communication. They adopted the same orthogonal multicarrier modulation format in channels and analyzed the capacity of the hybrid PLC-VLC system. Through simulation results, they observed that the system achieves highest capacity when the user is at the center and decreases as the user moves closer to the walls.

2.5 Summary

This chapter is composed of four sections. Introduction to what the chapter has to offer was provided in Section 2.1. The review of works that have been previously done in joint decoding application was presented in Section 2.2. It was observed that joint decoding can be used to improve the overall system performance in terms of system throughput, BER and FER, video quality in multi-view video streams and spectral efficiency. In Section 2.3, literature review of integration of PLC and wireless networks as well as VLC and Wi-Fi networks was provided. From their simulation results, it was observed that by combining VLC and Wi-Fi systems and deploying the VLC system as

the downlink system, the overall capacity of the system can be increased due to greater bandwidth available in the visible light spectrum compared to Wi-Fi networks. In parallel PLC and Wi-Fi system, the joint decoding technique was applied at the receiver's end and simulation results from this approach show significant improvement in the system throughput, decoding threshold and implementation complexity. Finally, Section 2.4 reviewed the serial concatenation of PLC and VLC systems. It was gathered from this section that by combining PLC and VLC systems in serial, the system performance can be improved in terms of reducing complexity, improving throughput and signal coverage in areas such as hospitals, shopping malls, etc.

Chapter 3

SYSTEM MODEL

3.1 Introduction

The demand to use PLC technology to deliver high-speed communication signals over electric power lines continues to grow at a rapid pace. However, power line networks were not originally designed for data transmission but to transport electric signals at lower frequencies since they provide a harsh environment for higher frequency communication signals [61]. Therefore, interest has been shown in the use of hybrid technology in indoor applications to obtain improved high-speed communication. One of the approaches taken in this regard is combination of power line and Wi-Fi technologies. However, issues such as low data security, limited bandwidth and high channel interference experienced in Wi-Fi transmission hugely affect the overall system performance [52]. Limited bandwidth in Wi-Fi causes “spectrum crunch” resulting in network throughput degradation [54]. Another approach is serial combination of PLC and VLC technologies. But there are issues facing applications of this nature such as double attenuation of the received signal and dependence of one system on the other. Thus, if one system breaks down, the entire system fails to function [34]. In this chapter, the proposed system model that is used to carry out this research investigation is first presented and it is then shown how this proposed system was adopted using PLC G3 physical layer specification outlined in [4, 9, 62]. To describe the operational mechanism of

PLC G3 system, the components that make up the physical layer were analyzed. Next, the OFDM systems used in both PLC and VLC channels are presented and it is shown how the OFDM system was modified in the VLC system [63, 64]. The chapter concludes with the analysis of PLC and VLC channel models modeling the PLC channel as AWGN channel with impulsive noise distribution [65, 66] and VLC channel as AWGN channel with line of sight propagation effect [13, 14].

3.2 Parallel PLC-VLC System

The transmission system model adopted in this research investigation is shown in Fig. 3.1. The system is implemented according to the PLC G3 physical layer specification [4]. To establish transmission between the sender and the receiver, the information is first encoded using a forward error correction (FEC) encoder. The encoded signal is then modulated using binary phase shift keying (BPSK) modulation scheme combined with OFDM technique [67]. The modulated signal is then transmitted over two non-identical channels where it is corrupted by noise. At the receiver, the information received from both channels is first combined and then decoded as one codeword [4].

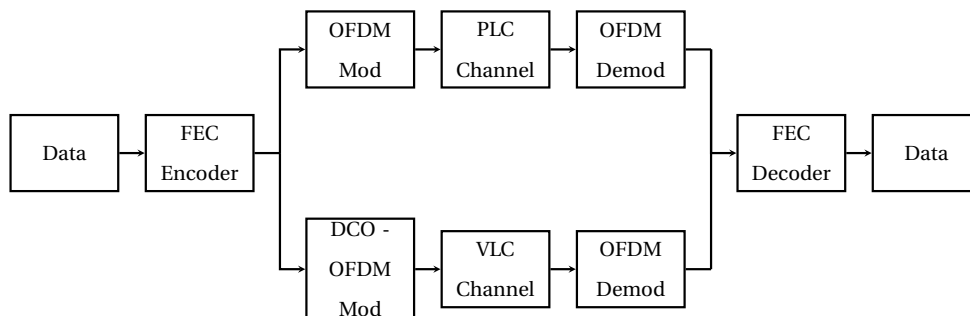


FIGURE 3.1: Parallel PLC-VLC system model with OFDM over PLC channel and DCO-OFDM over VLC channel

Parallel combination of these two distinct systems offers numerous advantages such as increased data rate, improved system reliability, higher spectral efficiency [49], continuous data transmission unless in the event that both systems fail and diversity [2]. However, there are pitfalls that are associated with transmission system of this sort. These

include: high maintenance cost, aging of the power lines, combating noise sources in the PLC channel, attenuation that affects VLC transmission, etc [68].

3.3 PLC G3 Model

The system depicted in Fig. 3.1 is modeled according to PLC G3 physical layer specification shown in Fig. 3.2. The PLC G3 bandwidth is between 35.9 kHz - 90.6 kHz of the CENELEC - A band. An OFDM with binary phase shift keying (BPSK) or quadrature phase shift keying (QPSK) modulation schemes per carrier is chosen such that in normal mode operation, the data rate is supported up to 33.4 kbps [9, 69]. The use of BPSK or QPSK modulation schemes for each carrier also simplifies the design of the receiver since no tracking circuitry is required for the coherent detection of the phase of each carrier. This is because, the phases of the carriers in the adjacent symbols are used as reference for detecting the phases of the carriers in the current symbol [67]. This standard can be adopted to extend the frequencies to 180 kHz. Thus, the sampling frequency can be selected to be 400 kHz to provide some margin above the Nyquist frequency for signal filtering in the transmitter (for spectrum shaping and signal images removal) and at the receiver (for frequency band selection and signal enhancement) [19]. The physical layer of both systems is designed according PLC G3 system model shown in Fig. 3.2. The system combines Reed-Solomon and convolutional coding with OFDM modulation scheme in order to merge the benefits of multicarrier modulation and FEC coding to obtain a system that has excellent performance capability in the presence of multipath and fading channels [4].

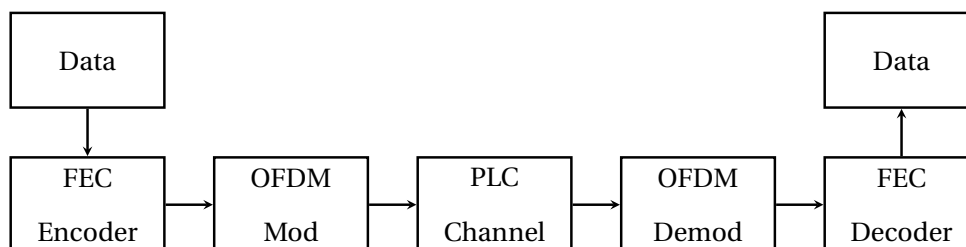


FIGURE 3.2: Transmission system model according to PLC G3 specification [4]

This system operates in two different modes, namely normal mode (BPSK mode or QPSK mode) and robust mode. In Normal mode, the forward error correction (FEC) encoder consists of a Reed-Solomon encoder and a convolutional encoder. The system also supports Reed-Solomon code with parity of 8 and 16 bytes [70]. In Robust mode, FEC is composed of Reed-Solomon and convolutional encoders followed by a Repetition Coder (RC) that introduces three redundancy bits for each data bit making the system more robust to channel impairments [71]. However, this reduces the system throughput by a factor of 4. Additionally, the system can also work in super robust mode to transmit frame control header (FCH). In this mode, the convolutional code combined with the RC introduces five redundant bits for each data bit [72]. The interleaver block that follows the convolutional encoder is used to provide protection against two different error sources, namely, the burst error capable of corrupting a few successive OFDM symbols and the frequency deep fade capable of corrupting a few adjacent frequencies for a large number of OFDM symbols [73]. To correct errors from both sources, a 2D interleaver is used where one interleaves in the time domain and the other interleaves in the frequency domain. This technique is very important as it prevents frequency-dependent fading and impulsive noise from corrupting the data [9]. The FEC encoder and decoder and OFDM modulator and demodulator consist of different components. The bandwidth available within the CENELEC band is divided into sub-channels, which can be seen as multiple independent PSK modulated carriers having different non-interfering (orthogonal) carrier frequencies [4]. The convolutional and Reed-Solomon encoders provide bit redundancy that enables the receiver to recover bits that are lost due to background and impulsive noise. The correlation of the received noise at the input of the decoder is reduced through time-frequency interleaving scheme, thereby providing diversity [19, 69].

PLC G3 is an open protocol that was developed by the G3-PLC Alliance organization for low frequency NB-PLC systems that operates in frequency band below 500 kHz [4]. This frequency has been further reduced to 148.5 kHz and sub-divided into four bands that are fully regulated by CENELEC. These sub-bands are described in EN 50065-1 as follows [20]:

- Band-A occupies the frequency range between 3 kHz and 95 kHz and is available for energy suppliers only for monitoring and controlling low voltage users. PLC G3 operates within this frequency range.
- Band-B covers the frequency range between 95 kHz and 125 kHz and is reserved for consumers with no access protocol.
- Band-C is reserved for home use and is regulated by CSMA/CA access protocol. It occupies the frequency range between 125 kHz and 140 kHz.
- Band-D has a frequency range of 140 kHz to 148.5 kHz and is utilized by alarm and security systems that have no access protocol.

TABLE 3.1: Narrowband PLC bands regulated by Europe EN 50065 - 1 [19]

CENELEC Band	Frequency Range (kHz)	Primary Use
A	3 – 95	Reserved for Energy providers
B	95 – 125	Reserved for all users
C	125 – 140	Reserved for home networking
D	140 – 148.5	Reserved for alarm and security systems

The summary of the sub-division of the narrowband frequency is provided in Table 3.1. Applications of NB-PLC are mostly in automatic meter infrastructure (AMI), automatic meter reading (AMR), controlling of street lights and providing vehicle-to-grid system communication [20]. The PLC G3 protocol uses modulation techniques to achieve higher data rates and NB-PLC is capable of achieving data rates up to 128 kbps through the use of OFDM modulation scheme. To increase the robustness of the OFDM system to channel impairments, channel encoding, interleaving and repetition code are performed prior to transmission [9].

TABLE 3.2: Main parameters of PLC G3 [20]

Frequency range	35 – 91 kHz
Sampling frequency	400 kHz
Subcarrier spacing	1.56 kHz
No. of data subcarriers	36
No. of pilot subcarriers	–
FFT interval	640 μ s
Cyclic prefix	75 μ s
OFDM symbol duration	715 μ s
Preamble period	6080 μ s
FEC	RS, CC
Interleaving	per data packet
Windowing	YES

PLC G3 utilizes OFDM modulation scheme in the frequency region between 35 kHz and 91 kHz. Either BPSK or QPSK modulation technique can be used to modulate the subcarriers and a maximum data rate of 33.4 kbps is achievable using QPSK and FEC [70]. PLC G3 provides higher transmission reliability when compared to counterparts such as PLC PRIME but redundant bits added in the frame and OFDM subcarriers affect data transmission rate [19, 74].

3.4 FEC Encoder and Decoder

The FEC encoder is located at the sender's side of the transmission system. Prior to transmission, a scrambler is used to introduce random distribution in the data. At the beginning of each data frame, a data structure called FCH is transmitted [4]. This data structure contains information such as frame type, frame length and frame index of

the frame that is being transmitted. The message is then encoded using both Reed-Solomon and convolutional encoders aligned in series to provide combined error correction scheme that is capable of combating both burst and random errors [73]. Before passing the codeword through the channel, the codeword is interleaved to provide protection against frequency deep fading and impulsive noise that are present in the channel. At the receiver, the FEC decoder performs the opposite functions of the FEC encoder in order to recover the original message that was transmitted [71].

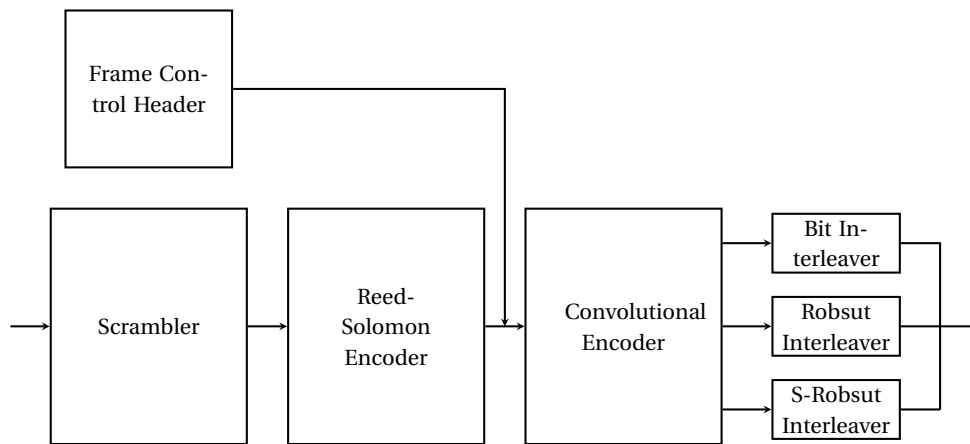


FIGURE 3.3: Components of an FEC encoder [4]

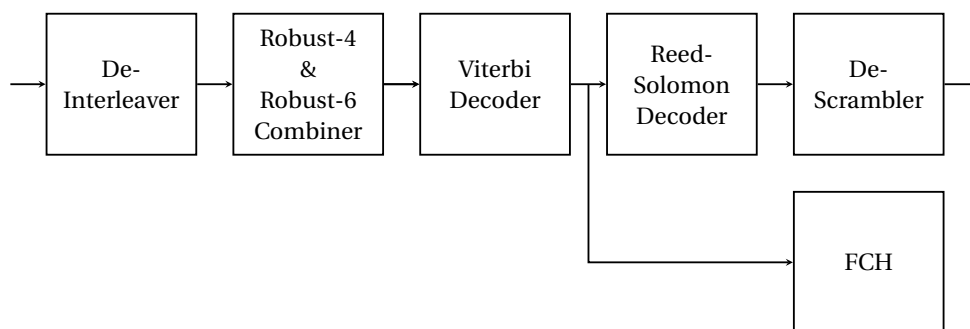


FIGURE 3.4: Components of an FEC decoder [4]

The two decoders aligned in cascade inside the FEC decoder are convolutional decoder that uses Viterbi algorithm and Reed-Solomon decoder that uses Berlekamp-Massey algorithm [70]. The importance and operation of these two algorithms are discussed in Chapter 4. The FEC scheme helps to reduce the adverse effects of multipath fading by introducing redundancies into the data to be transmitted. These redundancy bits are

added in a controlled way to enable the receiver to detect and correct transmission errors. This technique leads to improvement in the BER performance by providing high spectral efficiency at low bit error rate [19]. In normal mode, FEC consists of Reed-Solomon and convolutional encoders only whereas in robust mode, FEC encoder is followed by a repetition code (RC) that repeats each bit four times in order to make the system more robust to channel disturbances [9].

Forward error correction can be used to improve the quality of service (QoS) by reducing the BER. FEC enables the receiver to correct the errors that have occurred in the transmitted message without requiring any further information from the sender [75]. Thus, data lost during transmission can be recovered using this technique without a need for retransmission. For an RS (n, k) code, systematic FEC preserves the k message symbols and adds $(n - k)$ parity symbols for protection against channel disturbances [76]. Different types of errors occur in the transmitted data due to different types of noise. Thus, different error correction schemes for combating different types of noise have been proposed in [77–80]. Some of these proposed schemes used standard error correction scheme such as RS encoding and convolutional decoding while others added interleaving scheme in order to ease the burden on the RS decoder [81].

3.4.1 Frame Control Header

The frame control header (FCH) consists of four data symbols that are transmitted at the beginning of each data frame. The FCH contains information about the frame that is about to be transmitted, such as frame type, length and index [4]. It uses all the allowable subcarriers and is protected with five cyclic redundancy check (CRC) bits for error detection purposes. The CRC is calculated as a function of 34-bit sequence using standard generator polynomial of degree 5 as follows [62]:

$$G(x) = x^5 + x^2 + 1 \quad (3.1)$$

The CRC5 can be seen as the remainder obtained by dividing the FCH polynomial with the generator polynomial (3.1). To make CRC5 more robust, guardbands can be used.

In PLC G3, these data symbols are repeated 9 and a half times to allow for receiver synchronization. Thus, the probability of receiver not recognizing a received codeword is reduced [75].

3.4.2 Scrambler

The scrambler is used to introduce random distribution in the data. The bits in the scrambler are all initialized to ones at the start of processing of each frame and are then reinitialized for each FCH and data. A repeating PN sequence is used to XOR the data stream using the generator polynomial as shown below [62]:

$$S(x) = x^7 \oplus x^4 \oplus 1 \quad (3.2)$$

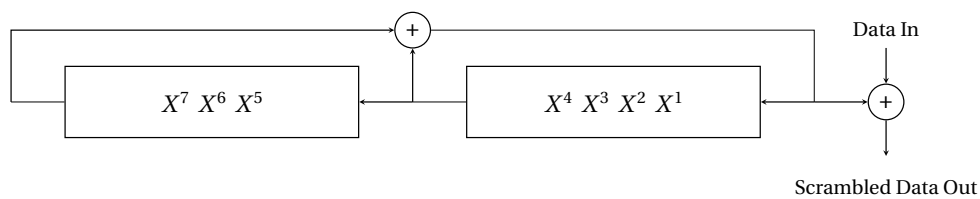


FIGURE 3.5: Data scrambler [4]

3.4.3 Reed-Solomon Encoder

Reed-Solomon codes are most frequently used in digital communication and storage systems due to their efficiency in error correction and are capable of correcting a maximum number of $(n - k)$ errors from any received k number of bits [82]. There are many decoding algorithms [82–84] available for decoding RS codes. The RS encoder is the outer encoder inside the FEC encoder box. The data from the scramble is encoded by shortened systematic RS code using Galois Field (GF) [84]. Thus, a t error-correcting RS code in $GF(2^m)$ has the following properties [62]:

- Block length = $n = 2^m - 1$

- Number of parity-check = $n - k = 2t$
- Minimum distance = $d_{min} = 2t + 1$

Consider (n, k) RS code over the field $GF(2^m)$. If α is the primitive element of $GF(2^m)$, then code generator polynomial $G(x)$ is given by [4]

$$G(x) = \prod_{i=1}^{2t} (x - \alpha^i) \quad (3.3)$$

where $2t = n - k$, t is the error correcting-capability of the RS code, n is the codeword length and k is the message length.

The first bit in time out of the scrambler is the most significant bit (MSB) at the input of RS encoder. Each input at the RS encoder consists of one or more fill symbols followed by the message symbols [83]. The output of the encoder with the exclusion of fill symbols proceed to the input of the convolutional encoder with each message followed by parity symbols [4]. Reed-Solomon encoding is a block coding scheme that is very effective in correcting burst errors that usually occur due to impulsive noise. RS codes are considered optimally effective binary burst error correcting codes and systematic encoding of RS codes involves three steps as follows [85]:

- Multiply the message polynomial $m(x)$ by x^{n-k}
- Divide the result of step 1 by the $G(x)$ and let $d(x)$ be the remainder
- Set $c(x) = x^{n-k}m(x) - d(x)$

The derived codeword $c(x)$ is a multiple of $G(x)$, the degree of $G(x)$ is $(n - k)$, the first $n - k$ coefficients of $x^{n-k}m(x)$ are zeros and only the first $n - k$ coefficients of $d(x)$ are non-zeros [85]. Our system operates in normal mode and as such, a standard RS (255,239) code is used to further enhance the system performance in the presence of hostile power line channel [71].

3.4.4 Convolutional Encoder

The bit stream coming out of the RS encoder proceeds to the input of the convolutional encoder where it is encoded using a standard code rate of $1/2$, constraint length (K) of 7 and generator polynomial of [171 133] [9]. When the last data bit from the RS encoder has been received, the encoder adds six tail bits that are needed to initialize the convolutional encoder to the "zero-state" [62]. These tail bits are regarded as six zeros and are inserted to improve the error probability of the convolutional decoder that depends on the future bits when performing decoding operations [67].

The concept of error control coding is focused on adding parity bits to the encoded message bits before passing them through the channel to the receiver. This technique is used to improve the SNR and BER and as a result, enhance the performance of the system [86]. Convolutional codes are widely used in communication systems for the purpose of error correction. A convolutional encoder consists of shift registers (memory elements) and can be seen as a sequential circuit [5]. Convolutional codes are commonly specified by three parameters: (k) which is the number of input bits (original message bits), (n) which is the number of output bits (encoded bits) and number of memory register (m) [87]. Code rate (r) of a convolutional code expressed as k/n indicates the measure of the efficiency of the code. The constraint length of a convolutional code is defined as the number of bits in the encoder memory that affects the generation of n output bits and is given by $K = k(m - 1)$ [88]. In a convolutional encoder, k number of information bits are convolved with the generator matrix (impulse response of the encoder) to obtain n number of encoded bits [86].

A simple convolutional encoder is shown in Fig. 3.6. The information bits are fed into in groups of k bits into the shift register and the output encoded bits are obtained by modulo-2 addition (*XOR* operation) of the input information bits and the contents of the shift registers which are the previous information bits [7]. The determination of which bits to be added in order to produce the output encoded bit is referred to as generator polynomial $g(x)$ for that output bit [5]. Prior to the encoding operation, the shift register of the encoder is initialized to the all-zero state. Systematic codes have

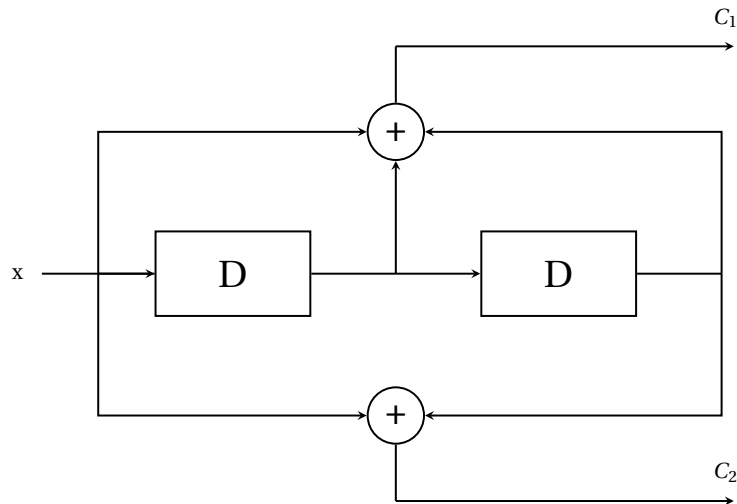


FIGURE 3.6: A convolutional encoder with $k = 1$, $n = 2$ and $r = 1/2$ [5]

advantages over non-systematic such as less hardware requirement for encoding and non-catastrophic nature of the codes which prevents the errors from propagating catastrophically [8]. These properties make systematic codes very desirable in Trellis Coded Modulation (TCM). The operation of a convolutional encoder can be explained in several ways such as state diagram representation, tree diagram representation and trellis diagram representation [7].

3.4.4.1 State Diagram Representation

The operation of a convolutional encoder can be viewed as a finite state machine. The contents of the rightmost $(K - 1)$ stages of the shift register define the states of the encoder [86]. Thus, the encoder depicted in Fig. 3.6 has four states. The transition of the encoder from one state to another is initiated by the input bit as shown in Fig. 3.7 [8]. Insertion of a new input bit (0 or 1) causes the encoder to move from one state to another and the path information between the states denoted as b/c_1c_2 represents the input information bit (b) and corresponding output bits (c_1c_2). The circles represent the states and both input bit and output bits are shown on the arc [7].

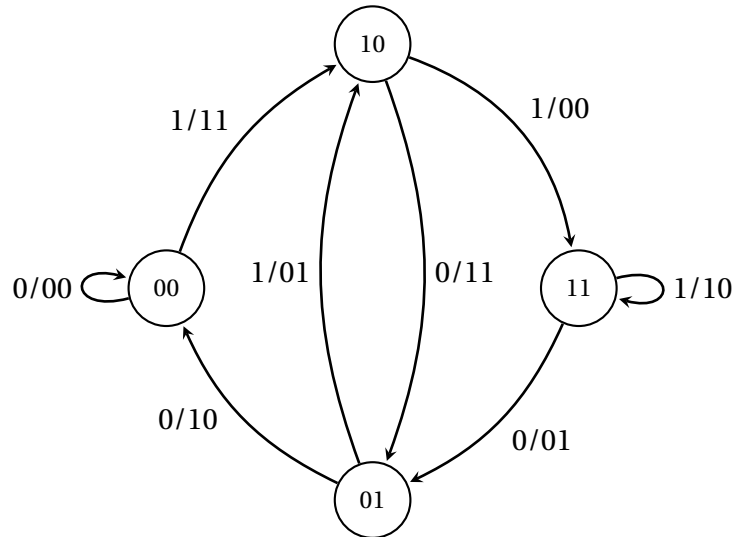


FIGURE 3.7: State diagram of a convolutional encoder with $k = 1$, $n = 2$ and $r = 1/2$ [6]

For example, let us encode the sequence 101100 using the state diagram [6].

1. We start encoding at state 00. The arrival of bit 1 causes the encoder to transit to state 10 and the output bits are 11.
2. Now we are at the new state 10 and arrival of the next bit 0 puts the encoder in state 01 and output bits are 11.
3. We are now at state 01 and arrival of the next bit 1 puts the encoder in state 10 and output bits are 01.
4. Back to 10 as the new state and the next input bit is 1, the encoder transits to state 11 and output bits are 00.
5. At state 11 and the next input bit is 0, the encoder moves to state 01 and output bits are 01.
6. When at state 01 and the next input bit is 0, the encoder moves to state 00 and output bits are 10.

Thus the encoded output bits that are transmitted through the channel are 11 11 01 00 01 10. The receiver does not have a direct knowledge of the transmitter state transitions,

it only sees the received sequence of parity bits with some possible corruptions [16]. Therefore, the receiver is tasked with determining the best possible sequence of the transmitter states that could have generated the received sequence [89].

3.4.4.2 Tree Diagram Representation

The tree diagram is used to show all the possible information and encoded sequence of a convolutional encoder. The Tree diagram of a convolutional encoder with $k = 1$, $n = 2$ and $r = 1/2$ is shown in Fig. 3.8 [90]. The tree diagram allows for direct determination of the encoded bits given an input sequence [7]. Unlike in a state diagram where input bit causes the encoder to move from one state to another, we go down the branches of the tree diagram depending on the value of the input bit (0 or 1) [7]. The first branch indicates the arrival of 0 or 1 and it is assumed that encoding starts at the all zero (00) state. If the input is 1, we go down the branch but if 0 is received, we go up the branch [6]. In Fig. 3.8, the dotted lines show the arrival of bit 1 at the input and solid lines indicate the arrival bit 0. The outputs of the encoder depending on the input bits are shown above the dotted and solid lines.

Let us consider an input sequence 1011. Using the tree diagram, we obtain the encoded output sequence as follows [91]:

1. We go down the first branch since input bit is 1. The output is 11.
2. Next bit at the input is 0. Now we go up the second branch and the output is 10.
3. The next arrival bit is 1, we go down the third branch and the output is 00.
4. Finally the incoming bit is 1 and we go down the fourth branch and the output is 01.

Thus, the encoded output sequence is 11 10 00 01.

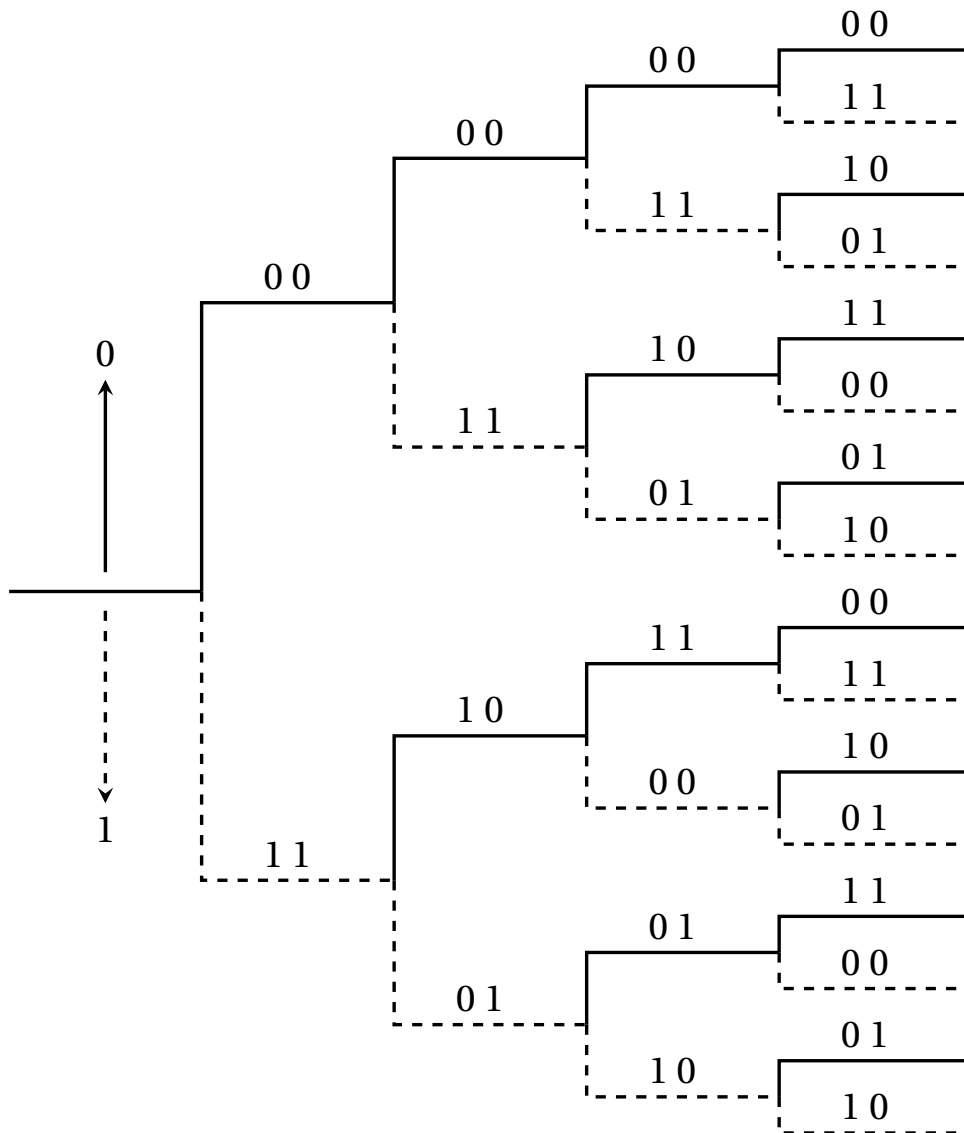


FIGURE 3.8: Tree diagram of a convolutional encoder with $k = 1$, $n = 2$ and $r = 1/2$ [7]

3.4.4.3 Trellis Diagram Representation

Trellis diagram is directly derived from the state diagram of the convolutional code. A Trellis diagram describes the operation of the encoder and can be conveniently used to describe the behavior of the corresponding decoder, especially when the Viterbi decoder is used [8]. The Trellis diagram is preferred to the state or tree diagram because it represents the linear time sequencing of events. The x-axis is the discrete time and all possible states are shown on the y-axis [90]. The Trellis diagram is navigated horizontally with the passage of time and each new bit arrival leads to a new state transition. To

construct a trellis diagram, all possible states are lined up in the vertical axis and each state is connected to the next state by the allowable codewords for that state [16]. There are only two possible options available at each state and these options are determined by the value of the incoming bit [8]. Encoding of the incoming bit starts at state 00 and

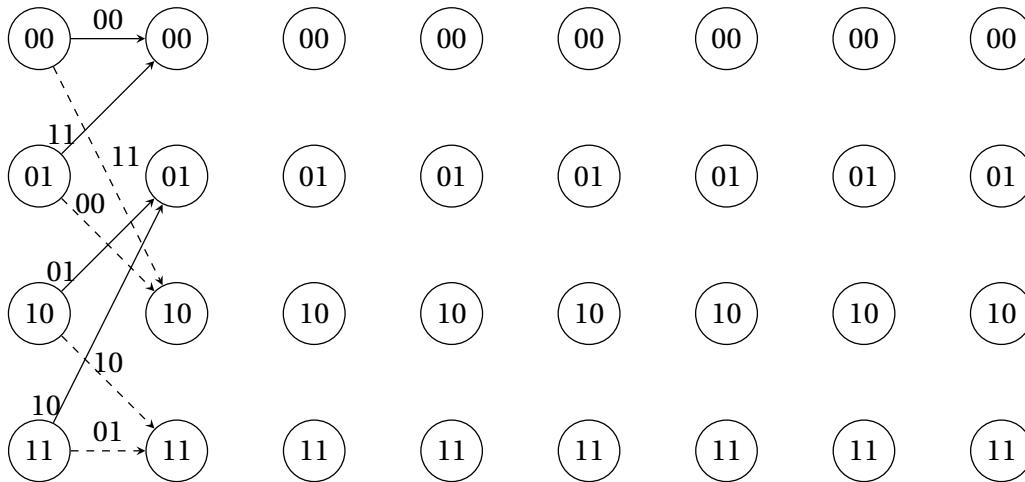


FIGURE 3.9: Trellis diagram for a 4-state convolutional encoder [8]

from there, the trellis expands in K bits and gets populated such that all states transitions are possible. The transitions are then repeated from that point and it should be noted that state, tree and trellis diagrams are unique to each code [5].

In PLC G3, Reed-Solomon and convolutional encoders are aligned in cascade. This technique provides a combined error correction scheme that is capable of combating both random and burst errors that occur in the channel [62].

3.4.5 Interleaver

Interleaving is generally adopted in systems with memory and especially involves convolutional coding due to its capability of handling burst errors [78]. Interleaving in PLC G3 is done with the purpose of spreading an OFDM symbol over other OFDM symbols while ensuring that each OFDM symbol is interleaved [72]. The interleaver is used to protect transmitted signal from being corrupt by frequency deep fading and impulsive noise that are present in the channel [62]. To achieve this protection, a 2D interleaver is used where one interleaves in the frequency domain and the other interleaves

in the time domain. The interleaver is designed in such a way that it provides protection against two different sources of errors [4]:

- i. Burst errors that corrupt a few consecutive OFDM symbols
- ii. Frequency deep fading that corrupts a large number of adjacent OFDM symbols

To combat these problems simultaneously, interleaving is performed in two stages. Stage one involves cyclic shifting in which each column is circularly shifted a different number of times so that a corrupted OFDM symbol is spread across different symbols [62]. During stage two, frequency deep fading is prevented from corrupting the whole column by circularly shifting each row a different number of times [58]. The number of times the circular shift occurs is determined by the parameters that are chosen based on the number of subcarriers in each OFDM symbol and the number of OFDM symbols in each interleaving block [4].

3.5 OFDM System

OFDM is a multicarrier modulation scheme that offers transmission advantages such as spectral efficiency and mitigation of multipath propagation that causes loss of data [4]. To generate an OFDM signal, an inverse fast Fourier transform (IFFT) is carried out on the complex-valued signal points produced by differentially encoded phase modulation and are allocated to individual subcarriers [9, 92]. An OFDM symbol is then formed by appending a cyclic prefix to the beginning of each block generated by the IFFT. The length of the cyclic prefix is selected in such a way that channel group delay does not result in interference between successive OFDM symbols or adjacent subcarriers [62, 93]. After modulation, the IFFT is applied to the data. An IFFT block accepts 256-point IFFT of data and generates 256 time domain samples that are pre-appended using 30 samples of cyclic prefix [94]. Then raised cosine shaping is applied to both data and frame control symbols to minimize out-of-band emission and spectral side lobes [95].

The number of symbols in each PHY frame is dependent on two parameters, namely, the required data rate and the acceptable robustness [9, 92].

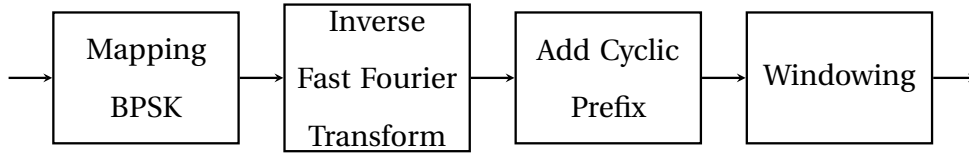


FIGURE 3.10: Components of an OFDM modulator [3]

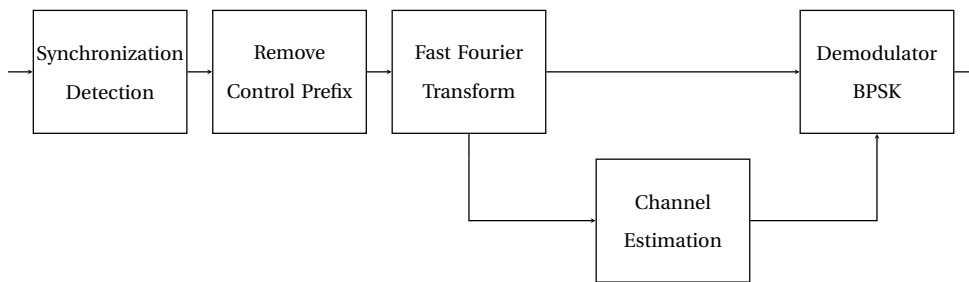


FIGURE 3.11: Components of an OFDM demodulator [9]

OFDM signals are transmitted in parallel using subcarriers at different frequencies. The transmitter utilizes IFFT to generate a sampled waveform [96]. For a given OFDM symbol, let $X(m)$ be the complex number that denotes the constellation point on the m th subcarrier. Then the baseband time domain samples for that symbol are given by [97]

$$x(k) = \frac{1}{N} \sum_{m=0}^{N-1} X(m) \exp\left(\frac{-j2\pi km}{N}\right) \quad (3.4)$$

where N is the IFFT size, $x(k)$ and $X(m)$ are generally complex and frequency domain vector X is constrained to have Hermitian symmetry to ensure that $x(k)$ is real [98].

OFDM efficiently uses the bandwidth within the CENELEC band to allow for advanced channel coding techniques to enable robust communication in the presence of impulsive noise, frequency selective attenuation and NB interference [62, 92]. The link adaptation is achieved through a blind channel estimation technique. The subcarriers with bad SNR are differentiated by the system and are not used to transmit data. The OFDM-based PLC G3 adopted in the PLC system offers the following advantages [9]:

1. Robust communication in the presence of a very hostile PLC channel by transmitting data only on the frequencies that do not have major interference. This is regarded as dynamic tone adoption.
2. In normal mode operation, it provides a minimum of 20 kbps effective data rate during transmission.
3. It also allows for the co-use of S-FSK in a narrowband transmission.

The OFDM adopted in the PLC system uses BPSK modulation scheme per subcarrier in order to support up to 33.4 kbps data rate during normal mode transmission. To detect the phases of the current carriers, the phases of the carriers in the adjacent symbols are used as reference [75].

3.5.1 Binary Phase Shift Keying

The BPSK modulation scheme has been adopted over the years in wireless communication for data modulation. There have been many research investigations done to analyze the performance of the BPSK scheme in comparison to the QPSK method [10]. These investigations have shown that BPSK offer better BER performance than QPSK because BPSK provides acceptable BER when transmitting signals with relatively low energy and it also provides high immunity to channel noise [10, 99].

The BPSK scheme uses two points located 180° apart to represent the binary information. These points can be plotted anywhere in the Cartesian plane provided that an angle of 180° is maintained between the points as shown in Fig. 3.12. This technique is referred to as a constellation or mapping [99]. These real signals can be written as the vector sum of two signals in quadrature called I and Q space. The I-Q amplitudes can be seen as the x and y projections of the signal computed as follows [10].

$$\begin{aligned}
 I_{amplitude} &= (\text{symbol expression})\cos(\text{phase}) \\
 Q_{amplitude} &= (\text{symbol expression})\sin(\text{phase})
 \end{aligned}
 \tag{3.5}$$

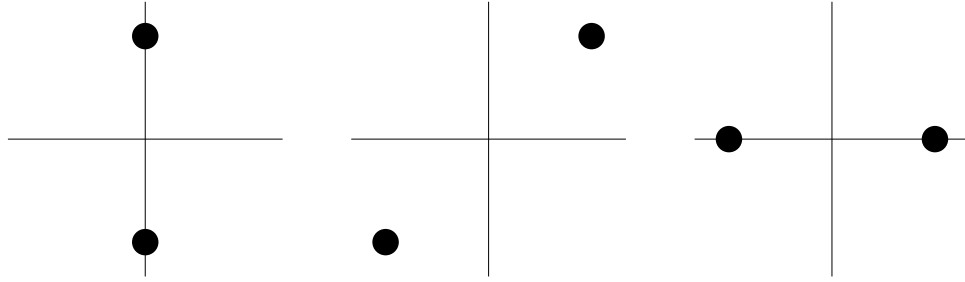


FIGURE 3.12: Binary information representation using BPSK modulation scheme [10]

Thus, it can be easily observed from (3.5) that $I = 1$ for the first symbol and -1 for the second symbol. The amplitude of Q on the other hand is zero for both symbols since $\sin(0^\circ) = \sin(180^\circ) = 0$ [100]. The mapping rules that must be observed when using the BPSK scheme are illustrated in Table 3.3

TABLE 3.3: Mapping procedure for BPSK scheme using two cosine signals [10]

Symbol	Bit	Expression	I	Q
S_1	0	$\sqrt{\frac{2E_b}{T}} \cos(\omega t)$	1	0
S_2	1	$\sqrt{\frac{2E_b}{T}} \cos(\omega t + \pi)$	-1	0

The carrier signals associated with the bits are transmitted rather than the bits themselves [101]. To illustrate how the expressions in Table 3.3 are derived, it was assumed that the frequency of the carrier signal is 1, i.e. $f_c = 1$ and express the BPSK waveform as follows [101]:

$$S_b(t) = \sqrt{\frac{2E_b}{T_b}} \cos(\omega t + \pi(1 - n)) \quad (3.6)$$

For binary bit 0 and taking $n = 0$, we have that

$$\begin{aligned} S_0(t) &= \sqrt{\frac{2E_0}{T_0}} \cos(\omega t + \pi(1 - 0)) \\ &= \sqrt{\frac{2E_0}{T_0}} \cos(\omega t + \pi) \end{aligned} \quad (3.7)$$

For binary bit 1 and taking $n = 1$, we have that

$$\begin{aligned} S_1(t) &= \sqrt{\frac{2E_1}{T_1} \cos(\omega t + \pi(1 - 1))} \\ &= \sqrt{\frac{2E_1}{T_1} \cos(\omega t)} \end{aligned} \quad (3.8)$$

where E_0 and E_1 are the bit energies associated with the first and second signals respectively. The BPSK bit error rate is the given by [102]

$$P_b = \frac{1}{2} \operatorname{erfc} \sqrt{\frac{E_b}{N_0}} \quad (3.9)$$

where E_b is the bit energy and N_0 is the noise power spectral density.

The same OFDM system used in the PLC system is used in VLC system but it is modified to suit the unique properties of VLC signals, such as non-negative value of VLC signal since light intensity cannot be negative [63]. There are two methods that are commonly used to generate non-negative signal: DC biased optical OFDM (DCO-OFDM) [63, 64] and asymmetrical clipped optical OFDM (ACO-OFDM) [98, 103]. In this research, DCO-OFDM was adopted in the VLC system as it offers better spectral efficiency than ACO-OFDM [11].

3.5.2 DCO-OFDM System

Most of the optical wireless systems used for communications adopt intensity modulated/direct detection scheme due to its cost efficient property and this technique ensures that only real and non-negative signals are transmitted [11]. At the transmitter, real signals can be generated using the IFFT that sacrifices half of the spectral efficiency by making use of only signals with Hermitian symmetry at the input [98].

In DCO-OFDM, negative signals are made positive by adding a DC bias to normal OFDM signals [104]. This increases the power requirement of the system since OFDM signals require very high peak-to-average ratio resulting in the use of very high bias to eliminate

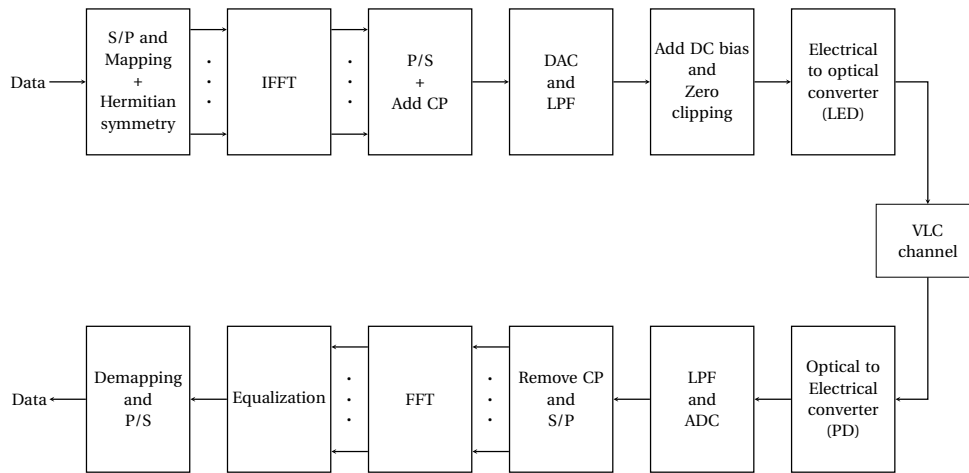


FIGURE 3.13: DCO-OFDM system [11]

all negative peaks [11]. However, only a moderate bias is used and the remaining negative peaks are clipped to zero resulting in clipping noise affecting both odd and even subcarriers [98].

DCO-OFDM is used to convert a bipolar OFDM signal into a unipolar signal. Adding a DC bias to an OFDM signal has an adverse effect on both power requirement and performance [98]. The performance of DCO-OFDM is determined by the bias level and optimum bias that can be added depends on the size of the constellation being used. Adding a small bias results in clipping noise that hampers performance while a large bias increases the amount of required power [104]. DCO-OFDM offers data rate that is twice that of ACO-OFDM as a result of Hermitian symmetry. Thus, there are $N/2$ independent complex inputs for an N IFFT point for a given constellation size [105].

3.6 The Impulsive Noise Model for PLC Channel

The PLC channel is well known to be very noisy and hostile for data communication. Its characteristics constantly change with frequency, time, location and type of loads that are connected to it [66]. The PLC channel is frequency selective and low frequency harmonics (10 kHz to 200 kHz) are mostly affected by interference [65, 69]. In addition to white noise that is always present, power line channel is typically subjected to background noise, impulsive noise, frequency selective fading and narrowband interference

[4]. Noise affecting OFDM subcarrier signals in PLC channel is modeled as AWGN only in frequency domain due to Fourier transform of the received signal. However, in the time domain, PLC channel is affected by non-AWGN [2]. Noise that occur in PLC channel is a combination of impulsive noise (synchronous and asynchronous), Gaussian background noise, and narrowband interference as described in [2, 65, 80, 106, 107]. Due to all these factors, there has been a lot of research investigation in modeling of such a complex channel as shown in [66, 108–110].

The PLC channel adopted in this research is modeled as Middleton Class-A noise model. Additionally, additive white Gaussian noise (AWGN) component is added to model the ever present thermal noise produced by the receiver. This model has been widely adopted in many literatures to model the effects of impulse noise in a communication systems [65, 106, 107, 111–116]. The probability density function (PDF) of a noise sample, z_p given by Middleton Class-A is represented as [12]

$$F(z_p) = \sum_{m=0}^{\infty} P_m N(z_p; 0, \sigma_m^2) \quad (3.10)$$

where $N(z_p; \mu, \sigma^2)$ denotes a Gaussian PDF with the mean μ and variance σ^2 from which the sample is taken.

$$P_m = \frac{(e^{-A})A^m}{m!} \quad (3.11)$$

and

$$\sigma_m^2 = \sigma_I^2 + \sigma_g^2 = \sigma_g^2 \left(\frac{m}{A\Gamma} + 1 \right) \quad (3.12)$$

where σ_I^2 is the variance of the impulse noise and σ_g^2 is the variance of the background noise (AWGN). The parameter m is the random noise state that describes each sample and is chosen from the set $m \in (0, 1, 2, \dots, \infty)$ and has a Poisson-distribution that is given by (3.11). The parameter $\Gamma = \sigma_g^2 / \sigma_I^2$ is the ratio of the mean power of the Gaussian component to mean power of the impulsive noise component [115]. It should be noted that if z_p is completely AWGN then Γ approaches ∞ . However, when $\Gamma \neq 0$ and $m = 0$, the noise component is completely Gaussian [2]. Therefore, it can be concluded

that the Middleton Class-A PDF presented in (3.10) is simply the summation of all the conditional-Gaussian PDFs multiplied by the probabilities of occurrence of the associated states [107]. The parameter A is the density of impulses within an observation period. Thus, it can be represented as $A = \eta\tau / T_0$, where η is the average number of impulses per second and τ is the average duration of each impulse and all impulses are assumed to have the same duration [12]. Noise samples are assumed to be i.i.d. (independent and identically distributed) and each noise sample has a Gaussian distribution and densities of the impulse noise are shown to occur according to the Poisson distribution (3.11). The density of the impulse noise is accepted as impulsive index $A \leq 1$ and during observation period T_0 , if $\eta\tau > T_0$ then A is set to 1 no matter how large $\eta\tau$ is [2]. It is worth noting that whether impulses occur in burst (one after the other) or at separate intervals, the calculation of impulsive index follows the same procedure [12]. The signal to noise ratio (SNR) of PLC channel is given by [2]

$$SNR_p = \frac{E[|h_p x|^2]}{\sigma_m} \quad (3.13)$$

where the expected value is calculated over all possible values of x . If the impulse noise is too high, then impulsive noise powers may be in the orders of magnitude greater than that of AWGN [111]. In a situation like this, low values of SNR_p are considered only when characterizing the system performance since SNR_p is determined by the total noise [106]. The capacity of the PLC channel is given by [2]

$$C_p = \log_2(1 + SNR_p) \quad (3.14)$$

A two-state representation of Middleton Class-A is shown in Fig. 3.14. It can be seen

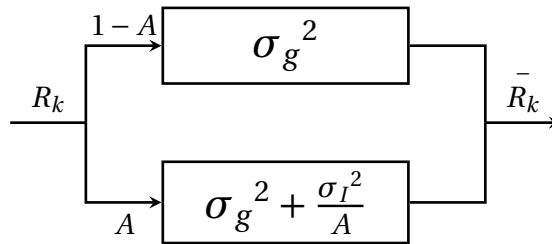


FIGURE 3.14: Middleton Class-A model for two-state PLC channel [12]

from this model that only the state with variance σ_g^2 has Gaussian distribution and the state with impulse noise does not necessarily have a Gaussian distribution [65]. The process by which each OFDM symbol R_k is affected by impulse noise is illustrated in Fig. 3.14, where the channel also has additive white Gaussian noise (AWGN) [107]. Each data symbol entering the channel is either corrupted by only AWGN noise having a variance of σ_g^2 with a probability $1 - A$ or is corrupted by both AWGN and impulse noise having a variance of $\sigma_g^2 + \sigma_I^2$ with a probability of A [72]. Impulse noise variance for the states with impulse noise is divided by the probability (A) of entering into that state resulting in impulse noise variance of the system being σ_I^2 [68]. From (3.10)–(3.12), it can be observed that impulse noise variance of state m is (σ_I^2/m) as given by (3.12) and this state variance occurs with probability P_m as shown in (3.11) [2]. Thus, the average impulse noise variance of Middleton Class-A noise model can be expressed as [12]

$$\sum_{m=0}^{\infty} P_m \frac{\sigma_I^2 m}{A} = \frac{\sigma_I^2}{A} \sum_{m=0}^{\infty} m P_m = \left(\frac{\sigma_I^2}{A} \right) A = \sigma_I^2 \quad (3.15)$$

From a simulation point of view and assuming that N OFDM symbols are transmitted, the derivation of (3.15) can be explained as follows: each symbol in the vector length N must be affected by impulse noise variance σ_I^2/A and as such it can be shown that this will result in impulse noise over the N symbols being σ_I^2 [116]. This is because impulse noise occurs with the probability of A and for N symbols (provided that N is very large), it can be seen that approximately AN symbols are affected by the impulse noise having a variance of σ_I^2/A [113]. And as a result, the impulse noise in the N samples can be expressed as $\sigma_N^2 = AN(\sigma_I^2/A) = N\sigma_I^2$ and the average impulse noise variance over N symbols will then be given as $\sigma_N^2/N = \sigma_I^2$ which is same result obtained in (3.15) [12]. The Middleton Class-A noise distribution is used to model noise in a PLC channel because of the simplicity of its PDF, since it has only three parameters of interest: the impulsive index, A , which characterizes the impulsiveness of the noise, Gaussian to impulsive noise power ratio, Γ and the total variance of the PLC Class-A noise, σ_m [72]. In addition, it allows noise sources to be constructed and simulated using real world measured data. Thus, noise characteristics can be quantified based on real world measurements [2].

3.7 The LOS Propagation Model for VLC Channel

The VLC system shown in Fig. 3.1 has a physical layer that is also modeled according to PLC G3 physical layer specification [4]. The VLC channel is the space between the transmitter (LED) and the receiver photodetector (PD) [30]. The VLC channel adopted in this research is modeled as a line of sight (LOS) propagation model. In directed LOS transmission, reflections are neglected and path loss is calculated using the transmitter's beam divergence, receiver's size and separation distance [14]. The configuration of topology that is adopted in this model is classified according to [13]:

1. Degree of directionality of the transmitter and the receiver
2. Existence of LOS between the transmitter and the receiver

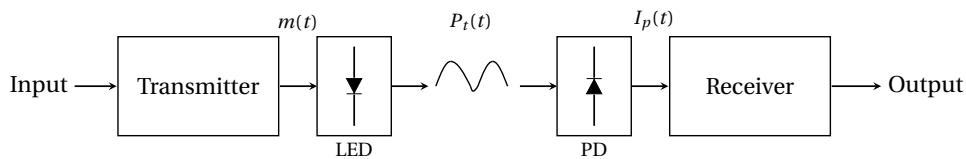


FIGURE 3.15: Optical intensity direct detection communication channel [13]

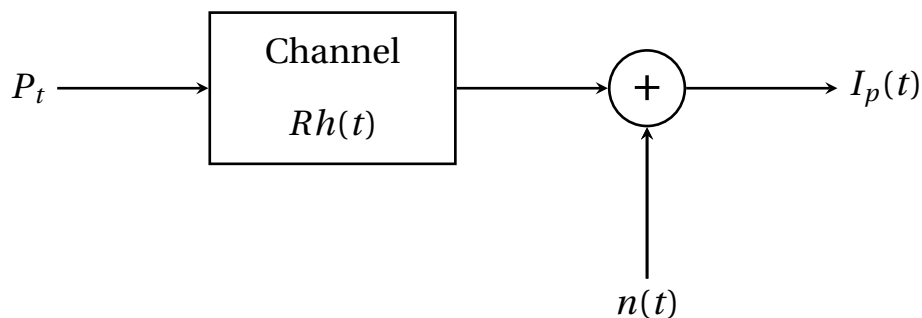


FIGURE 3.16: Equivalent diagram of VLC channel model using IM/DD [13]

The drive current of the source is directly modulated by modulating the signal $m(t)$ that varies the intensity of the source P_t as depicted in Fig. 3.15 [13]. The photodetector (PD) at the receiver's side has a response that is equivalent to the integration of numerous

short wavelengths of the incoming optical signal that produces a photocurrent $I_p(t)$ [117] and this signal can be represented as [13]

$$I_p(t) = RP_t(t) \otimes h(t) + n(t) \quad (3.16)$$

where R is the PD responsivity, $P_t(t)$ is the instantaneous optical transmitted power, $h(t)$ is the channel impulse response, $n(t)$ is the AWGN with a double-sided power spectral density (PSD) of $N_0/2$ representing the shot noise produced by the signal and \otimes denotes convolution [13]. The effects of dispersion experienced in the indoor optical wireless communication (OWC) is modeled as a linear baseband channel impulse response $h(t)$ [118]. The characteristics of an OWC channel can be considered fixed for a certain position of the transmitter, receiver and intervening reflecting objects. The channel characteristics only change when the positions of these parameters have been altered in order of centimeters [14].

3.7.1 LOS Propagation Model

Indoor OWC uses LED as its source and PD with large area as the receiver [29]. The angular distribution of the radiation intensity pattern can be modeled according to generalized Lambertian radiant intensity and its distribution is given by [13]

$$R_0(\phi) = \begin{cases} \frac{(m_1+1)}{2\pi} \cos^{m_1}(\phi) & \phi \in [-\pi/2, \pi/2] \\ 0 & \phi \geq \pi/2 \end{cases} \quad (3.17)$$

where m_1 is the Lambertian emission order indicating the directivity of the source beam, ϕ is the angle of radiated power which is maximum at $\phi = 0$ [29]. The relationship between m_1 and LED semi-angle at half-power $\Phi_{1/2}$ is given by [119]

$$m_1 = \frac{-\ln 2}{\ln(\cos \Phi_{1/2})} \quad (3.18)$$

and the radiant intensity is calculated as follows [13]

$$S(\phi) = P_t \frac{m_1 + 1}{2\pi} \cos^{m_1}(\phi) \quad (3.19)$$

The PD is modeled as an active area A_r that traps the incident radiation at an angle Ψ that is smaller than the detector's field of view (FOV) [14]. Since the incident radiation cannot occupy the entire A_r , the effective area of the PD can be defined as [29]

$$A_{eff}(\Psi) = \begin{cases} A_r \cos \Psi & 0 \leq \Psi \leq \pi/2 \\ 0 & \Psi > \pi/2 \end{cases} \quad (3.20)$$

To collect as much power as possible at the receiver, a PD with large area is often deployed but there are issues that affect the choice of large area PD such as increased cost, increased junction capacitance resulting in reduced receiver's bandwidth and increased receiver's noise [120]. However, non-imaging concentrator which is cost effective can be used to increase the overall effective area [121]. For an ideal non-imaging concentrator with internal refractive index of n , the optical gain is given by [13]

$$g(\Psi) = \begin{cases} \frac{n^2}{\sin^2 \Psi_c}, & 0 \leq \Psi \leq \Psi_c \\ 0, & \Psi > \Psi_c \end{cases} \quad (3.21)$$

where $\Psi_c \leq \pi/2$ is the FOV. The relationship between FOV of the receiver's system and area of lens A_{coil} and PD area according to constant radiance theorem can be expressed as [13]

$$A_{coil} \sin \frac{\Psi_c}{2} \leq A_r \quad (3.22)$$

From (3.22), it can be seen that reduction in FOV results in increase in concentrator gain.

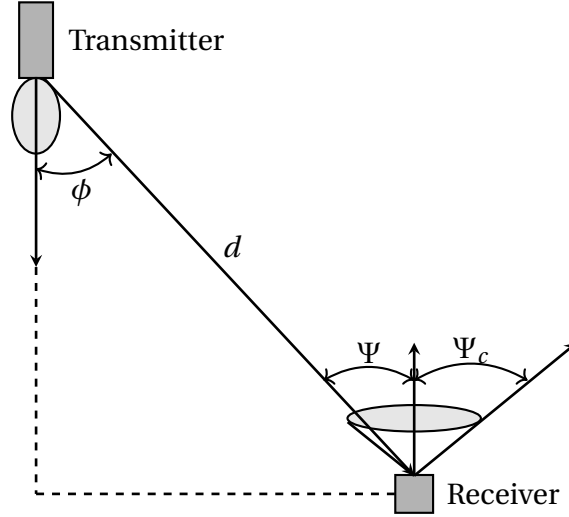


FIGURE 3.17: LOS propagation model [14]

In an indoor OWC, attenuation due to absorption and scattering is relatively low due to the short length of the OWC link [117]. For a receiver with an optical bandpass filter of transmission $T_s(\Psi)$ and a non-imaging concentrator of gain $g(\Psi)$, the DC gain for the receiver located at distance d from the source and angle ϕ with respect to the source as shown in Fig. 3.17 can be approximated as [13]

$$H_{LOS}(0) = \begin{cases} \frac{A_r(m_1+1)}{2\pi d^2} \cos^{m_1}(\phi) T_s(\Psi) g(\Psi) \cos(\Psi), & 0 \leq \Psi \leq \Psi_c \\ 0, & \text{otherwise} \end{cases} \quad (3.23)$$

Thus the received power is then given by [14]

$$P_{r-LOS} = H_{LOS}(0) P_t \quad (3.24)$$

The increase in an LOS signal as a result of aligning the source and the receiver is expressed as [13]

$$H_{LOS}(m_1) = \frac{(m_1 + 1)}{2} H_{LOS} \quad (3.25)$$

where H_{LOS} is used to indicate a Lambertian source with $m_1 = 1$ [121]. In a short-distance LOS link (as investigated in this research work), multipath dispersion is considered non-existent and LOS channel is modeled as a linear attenuation and delay [118]. The LOS link is considered as non-frequency selective resulting in path loss being solely

dependent on the square of the distance between the source and the receiver [29]. Consequently, the impulse response of the LOS channel is given by [122]

$$H_{LOS}(t) = \frac{A_r(m_1 + 1)}{2\pi d^2} \cos^{m_1}(\phi) T_s(\Psi) g(\Psi) \cos(\Psi) \delta\left(t - \frac{d}{c}\right) \quad (3.26)$$

where c is the speed of light in the free space, $\delta(\cdot)$ is the Dirac function and $\delta(t - d/c)$ is the signal propagation delay [122]. There are few assumptions that were made in order to realize the expression in (3.26) [120]

- i The angle of orientation between the source and the receiver is less than 90° . That is, $\phi < 90$.
- ii The angle at which radiation is incident on the active area is less than the FOV. That is, $\Psi < \text{FOV}$.
- iii And lastly, the distance of separation between the source and the receiver is much greater than the square root of the active area. That is, $d \gg \sqrt{A_r}$.

The time average optical transmitted power is given by [14]

$$P_t = \lim_{T \rightarrow \infty} \frac{1}{T} \int_0^T P_i \quad (3.27)$$

The average received optical power is expressed as $P_r = H(0)P_t$, where $H(0)$ is the DC channel gain given in (3.23) [13].

3.7.2 SNR Analysis

VLC transmission is affected by noise produced by sources such as sunlight, incandescent and fluorescent light present in the operating environment [30]. Additionally, the receiver produces thermal and shot noise as a result of photon's impact. The thermal noise is produced as a result of energy equilibrium fluctuations and shot noise is produced as a result of current fluctuations [29]. The variance of the total noise affecting

transmission in VLC system is the summation of the variances of the shot and thermal noise [30]

$$\sigma_n^2 = \sigma_{shot}^2 + \sigma_{th}^2 \quad (3.28)$$

where

$$\sigma_{shot}^2 = 2Bq [RP_r + I_B I_2] \quad (3.29)$$

and

$$\sigma_{th}^2 = \frac{8\pi K T_k}{G_{ol}} C_{pd} A I_2 B^2 + \frac{16\pi K T_k \Gamma}{g_m} C_{pd}^2 A^2 I_3 B^3 \quad (3.30)$$

where q is the electric charge, P_r is the received average optical power, B is the noise bandwidth, I_B is the photocurrent due to background radiation, R_r is the photoreceiver responsivity, ζ is the factor related to noise bandwidth, K is Boltzmann constant, T_k is the absolute temperature, A is the detection area, G_{ol} is the open-loop voltage gain, and g_m is the field effect transistor (FET) transconductance, Γ is the FET channel noise factor and noise bandwidth factors I_2 and I_3 are 0.562 and 0.0868 respectively [61, 123]

Considering inter-symbol interference (ISI) resulting from multipath propagation, the received power due to ISI affects the SNR [124]. In VLC systems, the noise vector appears as the combination of shot and thermal noise and it is assumed that the total noise is dominated by AWGN. Therefore the SNR is given by [30]

$$SNR_v = \frac{R_r^2 P_r^2}{\sigma_n^2} \quad (3.31)$$

The capacity of the channels is expressed by [3]

$$C_v = \log_2[1 + SNR_v] \quad (3.32)$$

The noise affecting both PLC and VLC OFDM subcarrier signals was modeled as additive white Gaussian noise (AWGN) in both channels since AWGN represents a good model

in the frequency domain due to the Fourier transform of the received samples [2].

3.8 Summary

There are nine sections in this chapter. Introduction to what to expect in this chapter was provided in Section 3.1 and the system model that is used in this research investigation and how the OFDM system was modified in the VLC system to eliminate the possibility of transmitting bipolar signal was described in Section 3.2. In Section 3.3, the PLC G3 physical layer that was adopted in modeling both PLC and VLC physical layers of the system used in this research investigation Fig. 3.1 was presented. Furthermore, the operation mechanism of the PLC G3 system model was described in details in this section. Section 3.4 discussed the various components that make up the parallel PLC-VLC system model and how each component plays an important role in combating both random and burst errors, reducing multipath fading and frequency deep fading. Sections 3.5 and 3.6 analyzed the role the PLC OFDM and VLC DCO-OFDM play in helping our system achieve better system performance. The modulation scheme adopted in the OFDM system was described in Section 3.7 and it was stated why BPSK modulation scheme was chosen over QPSK modulation scheme. Section 3.8 provided detailed analysis of the noise model for PLC channel and showed that by modeling the PLC channel as an impulsive noise model with Middleton Class-A noise distribution, it is possible to quantify the noise sources based on real world measurements. Finally in Section 3.9, the VLC channel model was presented as a LOS propagation model that is affected by attenuation and it was showed that the power of signal available at the receiver can be hugely affected by the angle of orientation and effective area of the receiver depending on the distance of separation between the source and the receiver.

Chapter 4

JOINT DECODING SCHEME

4.1 Introduction

The parallel combination of PLC and VLC networks offers a good option for high-speed communication and good signal quality. To further harness the advantages presented by a system of this topology and improve the overall system performance, a joint decoding technique is proposed in this research. This technique has been used in many applications and the results demonstrated by these applications show significant improvement in the system performance in terms of BER, spectral efficiency, throughput and signal quality [2, 47–51]. This chapter first presents a benchmark decoding scheme, and the issues that are encountered in this type of approach led to the idea of joint decoding as an alternative to overcoming these problems. To carry out the joint decoding technique, decoding algorithms such as Viterbi and Berlekamp-Massey algorithms are considered for joint decoding at the convolutional and Reed-Solomon decoders respectively. The chapter concludes with looking at the concept of erasure decoding to further improve decoding performance and scenarios and cases used in applying joint decoding are described.

4.2 Benchmark Decoding Scheme

The FEC decoder shown in Fig. 3.1 consists of Reed-Solomon and convolutional decoders in cascade [4]. Thus, in conventional decoding, each channel (PLC or VLC) is decoded separately using its own FEC decoder. This scenario represents the benchmark decoding scheme that is used to formulate our system model and is depicted in Fig. 4.1.

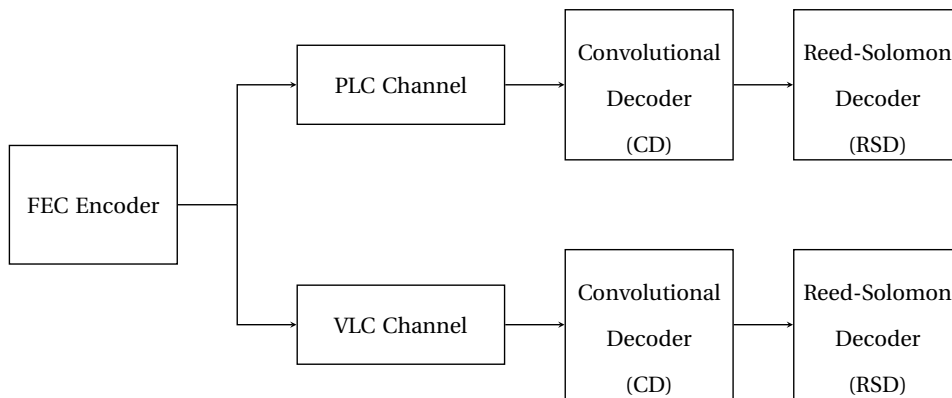


FIGURE 4.1: Block diagram of separate decoding

The scenario presented in Fig.4.1 involves using two decoders in each channel (four decoders in total) to decode the received codeword. This technique increases the decoding and implementation complexity since two decoders are used in each channel [125]. One way of overcoming this problem is to use a joint decoding technique. Thus, this research proposes joint decoding of parallel PLC-VLC systems.

4.3 Joint Decoding

Joint decoding is a technique that combines the received codewords from two different channels into one codeword and then decodes the combined codeword using one or more decoders. Many applications have deployed joint decoding techniques to improve system performance. In [84], joint decoding was applied in overloaded MIMO-OFDM system to improve the BER performance of the system, it was also used in [47] to

enhance the image quality, and in [48, 50, 51] to increase the spectral efficiency of the system. Furthermore, joint decoding has been used to provide diversity in many applications such as in [2, 3] where it was used in an indoor application to decode a parallel PLC and Wi-Fi system in order to explore media diversity in an office environment. They used both coding and modulation diversities to enable efficient use of parallel transmission channels. In [38], binary information transmitted over different parallel channels was decoded using one maximum-likelihood (ML) decoder and in [39], ML joint decoding was also used to decode Turbo-like code transmitted over multiple parallel channels. A hybrid FSO/RF communication system was decoded in [40, 41] using a joint decoding technique to optimize combined capacity and improve system reliability. The information from FSO and RF channels were combined at the receiver using a bit metrics multiplexer and decoded using a binary decoder [41].

One of the objectives of this research is to apply joint decoding to the system shown in Fig. 4.1. Thus, the codewords from the channels will first be combined and then decoded either at the inner or outer decoder. The main advantage that this system has is that it is optimized to the sum of the capacities of the two channels (i.e. $C_{PLC} + C_{VLC}$) instead of individual channel capacities C_{PLC} and C_{VLC} [40] and also improves the power spectral density (PSD) of the system [49].

4.3.1 Joint Decoding at the Convolutional Decoder

To perform joint decoding at the convolutional decoder, the information coming from both PLC and VLC channels are first combined at the output of both channels and decoded using only the convolutional decoder. This process is regarded as joint soft decision decoding (JSDD) at the convolutional decoder and is carried out using the Viterbi algorithm. This scenario is shown in Fig. 4.2.

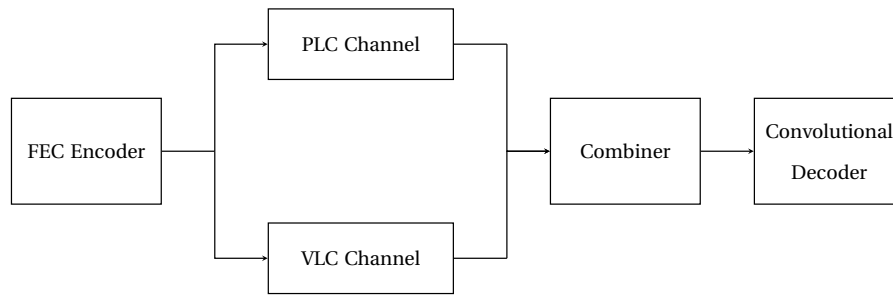


FIGURE 4.2: Block diagram of joint soft decoding technique at the convolutional decoder

Another way of performing joint decoding at the convolutional decoder is to first pass the information coming from both channels through their individual demodulators and then combine the bits at the output of both decoders. This approach is regarded as joint hard decision decoding (JHDD) and is carried out using the Viterbi algorithm. This scenario is shown in Fig. 4.3.

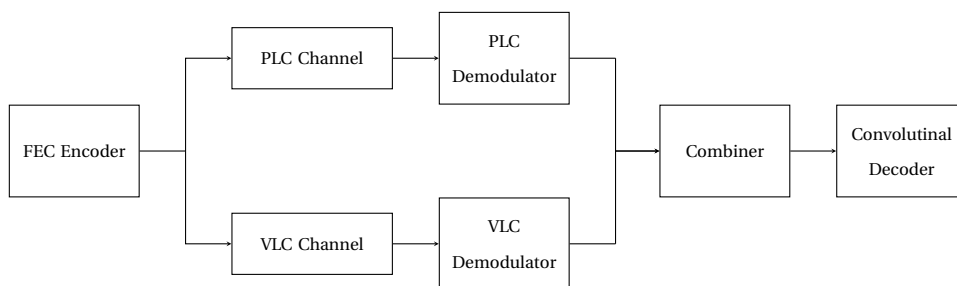


FIGURE 4.3: Block diagram of joint hard decoding technique at the convolutional decoder

In applying the joint decoding technique on the hard information combined after the demodulators, the erasure decoding technique is used in order to improve the BER performance of the system. Besides the convolutional decoder, joint decoding is also applied at the Reed-Solomon decoder.

4.3.2 Joint Decoding at the Reed-Solomon Decoder

At the Reed-Solomon decoder, only one option is available for application of the joint decoding technique. That is, only joint hard decision decoding can be performed since

the information at the output of the convolutional decoder is regarded as hard bits (1 or 0). Adopting this approach requires the information at the output of the channels to be first decoded separately using convolutional decoder. The outputs of the two convolutional decoders are combined and then decoded again using one Reed-Solomon decoder as shown in Fig. 4.4. The Berlekamp-Massey algorithm is used in the Reed-Solomon decoder.

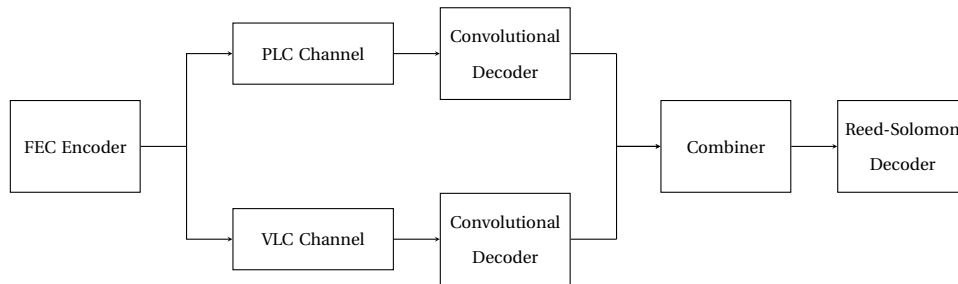


FIGURE 4.4: Block diagram of joint hard decoding technique at the Reed-Solomon decoder

The diagrams in Figs. 4.2, 4.3 and 4.4 show the application of the joint soft decoding technique at the convolutional decoder, joint hard decoding technique at the convolutional decoder and joint hard decoding at the Reed-Solomon decoder respectively. The information bit streams to be transmitted are encoded using a single FEC encoder (Reed-Solomon encoder in cascade with convolutional encoder) and then transmitted through different channels [4]. At the receiver, joint decoding is applied on the coded signal using hard decision decoding (HDD), Viterbi decoding for the convolutional code and Berlekamp-Massey decoding for the Reed-Solomon code [9]. The HDD of convolutional codes can be implemented using either a sequential algorithm or Viterbi algorithm but in this research, the Viterbi algorithm has been adopted for HDD of the convolutional codes as it offers maximum likelihood (ML) decoding and is very suitable in correcting random errors [15, 86]. Furthermore, the Berlekamp-Massey algorithm is used for the Reed-Solomon code due to its strong error correction mechanism (capable of correcting both random and burst errors) [126]. In Fig. 4.2, soft information from the two channels are combined and then decoded at the inner (convolutional) decoder, in Fig. 4.3, hard information are combined at the output of the demodulators and decoded at the convolutional decoder and in Fig. 4.4, hard information bits at the output of the

two convolutional decoders are combined and decoded at the outer (Reed-Solomon) decoder.

To carry out joint decoding, it is important to use decoding algorithms that are efficient in error correction. To perform both the JSDD and JHDD at the convolutional decoder, the Viterbi algorithm is used and to perform the JHDD at the Reed-Solomon decoder, the Berlekamp-Massey algorithm is used.

4.4 Hard Decision Decoding of Convolutional Code

The Viterbi algorithm is used for decoding convolutional codes due to its suitability for correcting random errors [6, 127]. The Viterbi algorithm finds the maximum likelihood (ML) estimate of the transmitted sequence \mathbf{c} from the corresponding received sequence \mathbf{r} through the maximization of the probability $p(\mathbf{r}/\mathbf{c})$ provided that sequence \mathbf{r} is received conditioned on the estimated code sequence \mathbf{c} [15]. The transmitted sequence \mathbf{c} must be a valid codeword [16].

The channel used for transmission is assumed to be memoryless in the sense that the noise sample affecting one received bit is independent from the one affecting the other bits [6]. The Viterbi algorithm uses trellis diagram to compute path metrics and decoding operation starts at the 00 state [90]. When a corrupted codeword is received, the branch metric of each branch is determined by calculating the Hamming distance (the dot product of the received codeword and the allowable codeword) of the received codeword from the valid codeword associated with the branch [8]. Path metrics of all the branches associated with all the states are also calculated in the same way. At the receiver, the code trellis is generated and the decoder navigates through the code trellis state by state searching for the transmitted codeword [16]. At each state of the code trellis, the decoder performs three functions that make up the decoding procedure. It does computation, addition and selection (CAS) [15]. It basically solves an optimization problem by navigating from one state of the trellis to another capturing errors introduced in the received sequence, accumulating these errors along a path and generating

the estimate of the total number of errors along the path [87]. The path with the smallest number of errors is stored as the survival path [128]. The Viterbi algorithm is a maximum likelihood decoder that determines the most likely path. It takes advantage of future knowledge to break ties which may result in paths previously considered as most likely at some point to change [15, 127].

The golden rule in Viterbi decoding is that prior to decoding, the shift register is initialized to all zero-state [128]. This implies that no matter what has been received, decoding starts at all zero-state and then make transitions to a new states [90]. In search of the encoded sequence, Viterbi algorithm performs three tasks at each current state [15]:

- Computation - it computes branch and path metrics for the previous state leading to the new state.
- Addition - it adds branch and path metrics for all paths arriving at the current state.
- Selection - it selects the path with the largest metric between the initial and the current states. This is the path with the smallest accumulated errors up to the current state [129].

TABLE 4.1: Hamming metric based on what was received and the valid codewords at that state [6]

Received Bits	Valid Codeword 1	Valid Codeword 2	Hamming Metric 1	Hamming Metric 2
00	00	11	2	0
01	10	01	0	2
10	00	11	1	1

The metrics are accumulated along each path so the path with the lowest metric is chosen as the most likely path [128]. From the trellis diagram shown in Fig.3.9, it can be seen that each state can be reached through two paths from the previous state and the path with the lowest accumulated path metric is chosen [15]. The basic operations of the Viterbi algorithm in decoding a received codeword are summarized below [6]:

- i. Determine the branch metrics of all the states.

- ii. The accumulated path metrics of all the paths leading to a new state are calculated taking into account the accumulated path metrics of the previous states from where the most recent branches emerged.
- iii. Out of all the paths entering into the new state, only the path with the minimum accumulated path metric is chosen as the survivor path.
- iv. The information bits associated with the branches making the paths are stored.
- v. Trace back the history of the survival path to identify the codeword associated with the first branch of the path and accept this codeword as the most likely transmitted first codeword.

The above procedure is then repeated for each received codeword and a decoding decision is only made once all the codewords have been received [15]. Let us decode a received sequence 01 11 01 11 01 01 11 for a (2,1,4) convolutional code having a rate of $1/2$.

At $t = 0$, bits 01 are received at the input of the decoder. The decoder always starts decoding operation at 000 state and received bits are injected into the decoder one at a time [16]. Thus, there are two possible paths available (for value of input bit = 0 and 1) as illustrated in Fig. 4.5 [15]. The decoder computes the branch metrics of these two paths and continues along these paths simultaneously [8]. The path metrics for the two branches are equal to 1, which means that one bit from each output matches with one bit from the incoming bits [6].

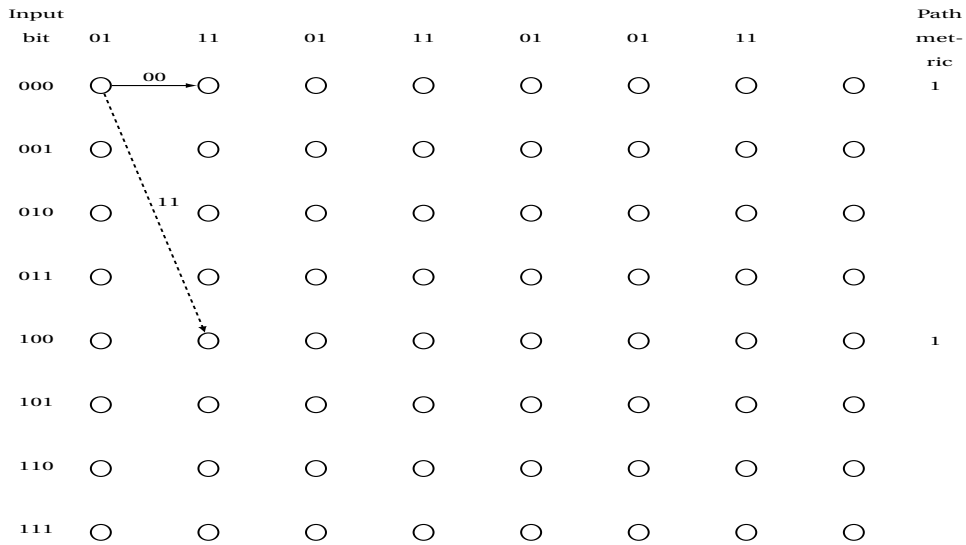


FIGURE 4.5: Viterbi decoding - step 1 [15]

At $t = 1$, the incoming bits at the input are 11. The decoding operation expands from two possible states to four possible states as shown in Fig. 4.6 [15]. The branch metrics are computed by looking at the concord between the incoming bits and the output bits. The branch metric at the new state is calculated from the previous states leading to the new state [128].

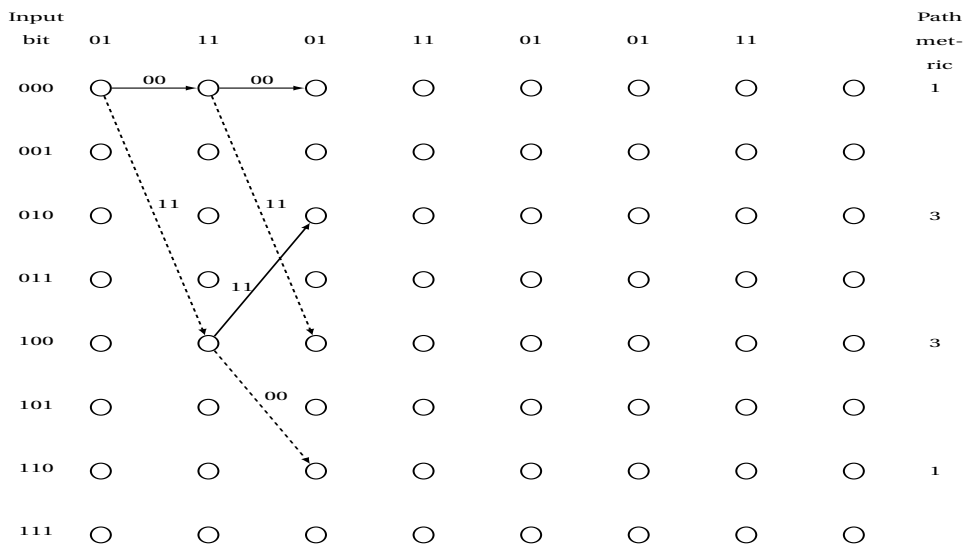


FIGURE 4.6: Viterbi decoding - step 2 [15]

At $t = 2$, the states grow from four to eight in order to show all the possible paths. The path metrics for incoming bits 01 are calculated and added to the path metrics of the

previous states at $t = 1$ [6]. It can be seen from Fig. 4.7 that the trellis is fully populated resulting in each node having at least one path coming into it [130].

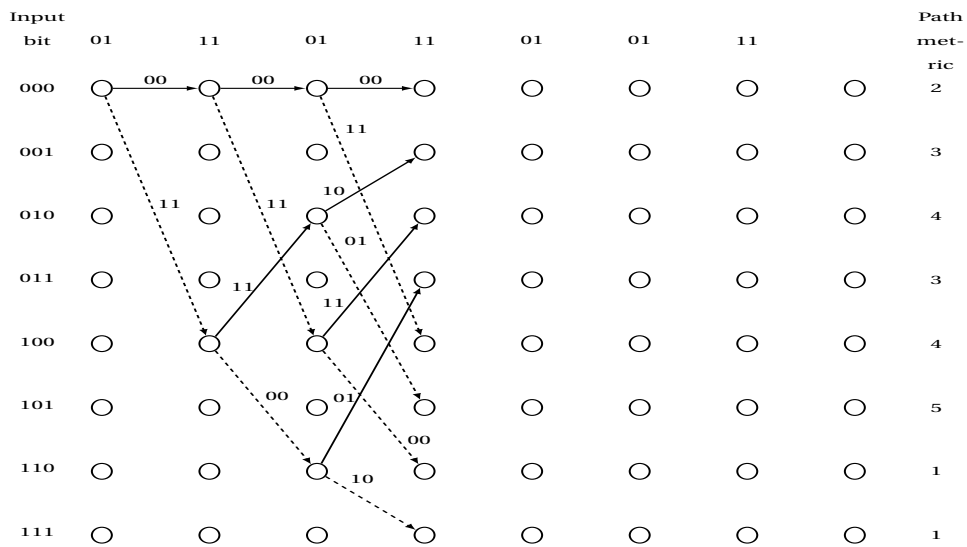


FIGURE 4.7: Viterbi decoding - step 3 [15]

At $t = 3$, the paths start converging at the nodes and there are two metrics for each path arriving at a node [6]. According to the ML principle, the path with the lower metric is discarded as it is considered the least likely path [15]. The efficiency of the Viterbi algorithm lies in its ability to discard the least likely path at each node thereby reducing the number of paths to be processed by the algorithm [129].

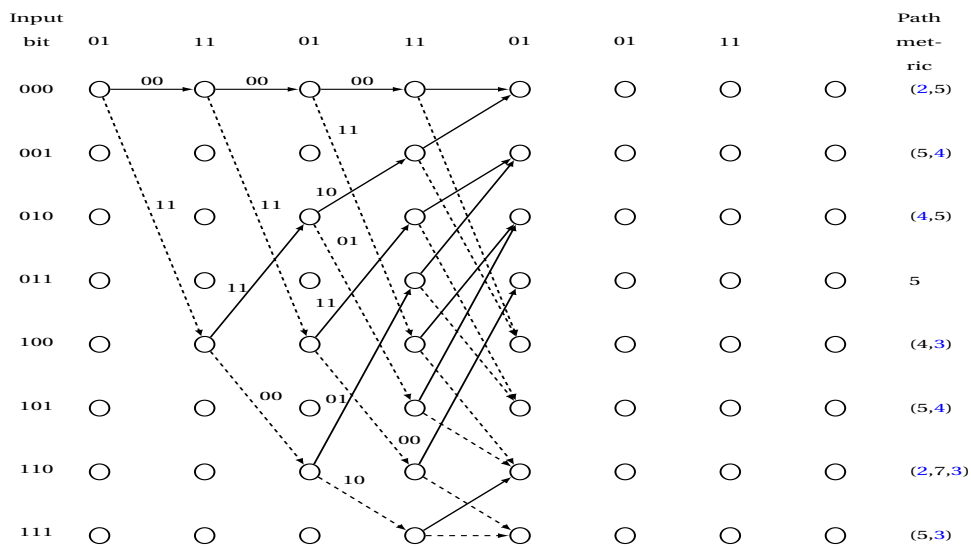


FIGURE 4.8: Viterbi decoding - step 4 [15]

To proceed with the decoding process, all the paths with lower metrics at each node have to be eliminated and only the path with the highest metric should be retained [16]. After discarding the paths with lower metrics, the surviving paths are shown in Fig. 4.9.

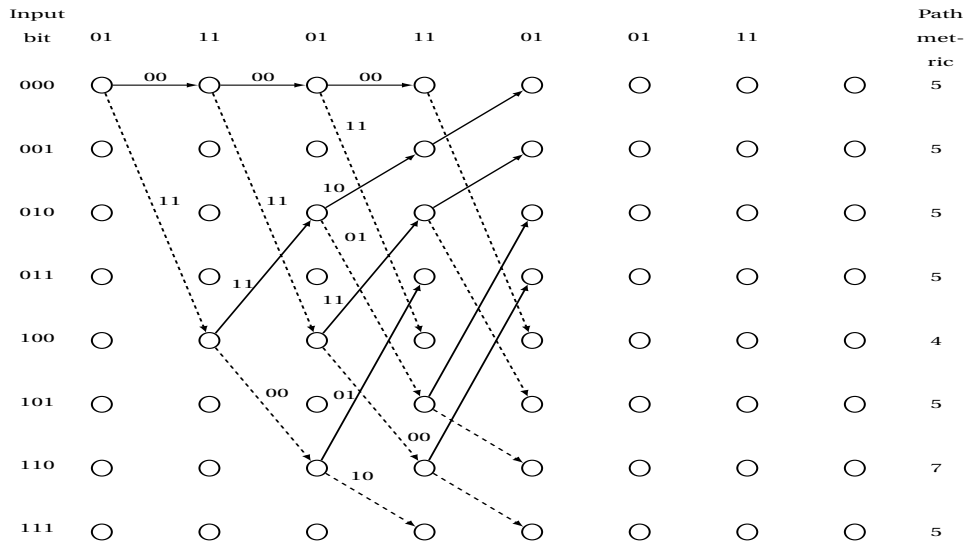


FIGURE 4.9: Viterbi decoding - step 4, after discarding [15]

At $t = 4$, the algorithm moves to the new node after discarding the paths with the lower metrics at the previous node [6]. The new metrics are computed for the converging paths at the new node and paths with the lower metrics are discarded as usual but paths with the same metrics at the same state are retained [15] as shown in Fig. 4.10.

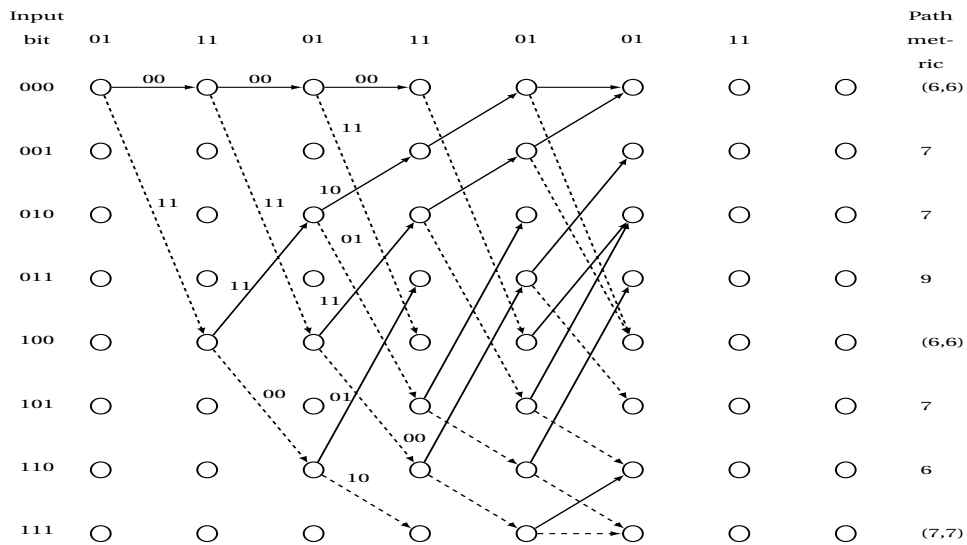


FIGURE 4.10: Viterbi decoding - step 5, after discarding [15]

At $t = 5$, proceed forward and compute the metrics at the next node after discarding paths with lower metrics at the previous node and again paths with same metrics are retained [6] as depicted in Fig. 4.11.

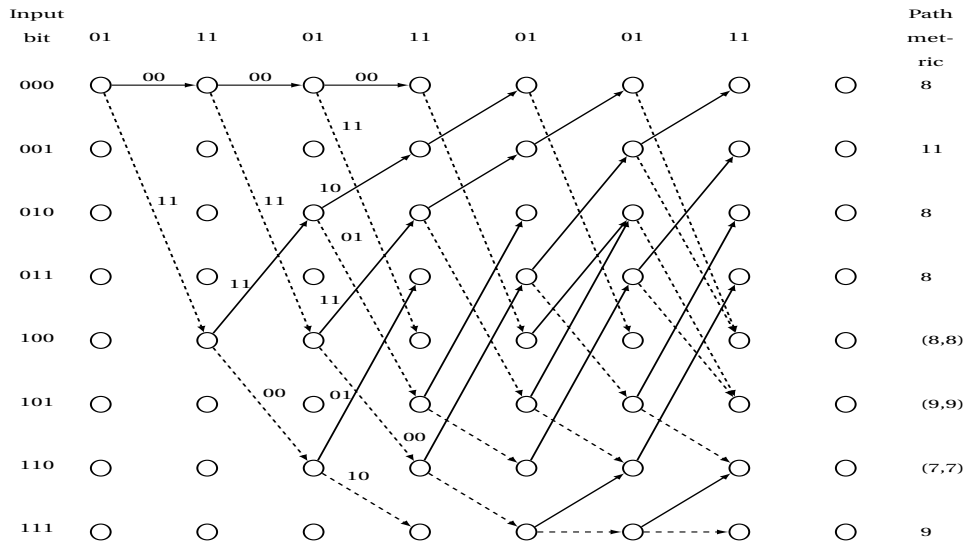


FIGURE 4.11: Viterbi decoding - step 6, after discarding [15]

At $t = 6$, bits 11 are received and again the metrics are computed for all paths at the new node. As done previously, all the paths with smaller metrics are eliminated and path with highest metric is retained [6]. If two paths have equal metrics, both paths are retained as shown in Fig. 4.12 [15].

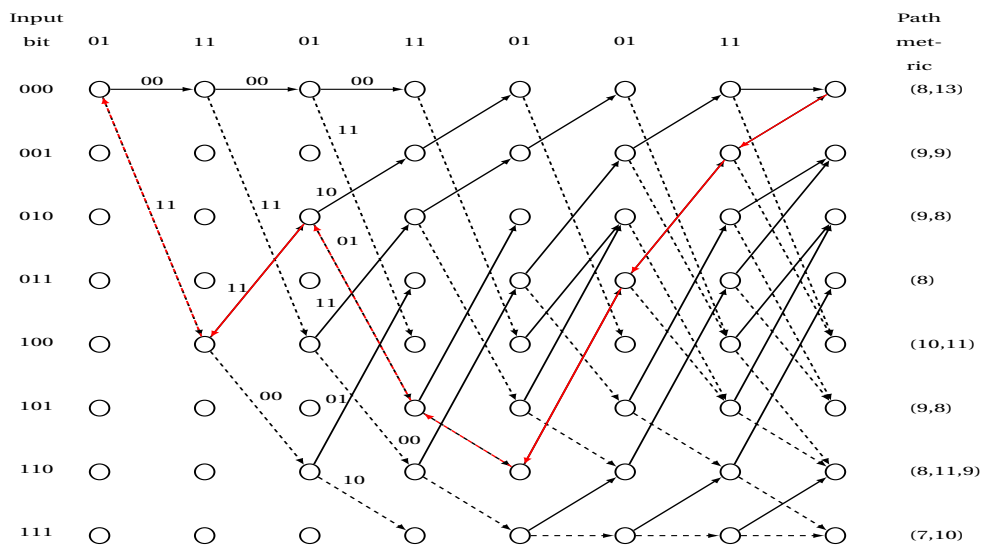


FIGURE 4.12: Viterbi decoding - step 7 [15]

The navigation through the trellis is completed after the seventh step. The next step is to determine the path with the highest metric using the traceback technique as shown in Fig. 4.12 [15]. The traceback path is indicated with the red line with the states going backward given by 000 - 001 - 011 - 110 - 101 - 010 - 100 - 000 and the corresponding decoded sequence is given as 1011000 [131]. This type of trellis decoding is also used for Trellis Coded Modulation (TCM) [132].

4.5 Soft Decision Decoding of Convolutional Code

The bits (0, 1) that are received at the receiver are represented using signal spectrum. However, when the bits are corrupted by noise, the spectrum used to represent the bits makes decoding decision complicated [21]. This is because the signal spreads out and the energy from one signal flows into the other [133].

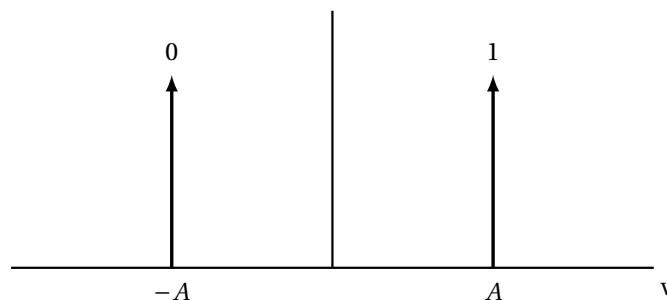


FIGURE 4.13: Signal representation of bits 0 and 1 [16]

If the noise corrupting the signal is small, i.e. noise variance is small (since noise power = noise variance), then the spread is small and vice versa as shown in Fig. 4.14 [6]. It can be easily deduced from the diagrams that if the S/N is high or the noise variance is small, then it is less likely to encounter decoding errors [21]. Carrying out a HDD involves setting a decision threshold between the two signals such that if the received voltage is positive then the signal is decoded as bit 1 and if otherwise, it is decoded as bit 0 as shown in Fig. 4.13 [6]. This process is what is regarded as Maximum likelihood (ML) decoding.

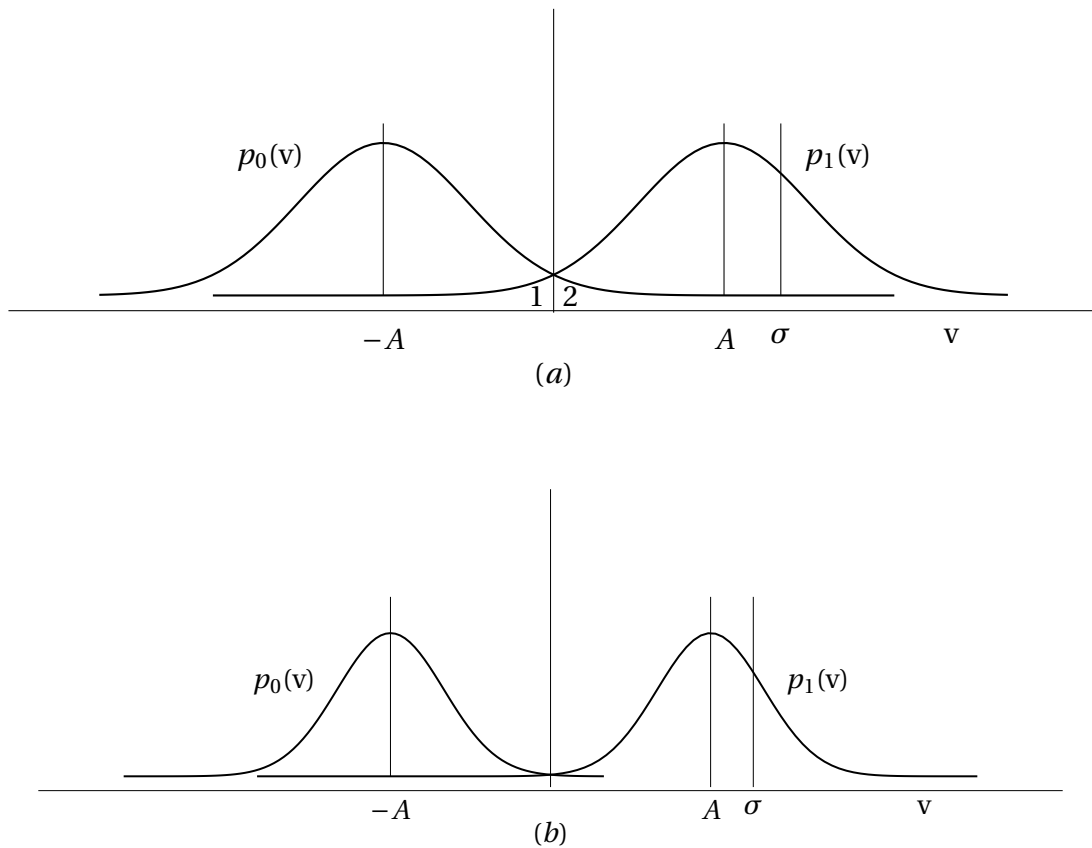


FIGURE 4.14: (a) Noise of $S/N = 2$ and (b) Noise of $S/N = 4$ spread out to spill energy from one decision region to another [6]

To perform SDD, subdivide the decision space into regions greater than two [134]. SDD improves the sensitivity of the decoding metrics and significantly improves the performance of the decoder when compared to HDD [16]. The errors that are associated with the decoding decision can be quantified and the probability that a 0 will be decoded given that a 1 was transmitted is a function of the two areas (indicated by 1 and 2) as shown in Fig. 4.14 [6]. The energy associated with bit 1 that has landed in the opposite decision region is indicated by area 1 [15]. And this results in erroneous decoding of the bit as 0. The area 2 represents the energy associated with bit 0 that has landed in the region of interest. This is subtracted from the received voltage resulting in a decoding decision error [128]. Now given that 1 was sent, the probability that it will be decoded as a 0 is given by [6]

$$P_{e1} = \frac{1}{2} \operatorname{erfc} \frac{A - v_t}{\sqrt{2}\sigma} \quad (4.1)$$

where v_t is the decision threshold voltage and σ is the noise variance or noise power. Thus, (4.1) can be rewritten as a function of signal-to-noise ratio (S/N) as [16]

$$P_{e1} = \frac{1}{2} \operatorname{erfc} \left(\sqrt{\frac{S}{N}} \right) \quad (4.2)$$

This is a familiar error rate equation that assumes that HDD has been used [135]. Now, let us divide the decision making area into four regions, instead of two, as shown in Fig. 4.15 and the probability of making a correct decoding decision is calculated from the area under the Gaussian curve [136].

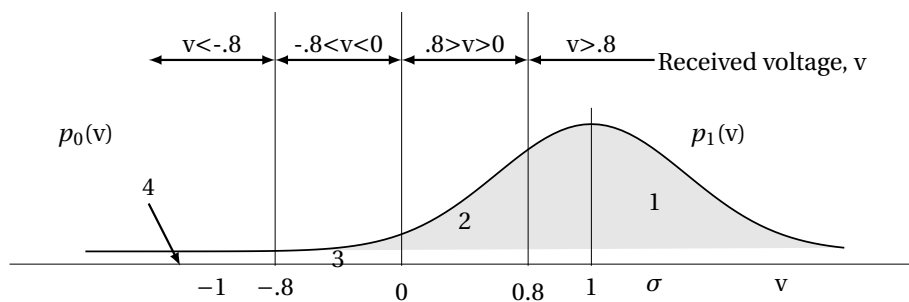


FIGURE 4.15: Creating four regions for decoding decision [6]

Let us select four regions from the above diagram as follows [6]:

- Region 1 = received voltage is greater than 0.8 v
- Region 2 = received voltage is greater than 0 but less than 0.8 v
- Region 3 = received voltage is greater than -0.8 v but less than 0
- Region 4 = received voltage is less than -0.8 v

Now assuming that the received voltage falls in region 3, the dilemma is what is the probability of error that a 1 was sent? For HDD, this probability can easily be computed using (4.2) but for multi-region space, calculate similar probabilities [131]. To accomplish this task, make use of the Q-function that provides the area under the tail defined by the distance from the mean to any other values. Thus, $Q(2)$ for a signal having a mean of 2 would yield a probability of a value that is equal to 4 or greater [17].

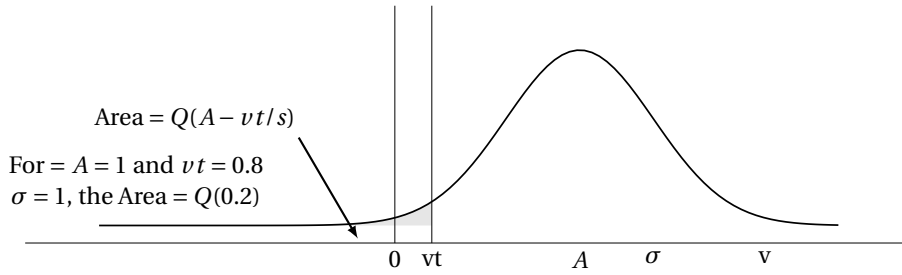


FIGURE 4.16: Q-function for determining the probabilities of a normally distributed variable [17]

The equations for the probabilities associated with the four regions can be deduced as follows [6]:

- The probability that the received voltage is in region 1 provided that a 1 was sent is $P_{e1} = 1 - Q(A - v_t/\sigma)$
- The probability that the received voltage is in region 4 provided that a 1 was sent is $P_{e4} = Q(2(A + v_t)/\sigma)$
- The probability that the received voltage is in region 2 provided that a 1 was sent is $P_{e2} = 1 - P_{e1} - Q(A/\sigma)$
- The probability that the received voltage is in region 3 provided that a 1 was sent is $P_{e3} = 1 - P_{e1} - P_{e2} - P_{e4}$

The above probabilities have been computed for $S/N = 1$ with the assumptions that $v_t = 0.8A$ and $A = 1$ [6]. It has been further assumed that both bits (0 and 1) are equiprobable. This is regarded as a priori probabilities for the bits 0 and 1 and they are always assumed to be equal except in Radar applications [17]. This process of subdividing the decision space into multiple regions greater than two is regarded as SDD. These probabilities that are described above are called transition probabilities [133]. Each received bit that requires a decoding decision has four different values of voltage associated with it. The soft decision metrics can now be computed by making use of the probabilities above [6], as shown in Fig. 4.5.

TABLE 4.2: Computation of soft decision metric [6]

Sent	ν_4	ν_3	ν_2	ν_1
1	0.03	0.12	0.25	0.60
0	0.6	0.25	0.12	0.03

Now taking the natural log of each value in Table. 4.2 and normalizing them so that one of the values becomes 0, results in the values in Table. 4.3 after some number manipulations [21].

TABLE 4.3: Normalized soft decision metric [21]

Sent	ν_4	ν_3	ν_2	ν_1
1	-3	-1	-4	-10
0	-10	-4	-1	0

Now, multiply possible allowed codewords with the received bits (corresponding voltages). During the decoding process, the decoder looks for the metric of that voltage in its memory and then carries out the necessary calculations [136]. Assume voltage pair (ν_3, ν_2) are received, and the allowed codewords are 01 and 10.

$$\text{Metric for 01} = p(0|\nu_3) + p(1|\nu_2) = -4 + -4 = -8$$

$$\text{Metric for 10} = p(1|\nu_3) + p(0|\nu_2) = -1 + -1 = -2$$

Looking at the metric calculations above, it can be observed that 01 has more likelihood than 10 and when these metrics add, they exaggerate the difference and aid decoding results [135].

The decoding performance of the algorithm can be improved by applying log likelihood metric that takes into account the channel error probability and it is expressed as [6]

$$\text{Metric for agreement} = \frac{\log_{10} 2(1-p)}{\log_{10} 2} \quad (4.3)$$

and

$$\text{Metric for disagreement} = \frac{\log_{10} 2p}{\log_{10} 2} \quad (4.4)$$

For $p = 0.1$, metric for agreement is -20 and disagreement is -1 . Thus, if 01 were received and allowed codeword is 00, then the total metric would be $-20 + -1 = -21$ and the metric for complete agreement would be -40 [133].

In summary, SDD also makes use of the Viterbi algorithm to decode a received sequence. However, the demodulator does not assign a 0 or 1 to each received bit as in HDD, rather it makes use of multi-bit quantized values [15]. Therefore, instead of using Hamming distance to calculate the branch metrics it uses squared Euclidean distance. Consequently, this makes the performance of SDD much better compared to its HDD counterpart [21]. The computational complexity of the Viterbi decoder increases exponentially as a function of the constraint length (K) and as such it is limited to $K = 9$ in practice [137].

4.6 Hard Decision Decoding of Reed-Solomon Code

Reed-Solomon (RS) codes are used in many data storage and digital communication systems and as such, efficient encoding and decoding are paramount for improved system performance [18]. RS codes are capable of correcting all errors within the error capability of the code. Reed-Solomon codes are used in many applications because of their high capability of correcting both random and burst errors; and the existence of efficient decoding algorithms such as the Berlekamp-Massey (BM) algorithm used to decode Reed-Solomon codes [138]. RS codes that are used in storage devices are decoded using an algebraic method known as hard decision decoding (HDD) [139]. A $t = (n - k)/2$ error-correcting RS code in $GF(2^m)$ has the following properties [140]:

- Block length = $n = 2^m - 1$
- Number of parity-check = $n - k = 2t$
- Minimum distance = $d_{min} = 2t + 1$

The RS decoder in its decoding operation carries out two tasks: detecting errors in the received codeword and correcting the detected errors [140]. The error-correcting capability is entirely dependent on the RS code used. The RS decoder consists mainly of three parts: syndrome decoder for computing syndrome components, Berlekamp-Massey algorithm for solving the key equation and the Chien search for error correction [125]. The general steps that are involved in decoding Reed-Solomon codes are summarized as follows [140]:

- Computation of syndrome vector $(S_1, S_2, \dots, S_{2t})$ whose $2t$ components belong to $GF(2^m)$.
- Determine error-location polynomial $\sigma(X)$ of degree t or less over $GF(2^m)$ from the syndromes using the Berlekamp-Massey algorithm.
- Determine the error-locations from step 2.
- Calculate error values using the Chien search and perform error correction using Forney algorithm.

These steps are illustrated in Fig. 4.17.

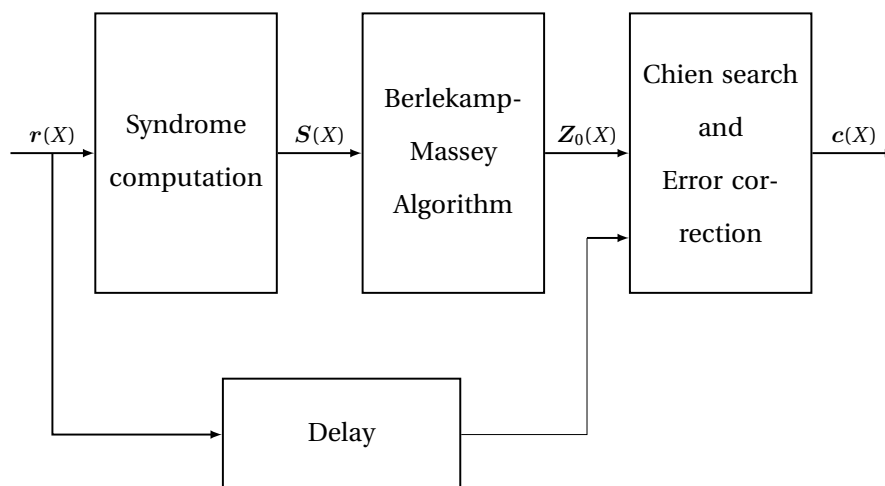


FIGURE 4.17: Reed-Solomon Decoder [18]

4.6.1 Syndrome Computation

Syndromes are indicators of whether errors are present in the received codeword or not. Thus, if the value of the syndrome computation is zero, it indicates that the received codeword contains no errors and a non-zero value indicates the presence of errors in the received message [141]. If the transmitted codeword is invalid, syndrome calculation will only produce components up to t errors but if a valid codeword is generated, syndrome computation will produce a syndrome polynomial up to $2t$ errors with all zero coefficients [142]. Let α in $GF(2^m)$ be a primitive polynomial of t error-correcting RS code of length $2^m - 1$. Then the generator polynomial $G(X)$ is the polynomial of degree $n - k$ whose coefficients are from $GF(2^m)$ and has $\alpha, \alpha^2, \dots, \alpha^{2t}$ as its roots [140]. Let $k(X)$ be the message polynomial, then the encoded codeword can be represented in a systematic form as [18]

$$c(X) = k(X)X^{n-k} + \text{Mod} \left[k(X)X^{n-k} / G(X) \right] \quad (4.5)$$

where $\text{Mod} \left[k(X)X^{n-k} / G(X) \right]$ is the remainder polynomial obtained by dividing $k(X)$ by $G(X)$. The received polynomial is given by [140]

$$\begin{aligned} r(X) &= c(X) + e(X) \\ &= r_0 + r_1X + r_2X^2 + \dots + r_{n-k}X^{n-1} \end{aligned} \quad (4.6)$$

where $e(X) = e_0 + e_1X + e_2X^2 + \dots + e_{n-k}X^{n-1}$ is the error pattern introduced by the channel noise. The coefficients of $c(X)$, $e(X)$ and $r(X)$ are all elements in $GF(2^m)$. The syndrome components of the received polynomial can be computed as follows [143]:

$$\begin{aligned} S_i^0 &= r(\alpha^i) = e(\alpha^i) \\ &= \sum_{j=1}^t Y_j X_j^i \quad i = 1, 2, \dots, 2t \end{aligned} \quad (4.7)$$

where X_j represents the error location of the j th erroneous symbol and Y_j is the corresponding error value. Therefore, to decode a particular RS code with given syndrome

values, the error locator polynomials and the corresponding error values have to be determined [125].

4.6.2 Berlekamp-Massey Algorithm

The Berlekamp-Massey algorithm is an iterative algorithm that is used to find the error-location polynomial $\sigma(X)$ [140]. Berlekamp published his algorithm in 1968 and shortly after that, Massey also published his variation of the algorithm in 1969 [144]. The algorithm is considered to be a fast way of inverting matrices that have constant diagonals and it works over any field, but is mostly used in finite fields that occur more frequently in coding theory [126].

The application and implementation of the algorithm were further advanced by Massey through the use of physical interpretation of a linear feedback shift register (LFSR) as a tool to provide better understanding of the algorithm. The LFSR is used in encoding and decoding of a sequence using a simple linear formula [140]. The use of physical interpretation in the algorithm helps to provide a physical explanation of the length of the encoded information which is a valuable insight needed by the decoder. He defined the length of the information as twice the length of the LFSR [145].

The main task of the RS decoder is to solve the key equation $Z_0(X)$ that has $2t$ linearly dependent equations [18].

$$\sigma(X)S(X) = Z_0(X) \bmod(X^{2t}) \quad (4.8)$$

where $\sigma(X)$ is the error-location polynomial that contains information about the locations of corrupted symbols and $Z_0(X)$ is the error-value evaluator polynomial that has information regarding the magnitude of the corrupted symbols [18]. There are numerous algorithms that can be used to solve for the key equation, but the BM algorithm has been chosen in this research because of its less decoding complexity. To find the error-value locator polynomial $Z_0(X)$, first determine the error-locator polynomial $\sigma(X)$ [139]. Suppose that the error pattern $e(X)$ presented in (4.6) contains ν errors

(nonzero components) at locations $X^{j_1}, X^{j_2}, \dots, X^{j_\nu}$ with $0 \leq j_1 < j_2 < \dots < j_\nu \leq n-1$. Then $e(X)$ can be rewritten as [138]

$$e(X) = e_{j_1} X^{j_1} + e_{j_2} X^{j_2} + \dots + e_{j_\nu} X^{j_\nu} \quad (4.9)$$

where $e_{j_1}, e_{j_2}, \dots, e_{j_\nu}$ are the error values. Therefore, to determine $e(X)$, first determine the error locations X^{j_i} and error values e_{j_i} . To determine the error-location polynomial, first compute the syndrome given by (4.7) [140]

$$S_i = \mathbf{v}(\alpha^i) + e(\alpha^i) = e(\alpha^i) \quad (4.10)$$

From (4.9) and (4.10), formulate a set of equations that relates the error locations and error values to the syndrome of the received polynomial $\mathbf{r}(X)$ as follows [140]:

$$\begin{aligned} S_1 &= e_{j_1} \alpha^{j_1} + e_{j_2} \alpha^{j_2} + \dots + e_{j_\nu} \alpha^{j_\nu} \\ S_2 &= e_{j_1} \alpha^{2j_1} + e_{j_2} \alpha^{2j_2} + \dots + e_{j_\nu} \alpha^{2j_\nu} \\ &\vdots \\ S_{2t} &= e_{j_1} \alpha^{2tj_1} + e_{j_2} \alpha^{2tj_2} + \dots + e_{j_\nu} \alpha^{2tj_\nu} \end{aligned} \quad (4.11)$$

For $1 \leq i \leq \nu$, let $\beta_i \triangleq \alpha^{j_i}$ and $\delta_i \triangleq e_{j_i}$ be the error-location numbers and error values respectively. Thus, (4.11) can be expressed as [140]

$$\begin{aligned} S_1 &= \delta_1 \beta_1 + \delta_2 \beta_2 + \dots + \delta_\nu \beta_\nu \\ S_2 &= \delta_1 \beta_1^2 + \delta_2 \beta_2^2 + \dots + \delta_\nu \beta_\nu^2 \\ &\vdots \\ S_{2t} &= \delta_1 \beta_1^{2t} + \delta_2 \beta_2^{2t} + \dots + \delta_\nu \beta_\nu^{2t} \end{aligned} \quad (4.12)$$

The error-location polynomial is expressed as [146]

$$\begin{aligned} \sigma(X) &= (1 - \beta_1 X)(1 - \beta_2 X) \cdots (1 - \beta_\nu X) \\ &= \sigma_0 + \sigma_1 X + \sigma_2 X^2 + \dots + \sigma_\nu X^\nu \end{aligned} \quad (4.13)$$

where $\sigma_0 = 1$. The error-location numbers are defined as the reciprocals of the $\sigma(X)$.

A set of equations called generalized Newton's identities that provides relationship between the coefficients σ'_i 's of $\sigma(X)$ and the syndrome components S'_i 's can be developed from (4.12) and (4.13) as follows [140]:

$$\begin{aligned}
 S_{\nu+1} + \sigma_1 S_{\nu} + \sigma_2 S_{\nu-1} + \cdots + \sigma_{\nu} S_1 &= 0 \\
 S_{\nu+2} + \sigma_1 S_{\nu+1} + \sigma_2 S_{\nu} + \cdots + \sigma_{\nu} S_2 &= 0 \\
 &\vdots \\
 S_{2t} + \sigma_1 S_{2t-1} + \sigma_2 S_{2t-2} + \cdots + \sigma_{\nu} S_{2t-\nu} &= 0
 \end{aligned} \tag{4.14}$$

The goal of the decoding algorithm is to find a minimum-degree polynomial $\sigma(X)$ whose coefficients satisfy the generalized Newton's identities and then, determine the error locations and error values [140]. The error-location polynomial $\sigma(X)$ is found in $2t$ iterative steps using BM's algorithm as shown in Table 4.4.

TABLE 4.4: BM's iterative procedure for finding $\sigma(X)$ [22]

i	$q_i - p_i$	d_i	z_i
-1		-1	
0		0	-1
1			
.			
.			
.			
$2t$			

The first step is to fill $-1 \leq i \leq 0$ using expressions below [22].

$$\begin{aligned}
 q_{-1}(x) &= 1 + s_{m+1}x + s_{m+2}x^2 + \cdots + s_{m+2t}x^{2t} \\
 q_0(x) &= s_{m+1} + s_{m+2}x + \cdots + s_{m+2t}x^{2t-1} \\
 p_{-1}(x) &= x^{2t+1} \\
 p_0(x) &= x^{2t}
 \end{aligned} \tag{4.15}$$

$d_{-1} = -1, d_0 = 0$ and $z_0 = -1$

The second step is to fill blank spaces for $1 \leq i \leq 2t$ by first checking if $q_{i-1,0} = 0$. If this condition is met, then fill the next available space using the following expressions [22]

$$\begin{aligned} q_i(x) &= q_{i-1}(x)/x \\ p_i(x) &= p_{i-1}(x)/x \\ d_i &= d_{i-1} + 1 \\ z_i &= z_{i-1} \end{aligned} \tag{4.16}$$

But if $q_{i-1,0} \neq 0$, then fill the next available space using the following expressions [22].

$$\begin{aligned} q_i(x) &= (q_{i-1}(x) + (q_{i-1,0}/q_{z_{i-1,0}})q_{z_{i-1}}(x))/x \\ p_i(x) &= (p_{i-1}(x) + (q_{i-1,0}/q_{z_{i-1,0}})p_{z_{i-1}}(x))/x \\ d_i &= 1 + \min\{d_{i-1}, d_{z_{i-1}}\} \\ z_i &= \begin{cases} i-1, & \text{if } d_i - 1 \geq d_{z_{i-1}} \\ z_{i-1}, & \text{otherwise} \end{cases} \end{aligned} \tag{4.17}$$

At $2t$ iteration, a true error-location polynomial is obtained provided that the number of errors in the error pattern does not exceed the error-correcting capability of the code (i.e., $v \leq t$) [22]. After obtaining the error-location polynomial, find the error-locations by first obtaining the roots of $\sigma(X)$ and secondly, taking the inverse of these roots to obtain the error-location numbers that indicate the positions where errors have occurred in the received polynomial $r(X)$ [140].

4.6.3 Chien search Algorithm and Error Correction

The next step in the decoding procedure is to determine the error values by finding the error-value evaluator using the Chien search algorithm and performing error correction using the Forney algorithm when Chien sum is equal to zero [18]. Chien search is used to obtain the roots of the error-location polynomial by using all the possible input values and checks to see if the corresponding outputs are zeros [138]. The delay block in

the RS decoder is used for the adjustment of delays in the syndrome block and startup delay in the Chien search block [126]. The syndrome polynomial $S(X)$ is defined as [140]

$$\begin{aligned} S(X) &\triangleq S_1 + S_2X + \cdots + S_{2t}X^{2t-1} + S_{2t+1}X^{2t} + \cdots \\ &= \sum_{j=1}^{\infty} S_j X^{j-1} \end{aligned} \quad (4.18)$$

where only the first $2t$ coefficients are known. For $1 \leq j < \infty$,

$$S_j = \sum_{l=1}^v \delta_l \beta_l^j \quad (4.19)$$

By combining (4.18) and (4.19), $S(X)$ can be rewritten as

$$\begin{aligned} S(X) &= \sum_{j=1}^{\infty} X^{j-1} \sum_{l=1}^v \delta_l \beta_l^j \\ &= \sum_{l=1}^v \delta_l \beta_l^j \sum_{j=1}^{\infty} (\beta_l X)^{j-1} \end{aligned} \quad (4.20)$$

where

$$\frac{1}{(1 - \beta_l X)} = \sum_{j=1}^{\infty} (\beta_l X)^{j-1} \quad (4.21)$$

And from (4.20) and (4.21), $S(X)$ can be simplified as [140]

$$S(X) = \sum_{l=1}^v \frac{\delta_l \beta_l}{(1 - \beta_l X)} \quad (4.22)$$

Now multiplying $\sigma(X)S(X)$ results in [140]

$$\begin{aligned} \sigma(X)S(X) &= (1 + \sigma_1 X + \cdots + \sigma_v X^v) \cdot (S_1 + S_2 X + S_3 X^2 + \cdots) \\ &= S_1 + (S_2 + \sigma_1 S_1)X + (S_3 + \sigma_1 S_2 + \sigma_2 S_1)X^2 + \cdots + \\ &\quad (S_{2t} + \sigma_1 S_{2t-1} + \cdots + \sigma_v S_{2t-v})X^{2t-1} + \cdots \end{aligned} \quad (4.23)$$

Adopting the format in (4.22), $\sigma(X)S(X)$ can be rearranged in the following form [140]:

$$\begin{aligned}\sigma(X)S(X) &= \left[\prod_{i=1}^v (1 - \beta_i X) \right] \cdot \left[\sum_{l=1}^v \frac{\delta_l \beta_l}{(1 - \beta_l X)} \right] \\ &= \sum_{l=1}^v \frac{\delta_l \beta_l}{(1 - \beta_l X)} \cdot \prod_{i=1}^v (1 - \beta_i X) \\ &= \sum_{l=1}^v \delta_l \beta_l \prod_{i=1, i \neq l}^v (1 - \beta_i X)\end{aligned}\quad (4.24)$$

a polynomial $Z_0(X)$ of degree $v - 1$ can now be defined as follows [140]:

$$Z_0(X) \triangleq \sum_{l=1}^v \delta_l \beta_l \prod_{i=1, i \neq l}^v (1 - \beta_i X) \quad (4.25)$$

From (4.23), (4.24) and (4.25), it can be observed that $Z_0(X)$ must be equal to the first v terms from X^0 to X^{v-1} in (4.23). Thus,

$$\begin{aligned}Z_0(X) &= S_1 + (S_2 + \sigma_1 S_1)X + (S_3 + \sigma_1 S_2 + \sigma_2 S_1)X^2 \\ &\quad + \cdots + (S_v + \sigma_1 S_{v-1} + \cdots + \sigma_{v-1} S_1)X^{v-1}\end{aligned}\quad (4.26)$$

Using the fact that the degree of $Z_0(X)$ is $v - 1$, it can be deduced that the coefficients of powers from X^v to X^{2t-1} in (4.23) must all equal zero. Thus, setting these coefficients equal to zero, the same set of equations as in (4.14) is obtained [140]. Finally, it can be shown that the error values can be evaluated from $Z_0(X)$ and $\sigma(X)$. Thus, start by substituting β_k^{-1} for X in (4.25) as follows [18]:

$$\begin{aligned}Z_0(\beta_k^{-1}) &= \sum_{l=1}^v \delta_l \beta_l \prod_{i=1, i \neq l}^v (1 - \beta_i \beta_k^{-1}) \\ &= \delta_k \beta_k \prod_{i=1, i \neq k}^v (1 - \beta_i \beta_k^{-1})\end{aligned}\quad (4.27)$$

Now taking the derivatives of $\sigma(X)$ in (4.13) results in

$$\begin{aligned}\sigma'(X) &= \frac{d}{dX} \prod_{i=1}^v (1 - \beta_i X) \\ &= \sum_{l=1}^v \beta_l \prod_{i=1, i \neq l}^v (1 - \beta_i X)\end{aligned}\quad (4.28)$$

And

$$\sigma'(\beta_k^{-1}) = -\beta_k \prod_{i=1, i \neq l}^v (1 - \beta_i \beta_k^{-1}) \quad (4.29)$$

From (4.27) and (4.29), it can be observed that error value δ_k at position β_k is given by [18]

$$\delta_k = \frac{-Z_0(\beta_k^{-1})}{\sigma'(\beta_k^{-1})} \quad (4.30)$$

The expression $Z_0(X)$ is regarded as the error-value evaluator.

In summary, RS codes are used to effectively correct burst errors that occur due to impulsive noise. Reed-Solomon codes are considered to be effectively optimal binary burst-error-correcting codes [4]. Convolutional codes on the other hand, are a group of probabilistic coding that is more concerned with finding the classes of codes that optimize the average performance as a function of coding and decoding complexities. Convolutional codes are mostly used to correct random errors and are usually decoded using the Viterbi decoding algorithm [62]. The combination of Reed-Solomon encoding and convolutional encoding in error correction provides a combined error correction scheme that is capable of combating both burst and random errors. However, some research have shown that even the combination of Reed-Solomon encoding and interleaving may not sufficiently combat all the burst errors that occur in a PLC channel [9]. This is because the performance of the Reed-Solomon decoder (RCD) can drastically degrade even when in conjunction with a powerful symbol interleaver in the presence of impulsive interference [72]. This occurs due to the fact that while the symbol interleaver converts burst errors into random errors, the number of residual burst errors at the output of the interleaver may exceed the error correcting capability of the Reed-Solomon code being used [75].

4.7 Erasure Decoding of Reed-Solomon Code

In an erasure channel, erasures occur at the receiver when the bits transmitted are either received correctly or not received; that is, the bits get scrambled in such a way that the receiver has no idea of what was transmitted [147]. In an erasure channel such

as the internet, transmission delays are encountered due to possible retransmission of erased or lost bits, but these delays can be eliminated through the use of forward error correction [148]. Erasures occur due to channel distortion and in some cases, the bit transmitted can get deleted or erased. In an attempt to recover what was transmitted, erasure decoding is performed at the receiver.

An RS code over $GF(2^m)$ can be effectively used to correct all combinations of v errors and u erasures provided that the condition $v + u/2 \leq t$ is maintained [140]. The conventional Berlekamp-Massey algorithm adopted in the HDD of RS codes can be modified to correct both errors and erasures effectively [149]. The conventional step-by-step decoding algorithm first proposed by Massey for decoding RS codes can directly determine whether the received symbol contains errors or not. It then finds the corresponding error value without having to find the error-location polynomial [145]. This conventional decoding algorithm is required to perform $2^m - 1$ iterations on each received symbol in order to determine whether every nonzero received symbol is in error or not [149]. The procedure for step-by-step error or erasure correction is described in [150]. Suppose that the received codeword given by [140]:

$$\mathbf{r}(X) = r_0 + r_1X + r_2X^2 + \cdots + r_{n-1}X^{n-1} \quad (4.31)$$

contains v errors and u erasures introduced by the channel noise and that v errors and u erasures are embedded in the positions $X^{i_1}, X^{i_2}, \dots, X^{i_v}$ and $X^{j_1}, X^{j_2}, \dots, X^{j_u}$ respectively. Thus, the received codeword $\mathbf{r}(X)$ can be modified to represent the sum of transmitted codeword $\mathbf{c}(X)$, the error pattern $\mathbf{e}(X)$ and the erasure pattern $\mathbf{f}(X)$ [140]. where

$$\begin{aligned} \mathbf{e}(X) &= e_0 + e_1X + e_2X^2 + \cdots + e_{n-1}X^{n-1} \\ &= \sum_{i=1}^v e_{i_1} X^{i_1} \quad e_{i_1} \neq 0, l = 1, 2, \dots, v \end{aligned} \quad (4.32)$$

and

$$\begin{aligned} \mathbf{e}(X) &= f_0 + f_1X + f_2X^2 + \cdots + f_{n-1}X^{n-1} \\ &= \sum_{i=1}^u f_{j_1} X^{j_1} \quad f_{j_1} \neq 0, l = 1, 2, \dots, u \end{aligned} \quad (4.33)$$

The erasure positions are known to the receiver but not the magnitudes of these erasures, therefore, the decoding operation is aimed at finding the locations of the errors and the magnitudes of both errors and erasures [150]. Now, using the information from the erasure locations, replace the erased positions in the received codeword $r(X)$ with zeros bearing in mind that substitution with zeros can lead to introduction of additional e errors and compute the syndrome values as follows [150]:

$$\begin{aligned}
 S_i(X) &= r(\alpha^i) \\
 &= \sum_{i=1}^v e_{i_1} (\alpha^{i_1})^i + \sum_{l=1}^u f_{j_1} (\alpha^{j_1})^j \\
 &= \sum_{i=1}^v e_{i_1} (X^{i_1})^i + \sum_{l=1}^u f_{j_1} (Y^{j_1})^l \quad 1 \leq i \leq 2t
 \end{aligned} \tag{4.34}$$

Forney in [151] introduced a linear transformation on the syndromes taking into account the information derived from the known erasure locations. This transformation represented by $\hat{S}(X) = \Gamma(X) \cdot S(X) \bmod X^{2t+1}$, is called the modified syndrome polynomial and erasure-location polynomial $\Gamma(X)$ is given by [151]

$$\begin{aligned}
 \Gamma(X) &= \Gamma_0 + \Gamma_1 X + \Gamma_2 X^2 + \dots + \Gamma_u X^u \\
 &= \prod_{i=1}^u (1 + Y_i X) = \prod_{i=1}^u (1 + \alpha^{j_i} X)
 \end{aligned} \tag{4.35}$$

and the syndrome polynomial $S(X)$ is given by [151]

$$S(X) = S_1 + S_2 X + S_3 X^2 + \dots + S_{2t} X^{2t-1} \tag{4.36}$$

Therefore, the original $2t$ syndrome values can be transformed into $2t - u$ modified error-syndromes as given by [150]

$$\begin{aligned}
\mathbf{T}_i &= \hat{\mathbf{S}}_{i+u} \\
&= \sum_{k=0}^u \mathbf{\Gamma}_k \mathbf{S}_{i+u-k} \\
&= \sum_{k=0}^u \mathbf{\Gamma}_k \left[\sum_{i=1}^v e_{i_1} X_i^{i+u-k} + \sum_{i=1}^u f_{i_1} Y_i^{i+u-k} \right] \\
&= \sum_{k=0}^u \mathbf{\Gamma}_k \left[\sum_{i=1}^v e_{i_1} X_i^{i+u-k} \right] + \sum_{k=0}^u \mathbf{\Gamma}_k \left[\sum_{j=1}^u f_{j_1} Y_j^{i+u-k} \right] \\
&= \sum_{i=1}^v e_{i_1} \cdot X_i^u \cdot \left[\sum_{k=0}^u \mathbf{\Gamma}_k X_i^{-k} \right] \cdot X_i^i + \sum_{i=1}^u f_{j_1} \cdot Y_i^u \cdot \left[\sum_{k=0}^u \mathbf{\Gamma}_k X_i^{-k} \right] \cdot Y_i^i \\
&= \sum_{i=1}^v e_{i_1} \cdot X_i^u \cdot \mathbf{\Gamma}(X_i^{-1}) \cdot X_i^1 + \sum_{i=1}^u f_{j_1} \cdot Y_i^u \cdot \mathbf{\Gamma}(Y_i^{-1}) \cdot Y_i^1 \\
&= \sum_{i=1}^v e_{i_1} \cdot X_i^u \cdot \mathbf{\Gamma}(X_i^{-1}) \cdot X_i^1 \\
&= \sum_{i=1}^v E_{i_1} \cdot X_i^1 \quad 1 \leq i \leq 2t - u
\end{aligned} \tag{4.37}$$

where $E_{i_1} = e_{i_1} \cdot X_i^u \cdot \mathbf{\Gamma}(X_i^{-1})$, $l = 1, 2, \dots, v$ are the modified error values. It can be observed from (4.37) that the modified syndrome values are similar to the original syndrome values obtained for error-only decoding [152]. This is because the transformation inserts the erasure locators into the original syndrome values to produce modified syndrome values that are dependent on the error locators [150].

The coefficients of the error-location polynomial given by [150]

$$\mathbf{\Lambda}(X) = \prod_{l=1}^v (1 + \alpha^{i_1} X) \tag{4.38}$$

are then calculated using the modified syndrome values just as in error-only decoding. The Chien algorithm is then used to find the error locators and using the information from the error locators, compute the erasure locators, error-location polynomial, erasure-location polynomial and modified syndrome polynomial [18]. Finally, use the Forney algorithm to calculate the magnitudes of both errors and erasures as follows

[140]:

$$e_{i_1} = \frac{X_i \mathbf{\Omega}(X_i^{-1})}{\mathbf{\Phi}'(X_i^{-1})} \quad (4.39)$$

$$f_{j_1} = \frac{Y_l \mathbf{\Omega}(Y_l^{-1})}{\mathbf{\Phi}'(Y_l^{-1})} \quad (4.40)$$

where the error-evaluator polynomial and error/erasure-location polynomial are represented as $\mathbf{\Omega}(X) = \mathbf{\Lambda}(X) \cdot [1 + \hat{\mathbf{S}}(X)] \bmod X^{2l+1}$ and $\mathbf{\Phi}(X) = \mathbf{\Lambda}(X) \cdot \mathbf{\Gamma}(X)$ respectively [153].

4.8 Joint Decoding Scenarios

The information received from each channel as shown in Fig. 3.1 is decoded under two scenarios. In the first scenario, the received codewords are decoded separately using each FEC decoder. In this case, each channel is decoded using its own FEC decoder resulting in four decoders at the receiver. Thus, each system is decoded according to the PLC G3 model and the joint decoding technique is not applicable. In the second scenario, joint decoding is done for both hard decision decoding (HDD) and soft decision decoding (SDD) for both convolutional and Reed-Solomon codes. Under this condition, a maximum of three decoders are used and there are three ways in which joint decoding can be applied. Firstly, the received codewords are combined and jointly decoded using the convolutional decoder (CD) and the RS decoder (RSD) is completely ignored. This technique results in the use of only one decoder for both systems. Secondly, the received codewords from both channels are combined and jointly decoded at either CD or RSD. This technique deploys two decoders in cascade to accomplish the intended task. In the third option, the received codewords are separately decoded using the convolutional decoders (one for each channel). The outputs of the two decoders are then combined and decoded using the RSD. This technique makes use of three decoders to accomplish the required task. These scenarios are further expanded and described below.

- Joint SDD is performed at CD (inner decoder). The received codewords from both channels are combined and jointly decoded at the CD. This method uses only one decoder since RSD is completely ignored.
- Joint HDD is performed at CD. The combined codeword is jointly decoded at the CD and the output of this decoder is then passed to RSD. Thus, only two decoders are used in this process.
- Joint HDD is performed at CD. The combined codeword is jointly decoded at the CD and the output of this decoder is then passed to RSD where erasure decoding (ED) is performed. Only two decoders are used in this process.
- Joint HDD is performed at RSD (outer decoder). The output of each channel is separately decoded using CD. The outputs of the two decoders are then combined and jointly decoded at RSD. A maximum of three decoders are used in this process.
- Joint HDD is performed at RSD. The output of each channel is separately decoded using CD. The outputs of the two decoders are then combined and jointly decoded at RSD by applying ED technique. A maximum of three decoders are also used in this process.

The above scenarios are applied to six different cases that are derived from the relationship between the source and the receiver. The application of these scenarios to the cases and simplified diagram illustrating these situations are presented and in Fig.4.18.

Case 1: The above scenarios are applied when the angle of orientation between the source and the receiver is zero. That is, $\theta = 0^\circ$.

Case 2: The scenarios are applied when $\theta = 10^\circ$.

Case 3: The scenarios are applied when $\theta = 15^\circ$.

Case 4: The above scenarios are also applied when the area of the receiver is 1 mm^2 . That is, $A = 1 \text{ mm}^2$.

Case 5: The scenarios are applied when $A = 0.5 \text{ mm}^2$.

Case 6: The scenarios are applied when $A = 0.1 \text{ mm}^2$.

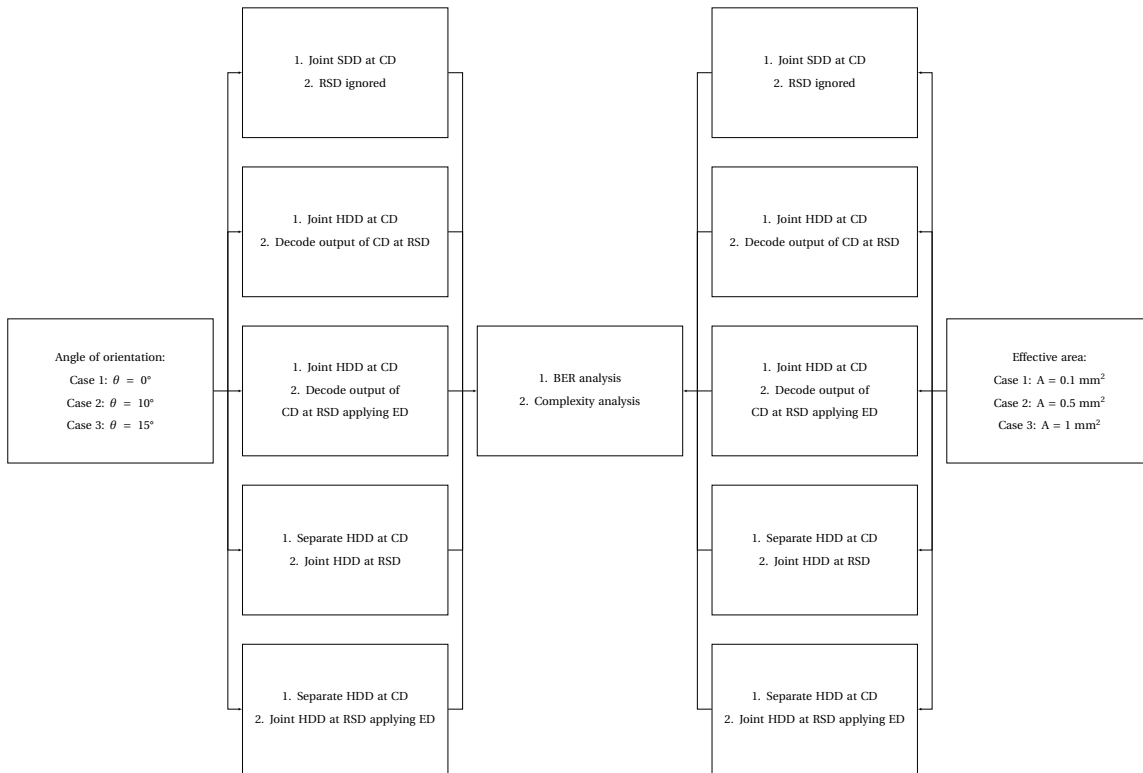


FIGURE 4.18: Application of joint decoding technique at either Reed-Solomon or convolutional decoder

After each of the three scenarios presented, the system performance is analyzed in terms of BER using MATLAB and the performance of joint decoding is then compared to that of separate decoding in terms of BER and complexity. The scenarios that are involved in the methodology are summarized in Fig. 4.18. To further enhance the performance of our systems, erasure decoding is performed on the combined received codeword. This technique takes advantage of both interleaving and erasure decoding to improve the error-correcting capability of our system. To achieve this added performance, first decode the first codewords received from both channels from which error locations are determined. Then these error locations are assumed as erasure locations in the subsequent codewords of the same interleaving block. Thus, remaining codewords are decoded in parallel [147].

4.9 Summary

There are eight sections in this chapter. Introduction that described the content of the chapter was presented in Section 4.1. In Section 4.2, the concept of decoding for benchmark scheme was introduced as shown in Fig. 4.1 and the issues that are associated with this technique were discussed. In order to overcome the issues that are encountered in the application of separate decoding, the joint decoding technique was proposed in Section 4.3. The advantages offered by this technique were described and different positions at which joint decoding can be applied in our proposed system were shown in Figs. 4.2, 4.3 and 4.4. To apply joint decoding at either convolutional or Reed-Solomon decoder, a decoding algorithm that is capable of correcting both random and burst errors is needed. Thus, the Viterbi algorithm was introduced in Sections 4.4 and 4.5 for hard decision decoding (HDD) and soft decision decoding (SDD) respectively. The operation mechanism of this algorithm was properly demonstrated and examples were used to show how both HDD and SDD are performed using the Viterbi algorithm. In Section 4.6, the decoding procedure of the Berlekamp-Massey algorithm for HDD of Reed-Solomon code was described. The section further showed how syndrome components are calculated and how the Chien search and error correction are performed. Section 4.7 presented the description of erasure decoding technique of Reed-Solomon codes. This section showed how both errors and erasures present in the received codeword can be detected and corrected. The chapter concluded with the presentation of possible scenarios that are considered for the simulation of BER performance of joint decoding technique in Section 4.8 and used a flowchart diagram to demonstrate how these scenarios are applied during the joint decoding operation.

Chapter 5

SIMULATION RESULTS AND ANALYSIS

5.1 Introduction

The BER performances of the PLC, VLC and joint decoded systems are presented in this chapter according to PLC and VLC channel models presented in Chapter 3 and adopting modulation scheme outlined by PLC G3 specification for narrowband operation in the frequency band between 35.9 kHz and 90.6 kHz of CENELEC-A band also described in Chapter 3 [4]. The BER results presented in this chapter are obtained under different cases, such as angle of orientation and area of the receiver and these conditions affect the power received differently. Consequently, BER performance is affected by the effects of these variations. In the simulation results presented in this chapter, a maximum distance of 3 m is considered between the source and the receiver and the distance of separation between the source and receiver planes is kept constant at 1 m. The PLC and VLC SNRs are fixed at 2 dB and 4 dB respectively. According to [154–156], PLC SNR can be considered fixed since attenuation is negligible for such a small distance in PLC transmission. However, the signal-to-noise ratio of the VLC system can vary according to distance due to attenuation [157] but in the simulations, it is kept constant so that the effects of angle of orientation and area of the receiver can be properly studied. The cases considered during the simulations are as follows:

- I. Angle of orientation between source and receiver. Under this condition, the area of the receiver (A) is kept constant at 1 mm^2 and angle of orientation (θ) is varied between 0° and 15° . That is, $\theta = 0^\circ, 10^\circ$ and 15° .
- II. Effective area of the receiver. Under this condition, the angle of orientation is kept constant at 5° and area of the receiver is varied between 0.1 mm^2 and 1 mm^2 . That is, $A = 0.1 \text{ mm}^2, 0.5 \text{ mm}^2$ and 1 mm^2 .

From the above two cases, different scenarios for each case can be formulated that will enable proper investigation of effects of the joint decoding technique. Simulations are then carried out to observe how each scenario affects the BER performance. However, before applying the joint decoding techniques, simulation of the system according to PLC G3 is performed. The scenarios that are applied to each case for joint decoding are described below.

1. Joint soft decision decoding (JSDD) at the convolutional decoder and the Reed-Solomon decoder (RSD) is removed.
 - i. Joint decoding is applied at the convolutional decoder (CD) at $\theta = 0^\circ$.
 - ii. Joint decoding is applied at the convolutional decoder (CD) at $\theta = 10^\circ$.
 - iii. Joint decoding is applied at the convolutional decoder (CD) at $\theta = 15^\circ$.

The above three scenarios are repeated for different values of effective area of the receiver. That is, $A = 0.1 \text{ mm}^2, 0.5 \text{ mm}^2, 1 \text{ mm}^2$. Therefore, there are six scenarios for performing JSDD at CD. The JSDD is only applied at CD whereas JHDD is applied at both CD and Reed-Solomon decoder (RCD).

2. Joint hard decision decoding (JHDD) at $\theta = 0^\circ, 10^\circ$ and 15° .
 - i. Joint decoding is performed at the convolutional decoder (CD) while the Reed-Solomon decoder (RSD) is ignored.
 - ii. Joint decoding is performed at the CD and output of the CD is then decoded using the RSD.

- iii. Joint decoding is applied at the CD and output of the CD is decoded using the RSD by applying the erasure decoding (ED) at RSD.
 - iv. Decode the output of each channel separately using their individual CD and the outputs are combined and jointly decoded at the RSD.
 - v. Decode the output of each channel separately using their individual CD and the outputs are combined and jointly decoded at the RSD by applying the ED at the RSD.
3. Joint hard decision decoding (JHDD) at $A = 0.1 \text{ mm}^2, 0.5 \text{ mm}^2, 1 \text{ mm}^2$.
- i. Joint decoding is performed at the CD while the RSD is ignored.
 - ii. Joint decoding is performed at the CD and output of the CD is then decoded using the RSD.
 - iii. Joint decoding is applied at the CD and output of the CD is decoded using the RSD by applying the ED at the RSD.
 - iv. Decode the output of each channel separately using their individual CD and the outputs are combined and jointly decoded at the RSD.
 - v. Decode the output of each channel separately using their individual CD and the outputs are combined and jointly decoded at the RSD by applying the ED at the RSD.

The BER is measured by comparing the transmitted and the received signals and then calculating the number of errors accumulated over the total number of bits transmitted [8]. The BER performance is expressed in terms of SNR in some cases and in terms of distance in other cases.

The RS encoder uses the (255,239) RS code and the encoded binary sequence coming out from its output is transferred to the input end of the convolutional encoder where every input bit is encoded using a standard code rate of $1/2$, constraint length (K) of 7 and generator polynomial of [171 133] [15]. Matlab simulations are used to determine the BER performance in terms of SNR and distance considering AWGN channel with LOS

propagation for the VLC system and AWGN channel with impulsive noise distribution for the PLC system.

5.2 BPSK Modulation Scheme

The BPSK modulation scheme is adopted per subcarrier during transmission in order to support up to 33.4 kbps data rate during normal mode transmission [4]. The phases of the carriers in the adjacent symbols are then used as reference to detect the phases of the current carriers [70]. The graph in Fig. 5.1 compares the BER performance in terms of SNR per carrier for both theoretical and simulated BPSK. It can be observed that the performance obtained through simulation is almost the same at each SNR value as the theoretical performance.

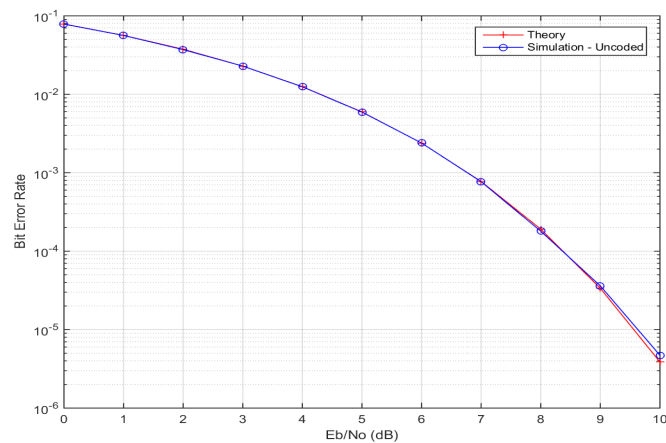


FIGURE 5.1: BPSK modulation over AWGN channel

5.3 Convolutional and Reed-Solomon Codes

The effect of Reed-Solomon, convolutional and concatenated Reed-Solomon and convolutional coding on the BPSK system over AWGN channel is shown in Fig. 5.2.

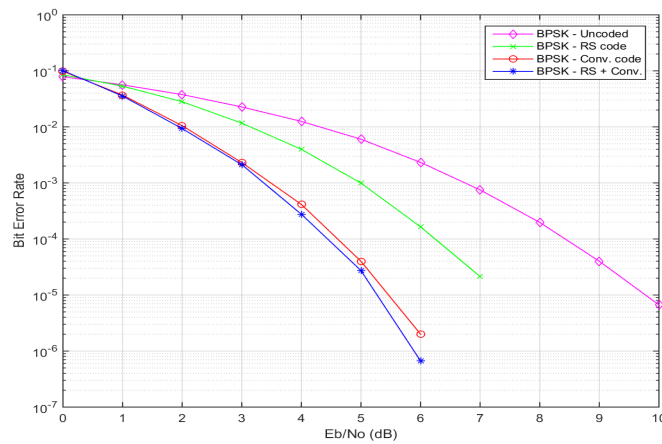


FIGURE 5.2: Effect of (255,239) Reed-Solomon, (7,[133 171]) convolutional and concatenated (255,239) Reed-Solomon and (7,[133 171]) convolutional coding on BPSK system over AWGN channel

It is observed that BER performance increases as the signal to noise ratio increases. From the graph in Fig. 5.2, it can be observed that as SNR value increases, the BER performance increases as well in all four cases, this implies that for better performance, the SNR must be high (i.e. noise must be as low as possible). It can also be seen that coding improves the BER performance of the BPSK system. It can be seen that concatenated RS and convolutional coding outperforms other coding schemes while convolutional coding outperforms RS coding. The difference between convolutional and concatenated RS and convolutional coding was not visible at low SNR but as SNR increases, the difference becomes more noticeable. Thus, the simulation results for the joint decoding technique presented in this research are obtained using concatenated RS and convolutional codes in order to obtain improved system performance.

5.4 PLC and VLC Channels

The BER performance of concatenated RS and convolutional codes modulated using BPSK modulation scheme and transmitted over PLC and VLC channels is shown in Figs. 5.3 and 5.4. The PLC channel is modeled as AWGN channel with impulsive noise distribution [12] and the VLC channel is modeled as AWGN channel with line-of-sight

(LOS) propagation effect [157]. In the Matlab simulations for the PLC channel, a fixed SNR value of 2 dB, impulsive index, $A = 0.1$ and ratio of Gaussian to impulsive noise, $\Gamma = 0.0001$ were used. For the VLC channel, a fixed SNR value 4 dB was used.

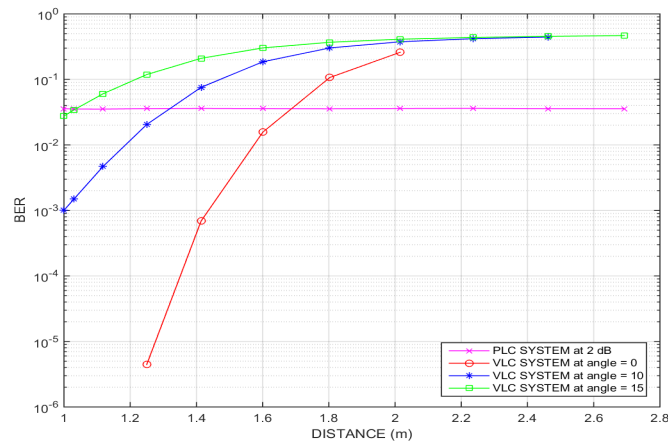


FIGURE 5.3: BER vs. distance for PLC channel and VLC channel for different angles of orientation between the source and the receiver using concatenated (255,239) Reed-Solomon and (7,[133 171]) convolutional code and BPSK modulation scheme

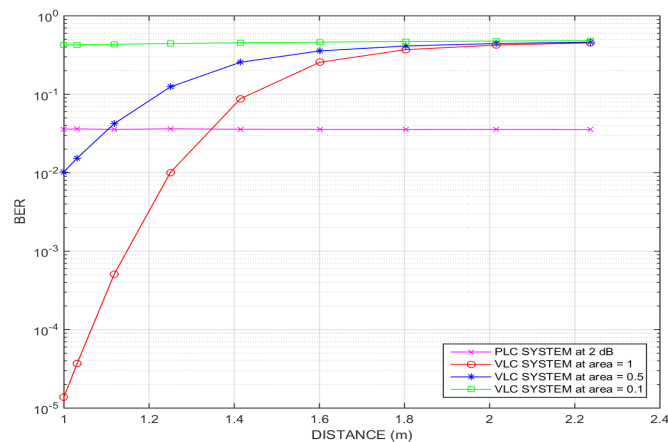


FIGURE 5.4: BER vs. distance for PLC channel and VLC channel for different effective receiver areas using concatenated (255,239) Reed-Solomon and (7,[133 171]) convolutional code and BPSK modulation scheme

From Figs. 5.3 and 5.4, it can be noticed that BER performance of the PLC system remains constant as the distance between the source and the receiver increases. On the other hand, the BER performance of the VLC system decreases as the distance from the

source increases. This degradation in the BER performance is associated with the effects of attenuation that heavily affect the VLC transmission. From the graph in Fig. 5.3, it can be seen that as the angle of orientation increases (i.e. direct LOS decreases), the BER performance decreases. This is because an increase in the angle of orientation leads to an increase in the distance between the source and the receiver and this results in increase in the attenuation. The attenuation weakens the strength of the signal resulting in less signal power being received at the receiver and consequently, the BER performance of the system suffers. Maximum signal power is received at $\theta = 0^\circ$ because the receiver is directly positioned below the source. Similarly from Fig. 5.4, an increase in the effective area of the receiver leads to better BER performance. This is because increase in the effective area results in more incident signal power being captured by the receiver and more signal at the receiver means an improvement in the BER performance. Maximum signal power is captured at the receiver when the effective area is at maximum, i.e. $A = 1 \text{ mm}^2$.

The graphs presented in Figs. 5.3 and 5.4 show that the PLC system performs better than the VLC system at certain distances from the transmitter. From Figs. 5.4, it can be observed that up to almost 1.4 m from the source, the VLC system provides better BER performance and as such the receiver can rely on the VLC system for better signal quality up to this distance. However, VLC system in Figs. 5.3 provides better BER performance up to 1.65 m and the performance becomes worse than the PLC system. Therefore at distance further than 1.65 m, the receiver can rely on PLC system for better signal quality but BER performance provided by the PLC channel is not as good as that provided by the VLC channel at distances much closer to the source. Thus, there is a need for a system that can harness the advantages provided by both systems to provide better signal quality than PLC and VLC systems at almost any distance from the source. To achieve this purpose, the joint decoding technique is utilized.

5.5 Joint Soft Decision Decoding Technique at Different Angles of Orientation

The angle of orientation determines the degree of line of sight (LOS) between the source and the receiver. A small value of angle of orientation implies that the receiver is at better LOS with respect to the source and as such, a better BER performance is expected. In Figs. 5.5 to 5.7, the simulation results of the joint soft decision decoding application at different degrees of LOS between the source and the receiver are presented.

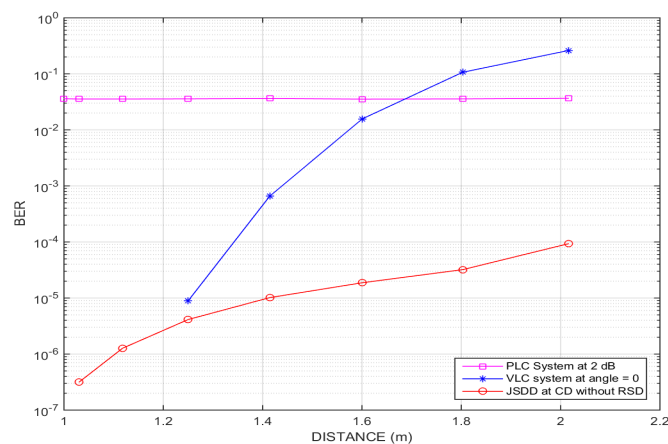


FIGURE 5.5: The joint soft decision decoding technique is performed at the convolutional decoder with the Reed-Solomon decoder removed for $\theta = 0^\circ$

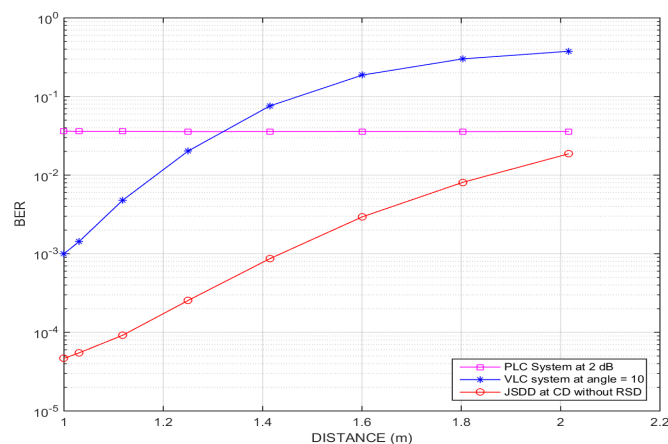


FIGURE 5.6: The joint soft decision decoding technique is performed at the convolutional decoder with the Reed-Solomon decoder removed for $\theta = 10^\circ$

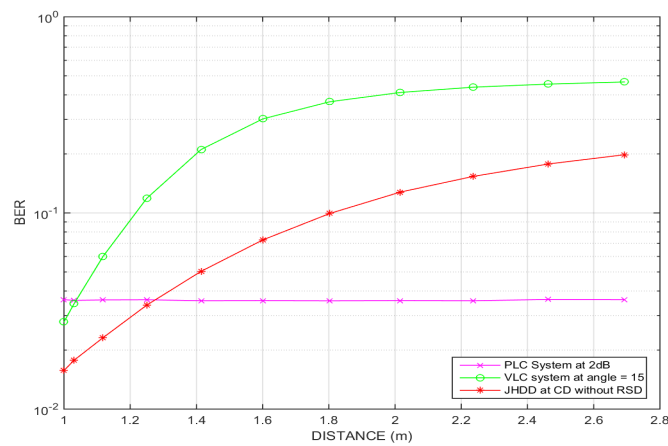


FIGURE 5.7: The joint soft decision decoding technique is performed at the convolutional decoder with the Reed-Solomon decoder removed for $\theta = 15^\circ$

5.6 Joint Soft Decision Decoding Technique at Different Effective Receiver Areas

The surface area of the receiver (PD) is responsible for capturing the incident signal power radiating from the source (LED). However, depending on the alignment of the receiver with respect to the source, the incident signal power can be captured by the entire surface area of the receiver or by only a portion of it. Thus, the effective area of the receiver refers to the actual portion of the total surface area of the receiver that captures the incident signal power. In Figs 5.8 to 5.10, the joint soft decision decoding at different receiver's areas is demonstrated.

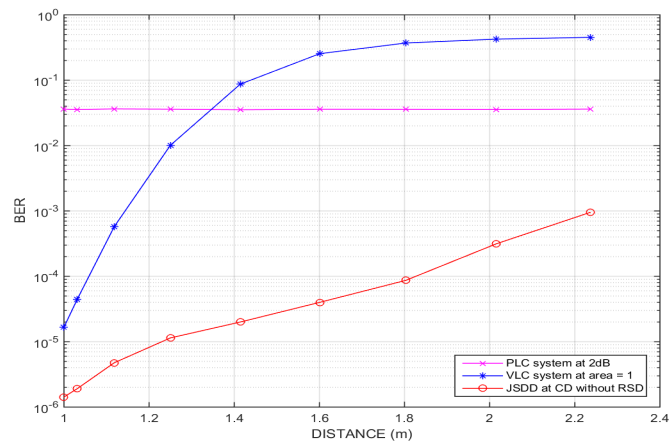


FIGURE 5.8: The joint soft decision decoding technique is performed at the convolutional decoder with the Reed-Solomon decoder removed for $A = 1 \text{ mm}^2$

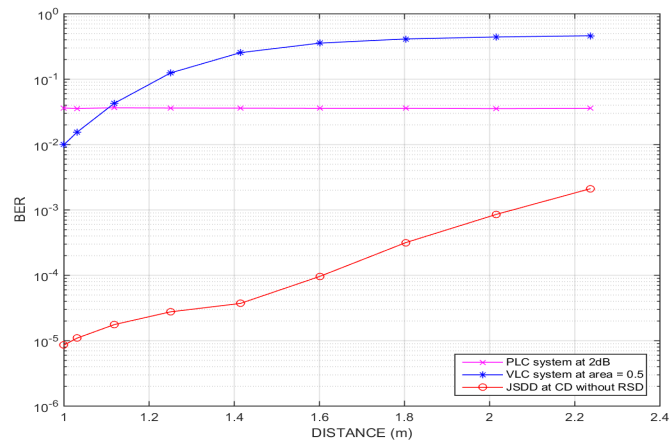


FIGURE 5.9: The joint soft decision decoding technique is performed at the convolutional decoder with the Reed-Solomon decoder removed for $A = 0.5 \text{ mm}^2$

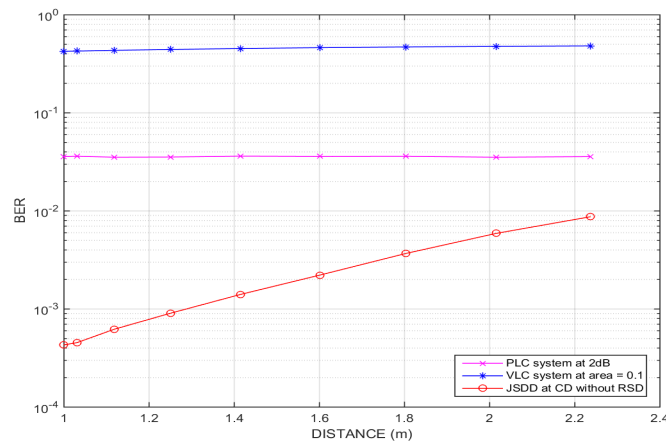


FIGURE 5.10: The joint soft decision decoding technique is performed at the convolutional decoder with the Reed-Solomon decoder removed for $A = 0.1 \text{ mm}^2$

The joint soft decision decoding is applied only at the convolutional decoder. From Figs. 5.5 to 5.7, it can be observed that an increase in the angle of orientation leads to a decrease in the BER performance due to loss of direct LOS between the source and the receiver which results in less signal power being captured by the receiver. From Figs. 5.8 to 5.10, it is seen that reducing the effective area of the receiver directly reduces the amount of signal power captured by the receiver which impacts negatively on the BER performance of both VLC and joint decoded systems.

5.7 Joint Hard Decision Decoding Technique at Different Angles of Orientation

The diagrams shown in Figs. 5.11 to 5.15 represent the BER performance of the VLC and joint decoded systems when there is a perfect LOS between the source and the receiver. In other words, the angle of orientation between the source and the receiver is at $\theta = 0^\circ$. It should be emphasized that under this condition, the receiver's movements relative to the source are only possible along the vertical direction since both the source and the receiver are perfectly aligned with each other.

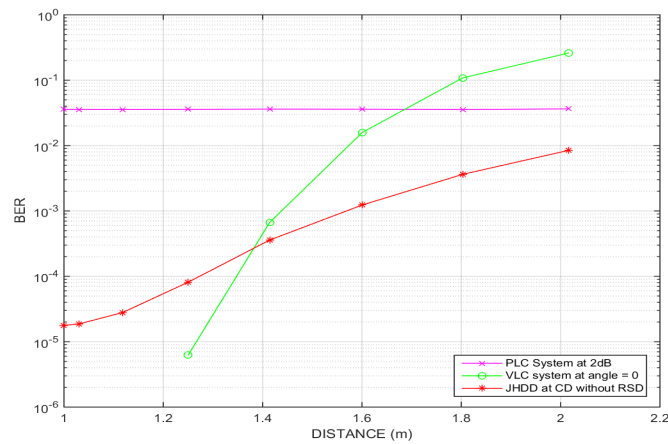


FIGURE 5.11: The joint hard decision decoding technique is performed at the convolutional decoder with the Reed-Solomon decoder removed for $\theta = 0^\circ$

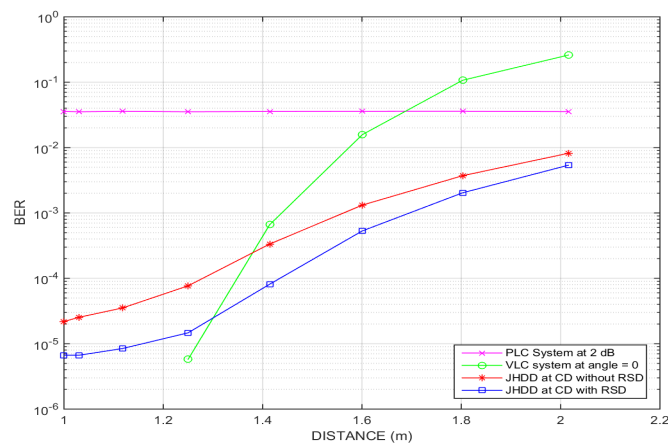


FIGURE 5.12: The joint hard decision decoding technique is performed at the convolutional decoder. Output of the convolutional decoder is further decoded at the Reed-Solomon decoder for $\theta = 0^\circ$

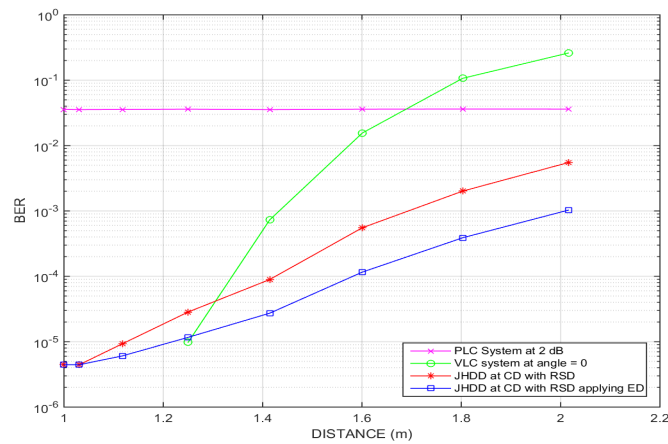


FIGURE 5.13: The joint hard decision decoding technique is performed at the convolutional decoder. Output of convolutional decoder is further decoded at the Reed-Solomon decoder applying the erasure decoding for $\theta = 0^\circ$

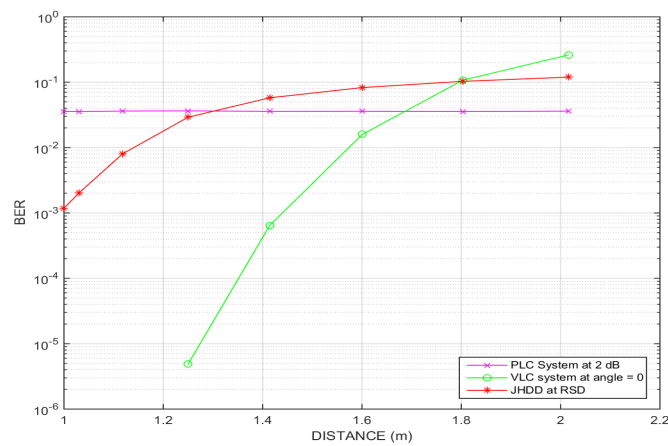


FIGURE 5.14: Outputs of the PLC and the VLC channels are decoded individually at the convolutional decoders. Outputs the convolutional decoders are combined and the joint hard decision decoding is performed at the Reed-Solomon decoder for $\theta = 0^\circ$

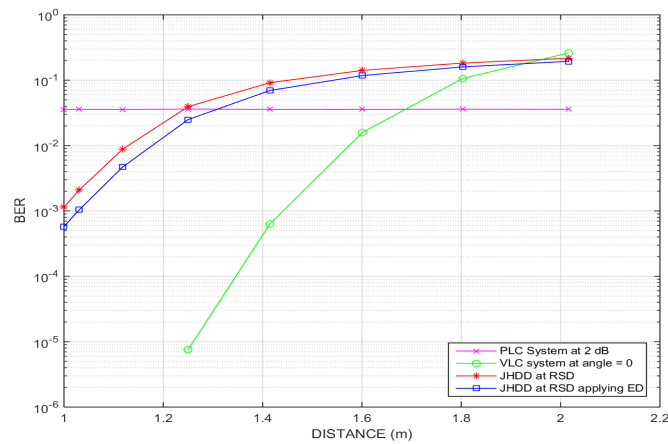


FIGURE 5.15: Outputs of the PLC and the VLC channels are decoded individually at the convolutional decoders. Outputs the convolutional decoders are combined and the joint hard decision decoding is performed at the Reed-Solomon decoder applying the erasure decoding for $\theta = 0^\circ$

From Fig. 5.11, it can be seen that at an angle of 0° , only a distance of 2 m directly below the source can be reached. This is because at an angle of 0° , movements relative to the source is only possible in the vertical direction directly below the source since horizontal component of the position vector is zero. It can also be observed that at close distance (up to 1.4 m) to the source, the VLC system outperforms both PLC and JD systems. The BER of the VLC system at close distance is approximately zero which implies that at close distance the receiver can depend on the VLC system to provide better signal quality for the receiver. However, as the receiver moves further away (beyond 1.4 m) from the source, the JD system performs better than both VLC and PLC systems. The best BER performance for the JD system at an angle of 0° is shown in Fig. 5.13 when the JD technique is applied at the convolutional decoder and the output is then decoded again at the Reed-Solomon decoder applying erasure decoding at the Reed-Solomon decoder. It can be seen that by applying erasure decoding at the RSD, the JD system outperforms the VLC system from a closer distance (1.25 m) than 1.4 m obtained in Fig. 5.11. The BER performance of the JD system however worsened when joint decoding was performed at RSD as shown in Figs. 5.14 and 5.15. This is as a result of combining hard information bits at the output of the convolutional decoders. Therefore, at an

angle of 0° and distance > 1.4 m, the receiver can depend on the JD system for better signal quality at the receiver.

Having investigated the effects of joint decoding when there is a perfect LOS between the source and the receiver, the diagrams shown in Figs. 5.16 and 5.20 will describe what happens when the angle of orientation is increased from 0° to 10° . This results in the receiver losing its perfect LOS with the source and also at further distance from the source. Consequently, the BER performance degrades.

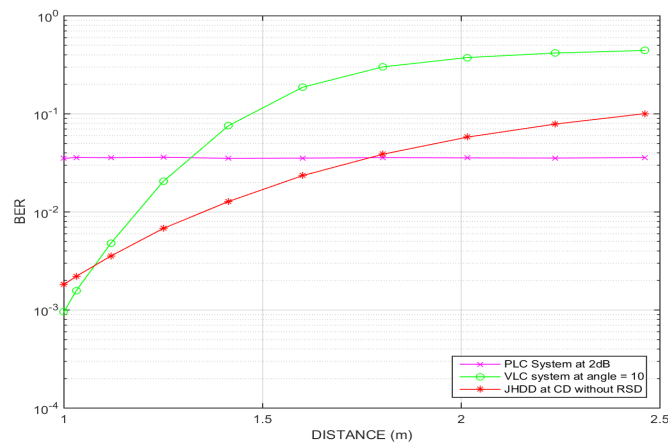


FIGURE 5.16: The joint hard decision decoding technique is performed at the convolutional decoder with the Reed-Solomon decoder removed for $\theta = 10^\circ$

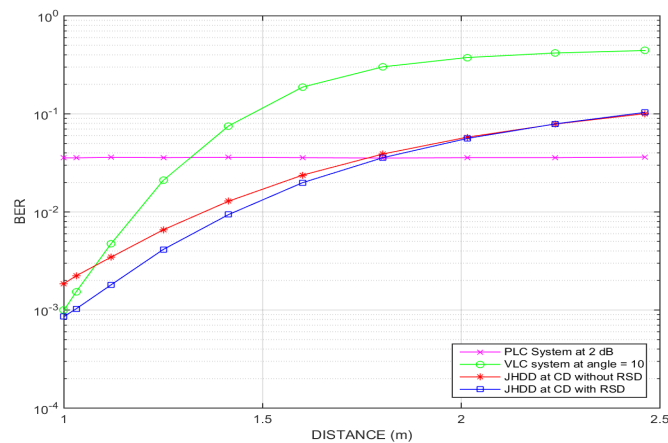


FIGURE 5.17: The joint hard decision decoding technique is performed at the convolutional decoder. Output of the convolutional decoder is further decoded at the Reed-Solomon decoder for $\theta = 10^\circ$

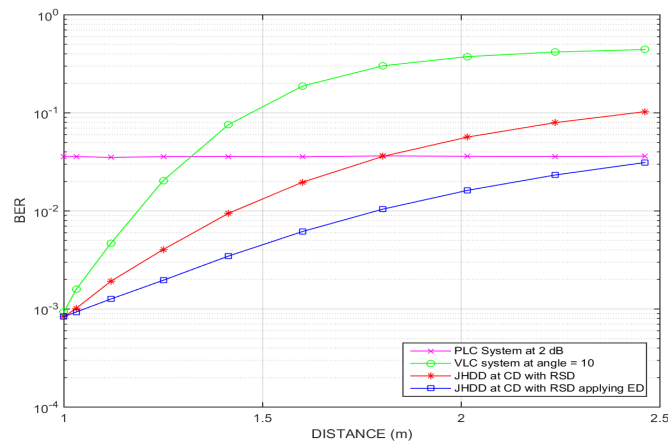


FIGURE 5.18: The joint hard decision decoding technique is performed at the convolutional decoder. Output of convolutional decoder is further decoded at the Reed-Solomon decoder applying the erasure decoding for $\theta = 10^\circ$

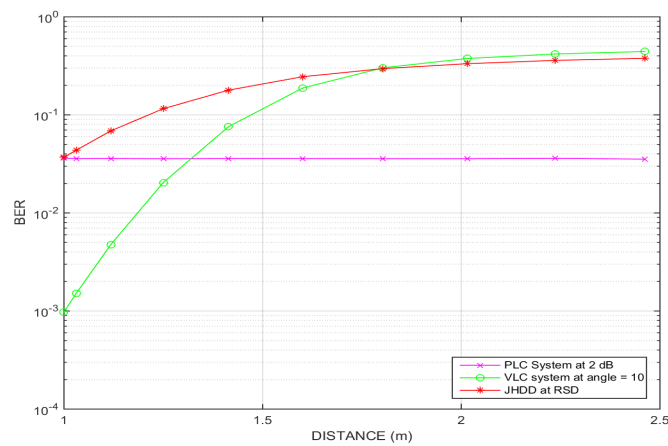


FIGURE 5.19: Outputs of the PLC and the VLC channels are decoded individually at the convolutional decoders. Outputs the convolutional decoders are combined and the joint hard decision decoding is performed at the Reed-Solomon decoder for $\theta = 10^\circ$

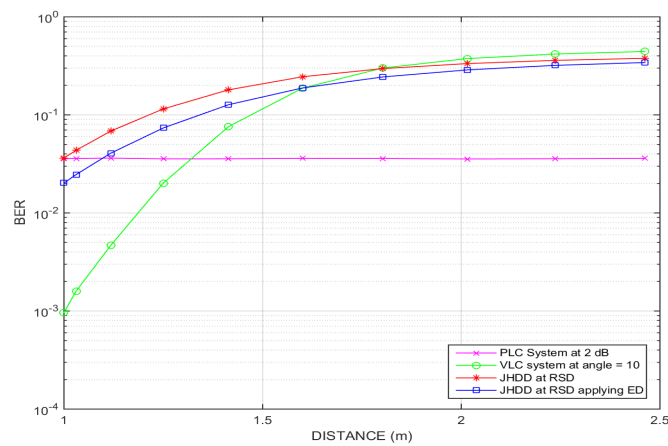


FIGURE 5.20: Outputs of the PLC and the VLC channels are decoded individually at the convolutional decoders. Outputs the convolutional decoders are combined and the joint hard decision decoding is performed at the Reed-Solomon decoder applying the erasure decoding for $\theta = 10^\circ$

The simulation results showing the effects of further increasing the angle of orientation from 10° to 15° are shown in Figs. 5.21 to 5.25. As was the case at $\theta = 10^\circ$, increasing the angle of orientation to 15° causes the receiver to lose more LOS advantage with the source by pushing the receiver much further away from the source and as a result, the BER performance becomes worse than it was at $\theta = 10^\circ$ for both VLC and joint decoded systems.

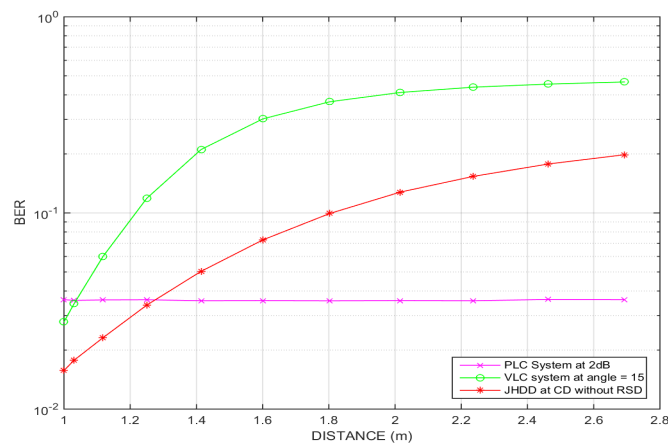


FIGURE 5.21: The joint hard decision decoding technique is performed at the convolutional decoder with the Reed-Solomon decoder removed for $\theta = 15^\circ$

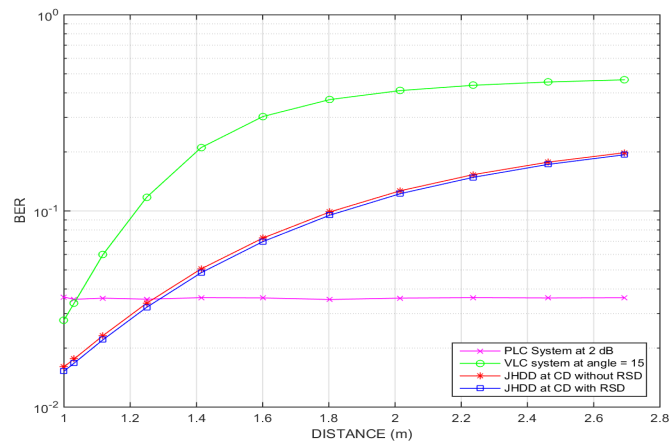


FIGURE 5.22: The joint hard decision decoding technique is performed at the convolutional decoder. Output of the convolutional decoder is further decoded at the Reed-Solomon decoder for $\theta = 15^\circ$

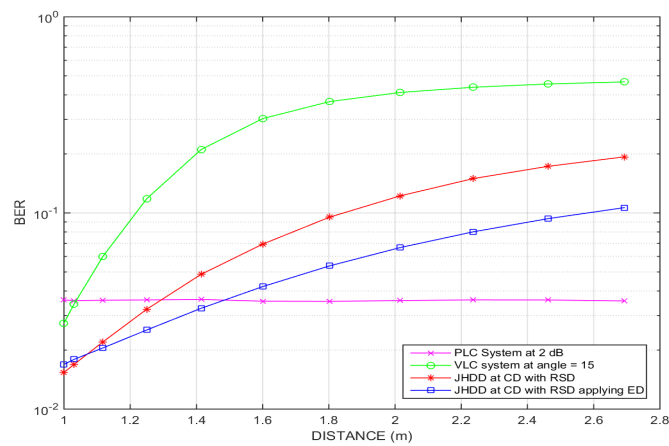


FIGURE 5.23: The joint hard decision decoding technique is performed at the convolutional decoder. Output of convolutional decoder is further decoded at the Reed-Solomon decoder applying the erasure decoding for $\theta = 15^\circ$

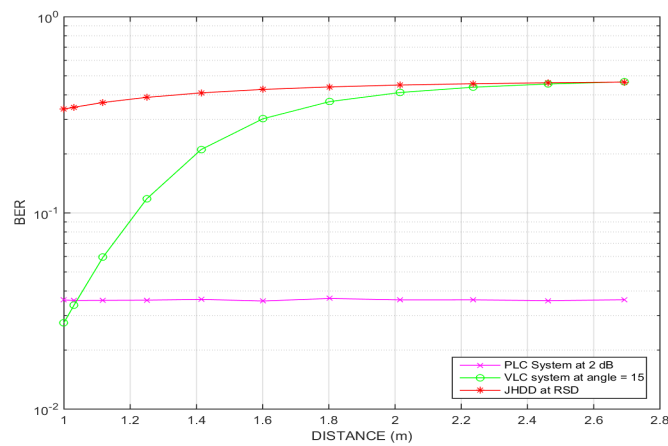


FIGURE 5.24: Outputs of the PLC and the VLC channels are decoded individually at the convolutional decoders. Outputs the convolutional decoders are combined and the joint hard decision decoding is performed at the Reed-Solomon decoder for $\theta = 15^\circ$

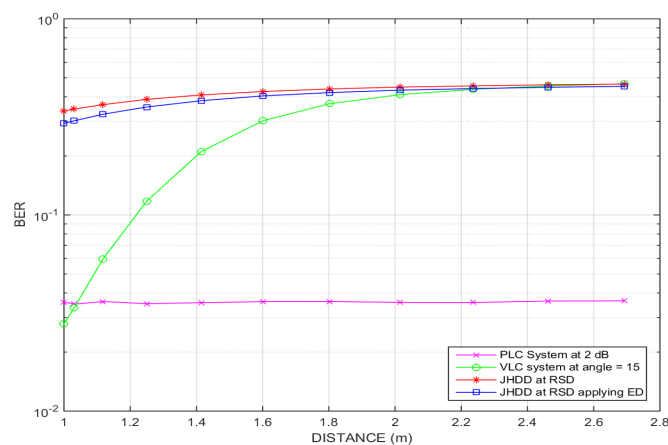


FIGURE 5.25: Outputs of the PLC and the VLC channels are decoded individually at the convolutional decoders. Outputs the convolutional decoders are combined and the joint hard decision decoding is performed at the Reed-Solomon decoder applying the erasure decoding for $\theta = 15^\circ$

By increasing the angle of orientation to 10° and 15° , as depicted in Figs. 5.16 to 5.20 and 5.21 to 5.25 respectively, distances of approximately 2.5 m and 2.7 m can be reached from the source. However, an increase in distance results in a decrease in the BER performance of both the VLC and the JD systems due to an increase in the attenuation affecting the VLC system which ultimately reduces the incident signal power at the receiver. The BER performance at angle 10° and 15° follows the same pattern as at angle

0° where the best performance is obtained by applying the JD technique at the CD and then decoding the output of the CD at the RSD deploying erasure decoding at the RSD and the worst BER performance is obtained when the outputs of the two convolutional decoders are combined and jointly decoded at the RSD.

The simulation results for application of joint decoding at both inner and outer decoders when the angle of orientation between the source and the receiver is 0°, 10° and 15° are presented in Figs. 5.11 to 5.25. It can be observed from these graphs that an increase in the angle of orientation leads to a decrease in the BER performance of both the VLC and the joint decoded systems. This is because an increase in the angle results in an increase in the distance of separation between the source and the receiver. As the receiver moves further away from the source, it gradually loses direct LOS advantage and as a result, the BER performance of the system decreases.

5.8 Joint Hard Decision Decoding Technique at Different Effective Receiver Areas

In Figs. 5.26 to 5.40, the effect of the joint decoding application at different effective areas of the receiver is demonstrated. The angle of orientation was kept constant at 5° and the maximum distance that can be reached at this angle was approximately 2.2 m. From the graphs, it is noticed that the BER performance deteriorates as the effective receiver area decreases. This is in agreement with the theoretical expectation since a decrease in the receiver area leads to a decrease in the amount of incident signal power being captured by the receiver. Thus, a decrease in the amount of signal power at the receiver results in the degradation of the BER performance as the signal captured at the receiver is dominated by noise.

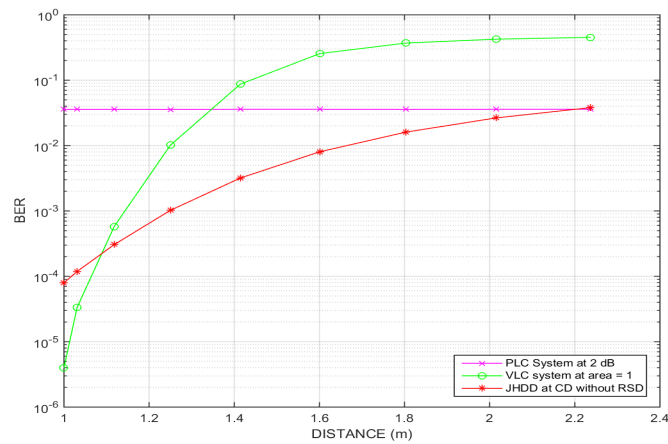


FIGURE 5.26: The joint hard decision decoding technique is performed at the convolutional decoder with the Reed-Solomon decoder removed for $A = 1 \text{ mm}^2$

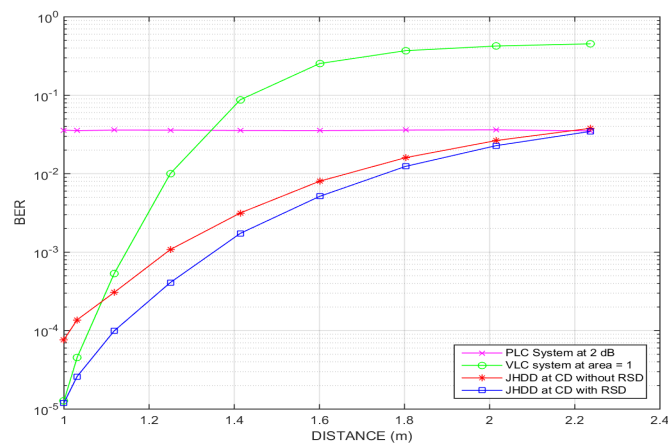


FIGURE 5.27: The joint hard decision decoding technique is performed at the convolutional decoder. Output of the convolutional decoder is further decoded at the Reed-Solomon decoder for $A = 1 \text{ mm}^2$

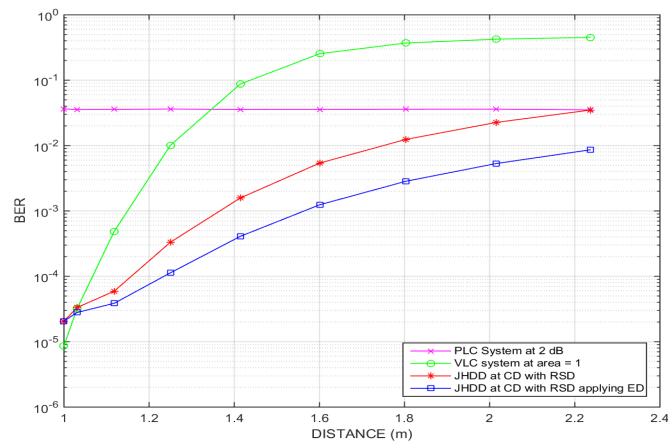


FIGURE 5.28: The joint hard decision decoding technique is performed at the convolutional decoder. Output of the convolutional decoder is further decoded at the Reed-Solomon decoder applying the erasure decoding for $A = 1 \text{ mm}^2$

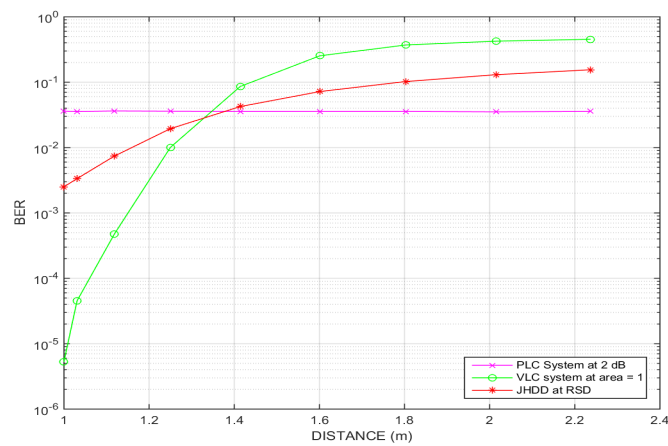


FIGURE 5.29: Outputs of the PLC and the VLC channels are decoded individually at the convolutional decoders. Outputs the convolutional decoders are combined and the joint hard decision decoding is performed at the Reed-Solomon decoder for $A = 1 \text{ mm}^2$

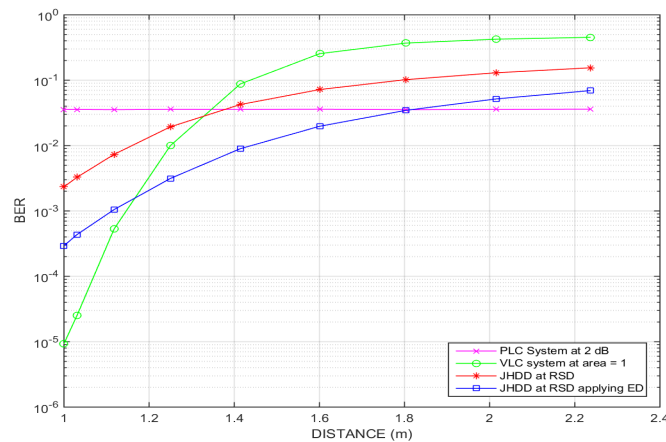


FIGURE 5.30: Outputs of the PLC and the VLC channels are decoded individually at the convolutional decoders. Outputs the convolutional decoders are combined and the joint hard decision decoding is performed at the Reed-Solomon decoder applying the erasure decoding for $A = 1 \text{ mm}^2$

The graphs in Figs. 5.26 to 5.30 show the simulation results obtained by applying the JD technique at either the CD or the RSD when the effective receiver area is kept at 1 mm^2 . In Fig. 5.26, the JD was applied at the CD while the RSD was ignored. It can be seen from the graph that the JD system has better BER performance than both VLC and PLC systems from a distance of 1.1 m to approximately 2.2 m. Thus, within this region, the receiver can rely on the the JD system to provide better signal quality at the receiver. In Fig. 5.27, the JD was applied at the CD and the output of the CD was then decoded using the RSD. It can be seen that by decoding the output of the CD using the RSD, it is possible to gain more system performance in terms of BER since the the joint decoded system outperforms the VLC system from a shorter distance (much closer to the source). However, as the receiver moves further away from the source, the BER performance gradually approaches that obtained in Fig. 5.26. In Fig. 5.27, erasure decoding was then used at the RSD in order to gain more system performance. It can be observed that the joint decoded system now outperforms the VLC system from a distance of 1 m. Thus, it is possible to obtain a system that outperforms both the PLC and the VLC systems by applying the JD at the CD and then use ED at the RSD to decode the output of the CD. The BER performance drastically worsened as the JD was applied at the RSD as shown in Figs. 5.29 and 5.30. The BER performance became much worse than that

of the VLC system and at a distance of 1.3 m, it became worse than that of the PLC system. To apply the JD at the RSD, first decode the soft information coming from each channel separately using the CD and combine the hard information coming out of the two convolutional decoders and then decode using the RSD.

Having observed the effect of joint decoding at maximum incident signal reception in Figs. 5.26 to 5.30, the graphs in Figs. 5.31 to 5.35 demonstrate what happens when the effective area is reduced from 1 mm^2 to 0.5 mm^2 . It can be observed from these graphs that as the effective area decreases, the BER performance at each scenario decreases. This is as expected because a reduction in effective area means that less signal power is received and ultimately, the BER performance deteriorates as a result of more signal noise being received.

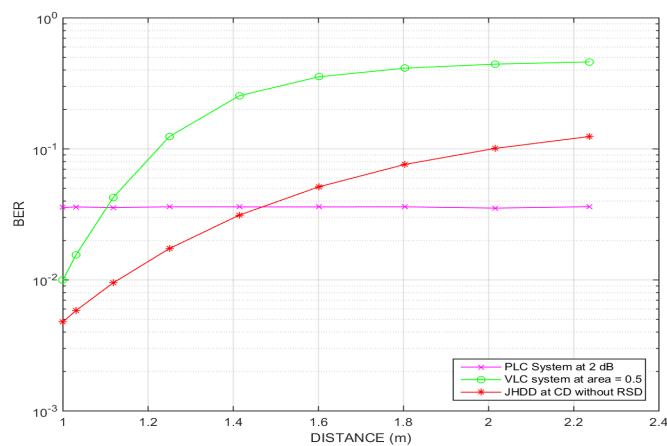


FIGURE 5.31: The joint hard decision decoding technique is performed at the convolutional decoder with the Reed-Solomon decoder removed for $A = 0.5 \text{ mm}^2$

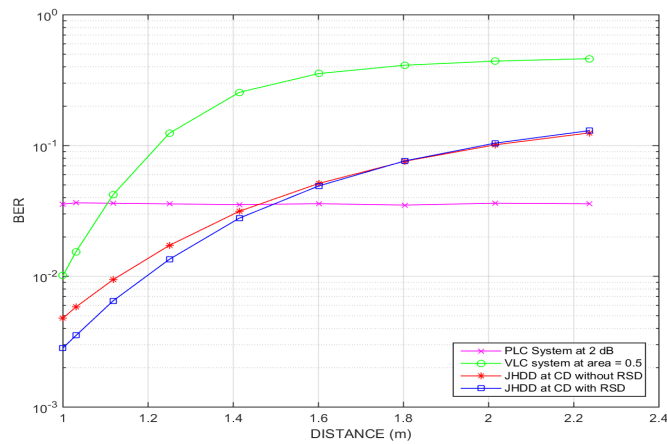


FIGURE 5.32: The joint hard decision decoding technique is performed at the convolutional decoder. Output of the convolutional decoder is further decoded at the Reed-Solomon decoder for $A = 0.5 \text{ mm}^2$

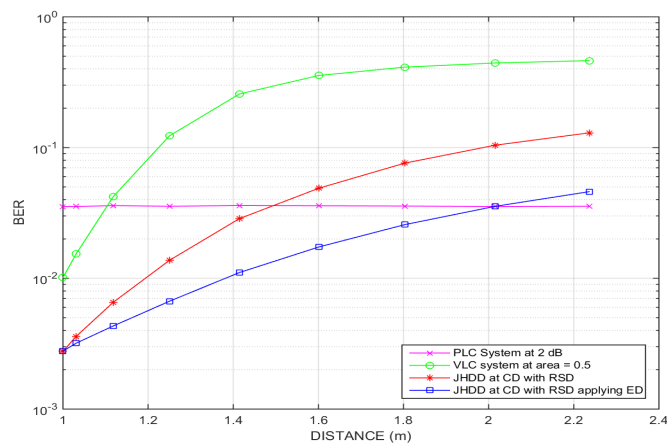


FIGURE 5.33: The joint hard decision decoding technique is performed at the convolutional decoder. Output of the convolutional decoder is further decoded at the Reed-Solomon decoder applying the erasure decoding for $A = 0.5 \text{ mm}^2$

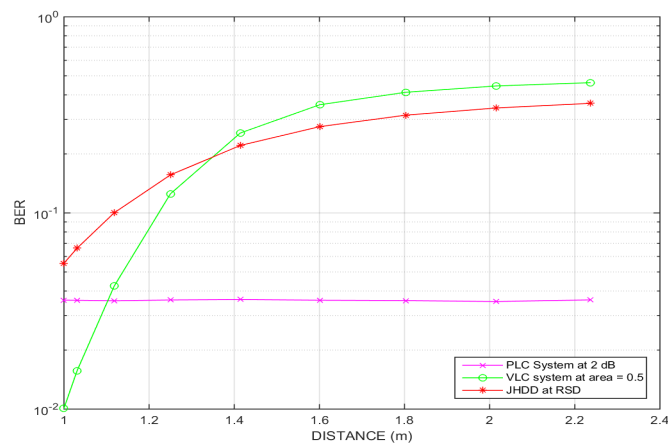


FIGURE 5.34: Outputs of the PLC and the VLC channels are decoded individually at the convolutional decoders. Outputs the convolutional decoders are combined and the joint hard decision decoding is performed at the Reed-Solomon decoder for $A = 0.5 \text{ mm}^2$

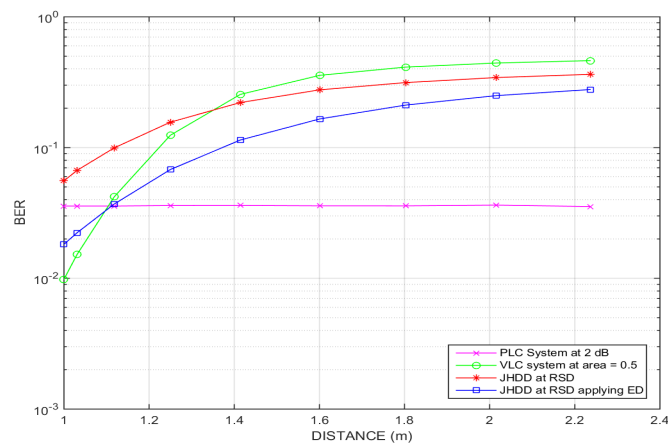


FIGURE 5.35: Outputs of the PLC and the VLC channels are decoded individually at the convolutional decoders. Outputs the convolutional decoders are combined and the joint hard decision decoding is performed at the Reed-Solomon decoder applying the erasure decoding for $A = 0.5 \text{ mm}^2$

The graphs in Figs. 5.36 to 5.40 show that a further decrease in the effective area from 0.5 mm^2 to 0.1 mm^2 results in very poor BER performance of both the VLC and the joint decoded systems. This poor BER performance can be attributed to very little signal power being captured at the receiver as the effective area has significantly reduced from 1 mm^2 to 0.1 mm^2 .

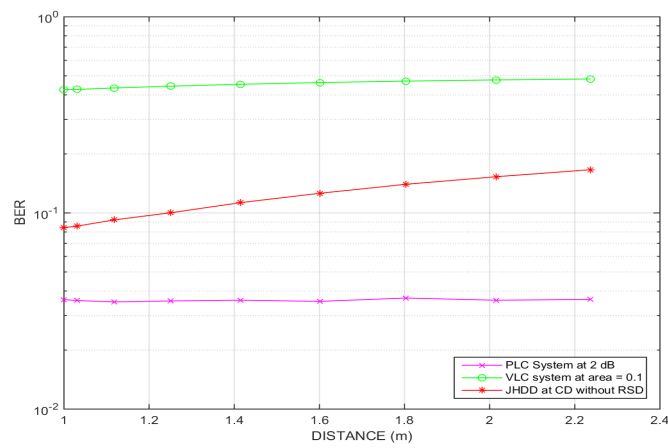


FIGURE 5.36: The joint hard decision decoding technique is performed at the convolutional decoder with the Reed-Solomon decoder removed for $A = 0.1 \text{ mm}^2$

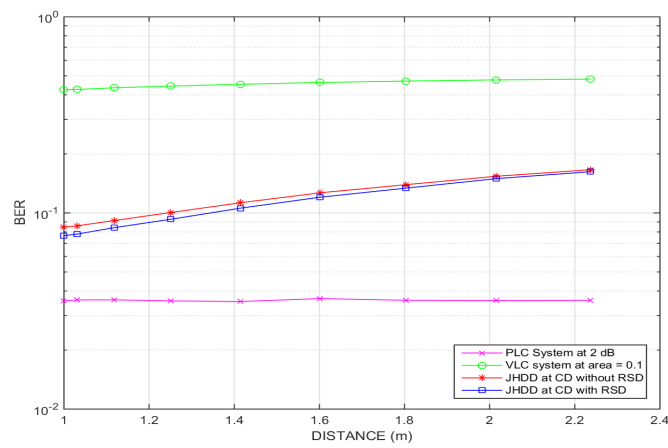


FIGURE 5.37: The joint hard decision decoding technique is performed at the convolutional decoder. Output of the convolutional decoder is further decoded at the Reed-Solomon decoder for $A = 0.1 \text{ mm}^2$

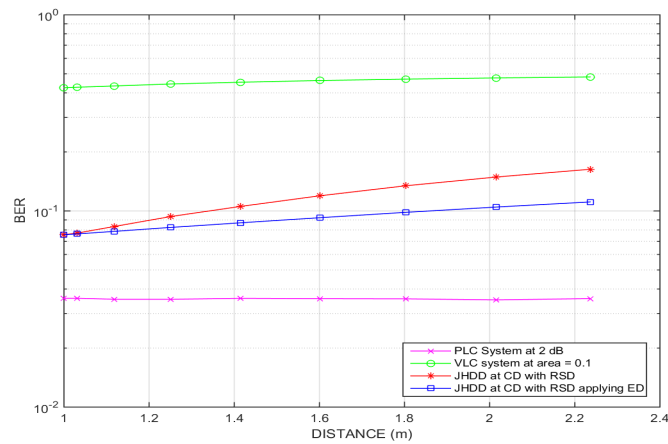


FIGURE 5.38: The joint hard decision decoding technique is performed at the convolutional decoder. Output of the convolutional decoder is further decoded at the Reed-Solomon decoder applying the erasure decoding for $A = 0.1 \text{ mm}^2$

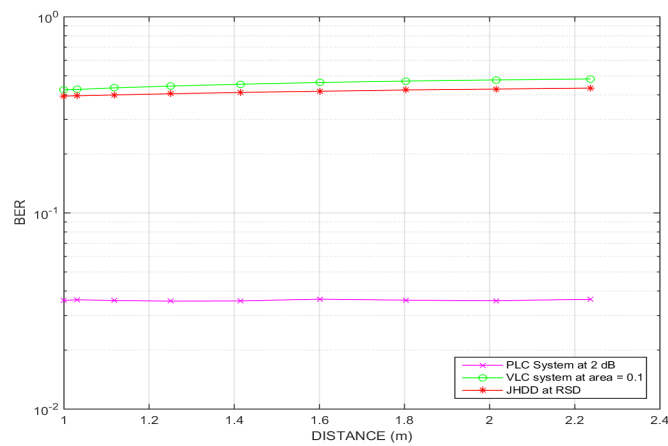


FIGURE 5.39: Outputs of the PLC and the VLC channels are decoded individually at the convolutional decoders. Outputs the convolutional decoders are combined and the joint hard decision decoding is performed at the Reed-Solomon decoder for $A = 0.1 \text{ mm}^2$

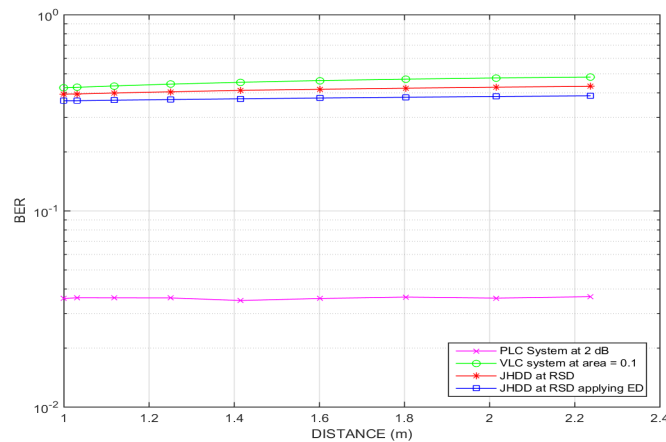


FIGURE 5.40: Outputs of the PLC and the VLC channels are decoded individually at the convolutional decoders. Outputs the convolutional decoders are combined and the joint hard decision decoding is performed at the Reed-Solomon decoder applying the erasure decoding for $A = 0.1 \text{ mm}^2$

From the simulation results presented in Section 5.5, it can be deduced that the receiver can rely on the JD system for better signal quality when moving from one position to another by keeping both the angle of orientation and effective area constant at 0° and 1 mm^2 respectively. Furthermore, the joint decoding has to be applied at the convolutional decoder and then decode the output of the convolutional decoder at the Reed-Solomon decoder applying the erasure decoding technique.

5.9 BER Analysis

How good or bad a coded communication system performs is usually measured in terms of the decoding error probability called the error probability and the coding gain compared to an uncoded system that transmits information at the same rate. The error probability can be categorized into two groups: word or block error probability and bit error probability or bit error rate [140]. This research focused on bit error probability since the information transmitted over the two channels are bit information. The BER is the probability that the decoded bit at the output of either Viterbi or Reed-Solomon decoder contains an error. To maximize the performance of the transmission system, BER

should be kept as low as possible while adhering to constraints such as power, bandwidth and decoding complexity [22].

The number of transmitted symbols per bit in a coded communication system with code rate $R = k/n$ is given as $1/R$ and the energy associated with each transmitted symbol is represented as E_s . Thus, the energy in each transmitted bit is given as [140]

$$E_b = E_s / R \quad (5.1)$$

The error probability of a coded transmission system is given as the ratio of E_b to one-sided PSD N_0 of the channel noise.

5.9.1 Decoded BER calculations for the convolutional decoder

The inner convolutional code used in this research has a code rate of 1/2 with constraint length $K = 7$ and generator polynomial of [133 171] [4]. The convolutional code was transmitted using the BPSK modulation through an AWGN channel. Thus, the upper bound on the BER can be obtained using union bound argument on the transfer function of the convolutional code [158]. Assuming that all zero sequence was transmitted, the probability that the decoder selected an incorrect path through the trellis that differs from the correct path by d bits is given by [140]

$$P(d) = \sum_k^d \binom{d}{k} p^k (1-p)^{d-k} \quad (5.2)$$

where d is odd and $k = \frac{d+1}{2}$. However, in a case where d is even, the probability is given by [140]

$$P(d) = \sum_k^d \binom{d}{k} p^k (1-p)^{d-k} + 0.5 \binom{d}{d/2} p^{d/2} (1-p)^{d/2} \quad (5.3)$$

And the upper bound on the BER using the union bound is then expressed as [159]

$$P_e \leq \sum_{d=d_{free}}^{\infty} a_d P_d \quad (5.4)$$

where a_d is the number of paths at distance d . For the convolutional code used in this research ($r = 1/2$, $k = 7, [133\ 171]$), the d_{free} value is given as 10 in [159]. This probability (5.4) is called the event probability which is the probability that at any given time, the Viterbi algorithm will select an incorrect path that introduces errors into the decoded sequence [92].

5.9.2 Decoded BER calculations for the Reed-Solomon decoder

The Reed-Solomon code is a non-binary code that uses symbols from $GF(2^m)$ and each symbol contains m bits. The RS code used in this research is from $GF(2^8)$ and its generator polynomial is given as [4]

$$G(x) = \prod_{i=1}^{2t} (x - \alpha^i) \quad (5.5)$$

where $2t = n - k$, t is the error-correcting capability of the RS code and α is the primitive element in $GF(2^8)$. The RS decoder is capable of correcting all the errors in the received codeword provided that number of errors in the received codeword does not exceed t . In a case where the number of errors exceeds t , the decoder does either of the following [160]

- Provides a mis-decoding result or
- Outputs an unchanged codeword due to decoding failure

For $t \geq 8$ and $n \geq 5t$, the probability of decoding failure is very high compared to mis-decoding and thus, the chances of mis-decoding can be ignored. Therefore, the ratio of BER to symbol error rate (SER) at the input and output of the RS decoder is the same. The BER at the output of the RS decoder is given by [161]

$$\begin{aligned} P_{bo} &= \frac{P_{bi}}{P_{si}} P_{so} \\ &= \frac{P_{bi}}{P_{si}} \frac{1}{n} \sum_{i=t+1}^n i \binom{i}{n} P_{si}^i (1 - P_{si})^{n-i} \end{aligned} \quad (5.6)$$

where P_{bi} and P_{si} are the channel BER and SER at the input of the RS decoder and P_{bo} and P_{so} are the BER and SER at the output of the RS decoder after decoding [161].

5.9.3 Decoded BER calculations for the Joint decoded system

In this research, the joint decoding is performed either at the CD or the RSD as demonstrated in Chapter 4. For the joint decoding at the CD, the BER at the input of the CD is given by

$$P_{e_{in}} = P_{e_1} + P_{e_2} - P_{e_1}P_{e_2} \quad (5.7)$$

where P_{e_1} and P_{e_2} are the BER at the output of the PLC and the VLC channels respectively. This scenario is further explained in Fig. 5.41.

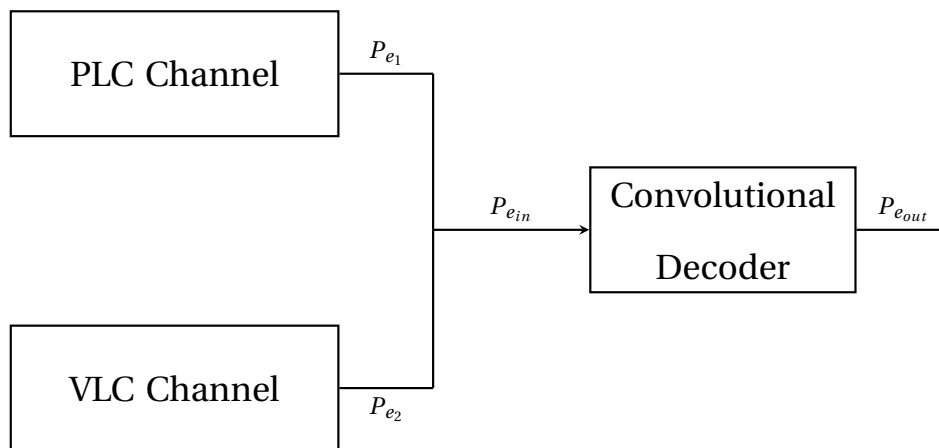


FIGURE 5.41: Decoded BER at the output of the convolutional decoder

where the $P_{e_{out}}$ is calculated using (5.4). To obtain the $P_{e_{in}}$ at the input of the RSD, (5.4) is used at the output of each convolutional decoder and the resulting P_{e_1} and P_{e_2} are then combined according to (5.7). The $P_{e_{out}}$ at the output of the RSD is then calculated using (5.6). This scenario is further explained in Fig. 5.42.

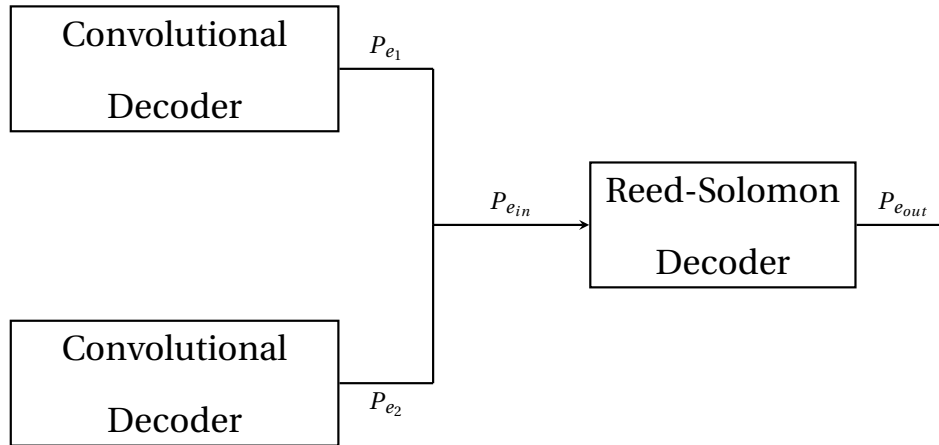


FIGURE 5.42: Decoded BER at the output the Reed-Solomon decoder

5.10 Decoding Complexity Analysis

Recently, great interest has been shown in reduced decoding complexity [162]. The decoding complexity is expressed in terms of iteration complexity of the iterative decoders where convolutional decoder lies at the heart of the iterative decoding [163]. The decoding complexity can be regarded as the number of real addition operations needed to decode a single codeword. That is, the number of operations (additions and multiplications) needed to decode a received codeword using either Berlekamp-Massey's algorithm in the Reed-Solomon decoder or the Viterbi algorithm in the convolutional decoder [164].

5.10.1 Decoding complexity of the convolutional decoder

In the simulations, a Viterbi decoder that has a rate of 1/2, constraint length (K) of 7 and generator polynomial of [133 171] was used according to PLC G3 specification [4]. The computational complexity of this iterative decoder is dependent on the number of possible codewords and the length of the input bits. In this analysis, only multiplicative operations is considered while excluding the additive operations [162]. The Viterbi algorithm iterates for every position x along α_i . Except for the first position, at each position $|\alpha_i| + 2$ the matches for all the most-likely $\psi = |\Sigma| + 1$ possible codewords are

examined [165]. The decoding process involves matching each codeword (δ_y) in a backward direction beginning with the bit at the input and ending with the bit at the position x . Thus, the number of iterations needed for matching grows according to [166]

$$I_M \sim |\alpha_i| \psi L \quad (5.8)$$

where L is the length of the codeword. For each successful matching, evaluate possible state transitions to the previously successful matches in the column $(x - |\delta_y|)$ and then obtain the most-likely path. At each state, examine all possible codewords, and the number of iterations, I_L needed to compute the state transitions. This computation grows according to [166]

$$I_L \sim |\alpha_i| \psi^2 \quad (5.9)$$

In addition to matching of codewords, the algorithm also clears all the table entries $T(.,.)$ for the next translation. Thus, the number of iterations needed for clearing, I_C is given by [162]

$$I_C \sim |\alpha_i| \psi \quad (5.10)$$

where I_C is quadratic in the worst case. The estimated total CPU time can now be obtained by combining (5.8) - (5.10) as expressed by [166]

$$\begin{aligned} T &\sim C_M I_M + C_L I_L + C_C I_C \\ &\sim C_1 |\alpha_i| \psi^2 + C_2 |\alpha_i| \psi \end{aligned} \quad (5.11)$$

where the C' s are appropriate constants and L has been integrated into C_2 . The table used to store the entries has a dimension of $|\alpha_i| + 2$ and ψ , the number of possible state transition probabilities is given by ψ^2 and the required storage space is expressed in quadratic form as [165]

$$S \sim C_3 |\alpha_i| \psi + \psi^2 \quad (5.12)$$

where C_3 is a constant whose size is dependent on the storage requirements for the table entries $T(.,.)$ which are cumulative log probabilities including the most likely path [165].

5.10.2 Decoding complexity of the Reed-Solomon decoder

The Berlekamp-Massey algorithm (BMA) introduced by Massey allows for error and/or erasure decoding of RS codes with a decoding complexity of $\mathcal{O}(n^2)$ [164]. The decoding complexity is determined by the number of multiplications, bearing in mind that both multiplication and inversion over $GF(2^m)$ requires an area-time complexity of $\mathcal{O}(m^2)$, whereas an addition operation requires an area-time complexity of $\mathcal{O}(m)$ [167]. The decoding complexity due to inversion can be ignored since the number of inversions is much smaller than those of multiplications [23]. The numbers of multiplications and additions are both given by $\mathcal{O}(n^2)$ [164]. The summary of the error-only decoding complexity associated with BMA for RS (255,239) code is shown in Table. 5.1.

TABLE 5.1: Error-only decoding complexity of Berlekamp-Massey algorithm [23]

	Multiplications	Additions	Inversions
Syndrome Computation	$2t(n-1)$	$2t(n-1)$	0
Key Equation Solver	$4t(2t+2)$	$2t(2t+1)$	0
Chien Search	$n(t-1)$	nt	0
Forney's Formula	$2t^2$	$t(2t-1)$	t
Total	$3nt+10t^2-n+6t$	$3nt+6t^2-t$	t

The decoding complexity analysis can now be extended to the case where both errors and erasures decoding is involved. Under this condition, erasure-locator polynomial and modified syndrome polynomial are first computed [168]. This is followed by the computation of error-locator polynomial using key equation solver and then error and erasure values are then determined using Forney's algorithm [169]. The analysis of decoding complexity assuming error and erasure decoding for RS (255,239) code is shown in Table. 5.2.

TABLE 5.2: Error and erasure decoding complexity of Berlekamp-Massey algorithm [23]

(255,239)	Multiplications	Additions	Inversions	Overall
Syndrome Computation	149	4012	0	6396
Key Equation Solver	1088	1040	16	18704
Chien Search	586	6900	0	16276
Forney's Formula	512	496	16	8944
Total	2335	12448	32	50320

The decoding complexity is dependent on the number of multiplicative and additive operations that the algorithm (Viterbi or Berlekamp-Massey) has to perform in order to successfully decode a received codeword. From the simulation results presented in this chapter, it can be seen that best BER performance for the joint decoded system is obtained at convolutional decoder. That is, when JSDD is performed at the convolutional decoder for either different angles of orientation or effective areas of the receiver.

By performing the joint decoding at the convolutional decoder, only one decoder is utilized. Thus, reducing the number of multiplications and additions compared to either the joint decoding at the RS decoder (three decoders used in this case) or the benchmark decoding scheme (two decoders used in this case). Therefore, the joint decoding technique reduces complexity as it requires less number of multiplicative and additive operations to produce better BER performance.

5.11 Summary

This chapter consists of ten sections. The chapter started with an explanation of what the chapter contains in Section 5.1. The cases and scenarios utilized in the application of joint decoding technique were also presented in this section. Section 5.2 presented the BER performance of theoretical and uncoded simulated BPSK modulation scheme passed over an AWGN channel. In Section 5.3, the effect of applying coding to BPSK modulation was demonstrated. The BER performance of Reed-Solomon (255,239) coding, convolutional (7,[133 171]) coding and concatenated Reed-Solomon (255,239) and convolutional (7,[133 171]) coding was compared. It was observed that the combination of Reed-Solomon and convolutional coding provides better BER performance compared to other two coding techniques. Section 5.4 showed how changing the angle of orientation between the source and the receiver affects the BER performance of the VLC system. It was noted that increasing the angle of orientation causes the BER performance of the VLC system to degrade. The section also showed how changing the effective area of the receiver affects the BER performance. It was observed that by increasing the effective area of signal reception, the BER performance increases as more signal

are captured by the receiver. Sections 5.5 and 5.6 showed the effects of joint soft decision decoding at the convolutional decoder and how increasing the angle of orientation or decreasing the effective area of the receiver on the BER performance. The effects of joint hard decision decoding at both the convolutional and the Reed-Solomon decoders while varying the angle of orientation or the effective area of the receiver affect the BER performance were studied in Sections 5.7 and 5.8. From the scenarios investigated in these sections for JHDD, it was observed that best BER performance was obtained when joint decoding is applied at the convolutional decoder while keeping the angle of orientation at 0° . In Section 5.9, the analysis of the simulation results was presented. And finally in Section 5.10, analysis of the decoding complexities that are associated with both convolutional and Reed-Solomon decoding in terms of the numbers of additive and multiplicative operations that are performed by Viterbi and Berlekamp-Massey algorithms in carrying out convolutional and Reed-Solomon decoding was presented.

Chapter 6

CONCLUSIONS AND FUTURE WORK

The PLC technology has the potential to become a successful and widespread technology that can be used for high-speed broadband Internet and network applications. However, it suffers from serious channel impairments such as noise, attenuation, interference etc. The VLC network despite being an emerging technology is fast gaining momentum in digital communication and has been used in many indoor applications. The visible light spectrum has range bandwidth that can be used to relieve the crowded radio frequency (RF) spectrum [28]. The combination of the PLC and the VLC networks can be used to harness the advantages of both systems with the PLC system acting as the backbone for the VLC system. The joint decoding of a parallel PLC-VLC system at the inner or outer decoder to improve system performance in terms of BER and decoding complexity has been considered in this dissertation. In the later parts of this dissertation, the problems affecting the combination of PLC and wireless systems and the PLC and the VLC systems were studied. Furthermore, the system model that was adopted in this research and joint decoding scenarios were presented.

6.1 Summary of Results

In carrying out this research investigation, the aim was to identify and complete specific tasks that are fundamental in achieving the overall research objective, which is to

improve the overall system performance in terms of BER and computational complexity using joint decoding technique. To achieve this objective, the effects of applying a joint soft decision decoding technique at the inner decoder and a joint hard decision decoding technique at the inner or outer decoder in terms of BER and computational complexity have to be identified. Hence, the conclusion made in this dissertation will be based on the observed effects. The tasks that are completed to achieve the primary objective of this research investigation are summarized as follows:

- First, applications that have utilized the joint decoding technique were reviewed in Chapter 2. The topologies, structures and physical properties of these applications were studied. It was shown through their simulation results and analysis that joint decoding technique has a great potential to produce significant gain in the overall system performance. Furthermore, it was observed that this technique significantly improved the spectral efficiency, signal quality and BER.

Indoor applications that have deployed the combination of VLC and Wi-Fi networks, PLC and wireless systems, and PLC and VLC systems were also reviewed in this chapter. In these applications, either the Wi-Fi or the PLC system is used as the uplink system and the VLC system is used as the downlink system to increase the overall network capacity. In this research work, the serial combination of the PLC and Wi-Fi systems, and the PLC and VLC networks were presented as well as the parallel combination of the PLC and Wi-Fi systems. To overcome deficiencies such as low data security, limited bandwidth and high channel interference encountered in the Wi-Fi system, the VLC system was used to replace the Wi-Fi system giving rise to the serial concatenation of the PLC and the VLC systems in many applications. The problems associated with this topology such as double attenuation and complete failure of the entire system due to breakdown of one system can be overcome by adopting parallel combination. The parallel combination of the PLC and the Wi-Fi systems presented in this dissertation utilized the joint hard decision decoding technique to recover the transmitted information at the receiver. It was observed through simulation results that these combinations

improved the overall system performance in terms of BER, throughput and implementation complexity.

- In Chapter 3, the system model that was used in this research was presented and thoroughly discussed. It was shown that the physical layers (PLC and VLC) were adopted according to PLC G3 system model and the operational mechanism and components of PLC G3 physical layer were studied. Furthermore, the OFDM modulation scheme was selected for both PLC and VLC systems, due to its outstanding advantages. In addition to robustness against multipath and frequency selectivity, OFDM reduces the effect of impulsive noise by spreading its effect over multiple symbols. When combined with adaptive modulation techniques, the performance and efficiency of OFDM based systems can be significantly improved. The DCO-OFDM system was used in the VLC channel to allow only for transmission of positive signals across the channel. The PLC channel was modeled as AWGN channel with impulsive noise distribution. The impulsive noise was modeled as Middleton Class-A noise model. The VLC channel was modeled as AWGN channel with LOS propagation effect. Special attention was paid to how changes in the angle of orientation and effective area of the receiver affect the channel behavior in terms of BER.
- The application of joint decoding technique and joint decoding scenarios were considered in Chapter 4. It was shown that joint decoding was applied either at the inner or at the outer decoder depending on whether either JSDD or JHDD is required. To implement the joint decoding, the Viterbi and the Berlekamp-Massey decoding algorithms were used at the inner and outer decoders respectively. A thorough study of these algorithms was presented and the chapter concluded with the demonstration of joint decoding scenarios. It was shown that JSDD was only performed at the inner decoder while JHDD was performed at both inner and outer decoders. It was also demonstrated how joint decoding was performed at different positions at the receiver based on changes in angle of orientation and effective area of the receiver.

- Chapter 5 of this dissertation presented the simulation results for joint decoding technique according to scenarios outlined in Chapter 4. Simulation results were obtained for two cases: increase in the angle of orientation and increase in the effective area of the receiver. Each case was further developed into different scenarios for JSDD or JHDD. The BER performance of VLC and joint decoded systems shows that increasing the angle of orientation affects both systems negatively while increasing the effective area of the receiver improves the performance of both systems.

In conclusion, the specific tasks that needed to be completed in order to answer the research question stated in Section 1.4 were successfully achieved. In Chapter 2, a technical review of applications that have utilized joint decoding technique, serial and parallel combinations was presented. It was shown that joint decoding technique improves the overall system performance in terms of spectral efficiency, signal quality and BER. It was also shown that parallel combination offers more communication advantages compared to serial combination that suffers double attenuation and dependence of one system on the other. The knowledge gained from these reviews showed that by adopting parallel combination and applying joint decoding technique at the receiver, the BER performance can be significantly improved. The system model that was adopted in this research work was presented and properly described in Chapter 3. The different components that make up the physical layer were explained and the channel model for both the PLC and the VLC channels were technically presented. The knowledge gained from this chapter enabled the exploitation of the adopted physical layer to improve transmission across the two distinct channels. The Chapter 4 clearly presented the joint decoding technique adopted in this investigation and the joint decoding scenarios regarding the application of joint decoding technique. These scenarios were then used in Chapter 5 to carry out the simulations. The simulation results were clearly presented and technical result analysis was provided. The simulation results showed that the quality of the signal captured at the receiver varies according to the angle of orientation, distance of separation between the source and the receiver, and the effective area of the receiver. Based on these three factors, the joint decoding technique was then applied at different

positions at the receiver and the results showed that joint soft decision decoding outperforms the joint hard decision decoding. Thus, it can be concluded that this research investigation has successfully met the overall objective that was set in Chapter 1. This claim is supported by the simulation results presented in Chapter 5 of this dissertation. These results conclusively showed that the joint decoding technique can be used to improve the BER performance of a parallel PLC-VLC system with significant reduction in BER depending on the angle of orientation, distance of separation between the source and the receiver, and the effective area of the receiver. Furthermore, the best BER performance is obtained when SDD is used to perform joint decoding at the inner decoder at a distance of approximately 1 mm^2 from the source with a perfect LOS between the source and the receiver and capturing the incident signal power at the maximum effective area at the receiver.

6.2 Recommendations for Future Work

The work presented in this research can be extended through further research as follows:

- LOS propagation model was presented in the Chapter 3 of this dissertation. More research can be conducted by considering non-LOS propagation model where multitude of factors such as the reflectivity of the ceiling, walls and objects within the room can be considered in addition to the position and orientation of the transmitter and receiver and room dimensions as considered in this research work.
- In this research, the concept of concatenated codes in the form of convolutional and Reed-Solomon codes for the inner and outer decoders respectively was adopted. However, in Chapter 4, only SDD of convolutional codes was used in performing the joint decoding technique. This work can be extended to the SDD of the Reed-Solomon codes.
- The results obtained in this research are based on computer simulations using widely-accepted noise models to represent both the PLC and VLC channels. This

approach can be extended by conducting practical measurements on actual power line networks and indoor room environment. This will provide an additional tool necessary to verify the practicality of the existing techniques.

The system model and the joint decoding techniques presented in this dissertation are very useful many indoor applications that operate at narrowband speed. The joint decoding technique can be adopted in both image and video processing to reduce blurring effect in order to improve both image and video quality. Due to existence of power lines in almost every home networks, parallel combination of the PLC and the VLC systems can be very useful in locations where the effect of EMI is of major concern. In the hospitals, it can be used to perform MRI and e-health in order to enhance diagnosis, and inside aircraft to enable communications. This technique is also very useful in smart house lighting and indoor positioning systems to improve system efficiency. Furthermore, it can be used in the intelligent transport systems to improve inter vehicle communication and communication between aircrafts or trains and the control station. The technique presented in this dissertation can also be useful in street lighting, sign boards, airports, cinemas, hotels, traffic lights etc. All these areas of application make the importance of the outcomes of this research investigation more appealing and should be exploited in digital communication to enhance the overall system performance.

Bibliography

- [1] W. Commons. “Li - Fi: Wikimedia Commons - the free media repository.”, 2016. URL <http://www.commons.wikimedia.org>.
- [2] S. W. Lai and G. G. Messier. “Using the Wireless and PLC Channels for Diversity.” *IEEE Transactions on Communications*, vol. 60, no. 12, pp. 3865–3875, December 2012.
- [3] S. W. Lai, N. Shabehpour, G. G. Messier, and L. Lampe. “Performance of wireless/power line media diversity in the office environment.” In *2014 IEEE Global Communications Conference*, pp. 2972–2976. Dec 2014.
- [4] E. E. utility company (ERDF). “PLC G3 Physical Layer Specification,â€” Proj. PLC G3 OFDM.” pp. 1–46. 2009. URL <http://scholar.google.com/scholar?hl=en&btnG=Search&q=intitle:PLC+G3+Physical+Layer+Specification#5>.
- [5] R. A. Baby. “Convolution coding and applications: A performance analysis under AWGN channel.” In *2015 International Conference on Communication Networks (ICCN)*, pp. 84–88. Nov 2015.
- [6] T. Kharagpur. “Lesson 35: Convolutional Codes.”, 2005. URL <http://www.nptel.ac.in/courses/117105077/pdf-m-6/m6l35.pdf>.
- [7] C. Langton. “Coding and decoding with Convolutional Codes - Tutorial 12.”, July 1999. URL <http://www.complextoreal.com/chapters/convo.pdf>.
- [8] M. 6.02. “CHAPTER 6 Linear Block Codes : Encoding and Syndrome Decoding.”, Oct 2010. URL <http://web.mit.edu/6.02/www/s2012/index.shtml>.

- [9] K. Razazian, M. Umari, A. Kamalizad, V. Loginov, and M. Navid. “G3-PLC specification for powerline communication: Overview, system simulation and field trial results.” In *ISPLC2010*, pp. 313–318. March 2010.
- [10] M. S. A. Ul Haque and F. Siddiqui. “Comparative Study of BPSK and QPSK for Wireless Networks over NS2.” *International Journal of Computer Applications*, vol. 41, no. 19, pp. 8–12, 2012.
- [11] M. F. Sanya, C. Aupetit-Berthelemot, L. Djogbe, and A. Vianou. “Diversity-Combining in asymmetrically clipped optical OFDM for PON IM/DD fiber link.” In *2014 IEEE International Conference on Communications Workshops (ICC)*, pp. 403–406. June 2014.
- [12] T. Shongwe, A. J. H. Vinck, and H. C. Ferreira. “On impulse noise and its models.” In *18th IEEE International Symposium on Power Line Communications and Its Applications*, pp. 12–17. March 2014.
- [13] H. C. Y. Qiu and W. Meng. “Channel modeling for visible light communications - a survey.” *Wireless Communications and Mobile Computing*, pp. 421–430, Sept 2015. URL <http://eprints.soton.ac.uk/266684/>.
- [14] K. Lee, H. Park, and J. R. Barry. “Indoor Channel Characteristics for Visible Light Communications.” *IEEE Communications Letters*, vol. 15, no. 2, pp. 217–219, February 2011.
- [15] MIT. “Viterbi Decoding of Convolutional Codes.”, October 2010. URL <http://www.staff@mit.edu>.
- [16] P. Farrell. “Convolutional Codes.”, 2006. URL <http://www.wireless.ece.ufl.edu/eel6509/lectures/ConvCodes.pdf>.
- [17] D. F. Yuan, A. Sui, and F. Zhang. “Soft decision decoding of punctured convolutional codes in Rayleigh fading channels.” In *IEEE APCCAS 2000. 2000 IEEE Asia-Pacific Conference on Circuits and Systems. Electronic Communication Systems. (Cat. No.00EX394)*, pp. 22–24. 2000.

- [18] P. Dayal and R. K. Patial. "Implementation of Reed-Solomon CODEC for IEEE 802.16 network using VHDL code." In *2014 International Conference on Reliability Optimization and Information Technology (ICROIT)*, pp. 452–455. Feb 2014.
- [19] Z. Sadowski. "Comparison of PLC-PRIME and PLC-G3 protocols." In *2015 International School on Nonsinusoidal Currents and Compensation (ISNCC)*, pp. 1–6. June 2015.
- [20] M. Yigit, V. C. Gungor, G. Tuna, M. Rangoussi, and E. Fadel. "Power line communication technologies for smart grid applications: A review of advances and challenges." *Computer Networks*, vol. 70, no. Supplement C, pp. 366 – 383, 2014. URL <http://www.sciencedirect.com/science/article/pii/S1389128614002369>.
- [21] S. V. Nagaraj and A. Alimohammad. "Soft-decision decoding of convolutional codes with square-law detectors." *IET Communications*, vol. 7, no. 10, pp. 966–972, July 2013.
- [22] L. Cheng. "A Short Course on Error Control Coding.", October 2010.
- [23] N. Chen and Z. Yan. "Complexity Analysis of Reed Solomom Decoding over GF (2m) Without Using Syndromes." *Signal Processing Systems*, pp. 1–10, Oct 2007.
- [24] N. K. Ram Krishna, R.K. Siddhatha and G. Jogi. "Broadband over power lines (bpl)." 2007.
- [25] T. Zhang and W. Liu. "FFT-Based OFDM in Broadband-PLC and Narrowband-PLC." In *2012 International Conference on Cyber-Enabled Distributed Computing and Knowledge Discovery*, pp. 473–478. Oct 2012.
- [26] A. Pittolo and A. M. Tonello. "Physical layer security in power line communication networks: an emerging scenario, other than wireless." *IET Communications*, vol. 8, no. 8, pp. 1239–1247, May 2014.
- [27] H. C. Ferreira, L. Lampe, J. Newbury, and T. G. Swart, editors. *Power Line Communications: Theory and Appl. for Narrowband and Broadband Communications over Power Lines*. Wiley, 1st ed., 2010.

- [28] A. R. Ndjiongue, H. C. Ferreira, K. Ouahada, and A. J. H. Vinckz. “Low-complexity SOCPBFSK-OOK interface between PLC and VLC channels for low data rate transmission applications.” In *18th IEEE International Symposium on Power Line Communications and Its Applications*, pp. 226–231. March 2014.
- [29] K. Lee and H. Park. “Channel model and modulation schemes for visible light communications.” In *2011 IEEE 54th International Midwest Symposium on Circuits and Systems (MWSCAS)*, pp. 1–4. Aug 2011.
- [30] A. R. Ndjiongue, H. C. Ferreira, and T. M. N. Ngatched. “Visible Light Communications (VLC) Technology.” *Wiley Encyclopedia of Electrical and Electronics Engineering*, pp. 1–15, 2015.
- [31] J. Grubor, S. Randel, K. D. Langer, and J. W. Walewski. “Broadband Information Broadcasting Using LED-Based Interior Lighting.” *Journal of Lightwave Technology*, vol. 26, no. 24, pp. 3883–3892, Dec 2008.
- [32] Y. Z. M. Saadi, L. Wattisuttikulkiy and P. Sangwongngam. “Visible Light Communication : Opportunities , Challenges and Channel Models.” *International Journal of Electronics & Informatics (IJEI)*, vol. 2, no. 1, pp. 1–11, Sept 2013. URL <http://www.ije.org>.
- [33] W. Ding, F. Yang, H. Yang, J. Wang, X. Wang, X. Zhang, and J. Song. “A hybrid power line and visible light communication system for indoor hospital applications.” *Computers in Industry*, vol. 68, pp. 170–178, Feb 2015.
- [34] J. Song, W. Ding, F. Yang, H. Yang, B. Yu, and H. Zhang. “An Indoor Broadband Broadcasting System Based on PLC and VLC.” *IEEE Transactions on Broadcasting*, vol. 61, no. 2, pp. 299–308, June 2015.
- [35] M. J. Ball and J. Lillis. “E-health: Transforming the physician/patient relationship.” *International Journal of Medical Informatics*, 2001.
- [36] H. Ma, L. Lampe, and S. Hranilovic. “Integration of indoor visible light and power line communication systems.” In *2013 IEEE 17th International Symposium on Power Line Communications and Its Applications*, pp. 291–296. March 2013.

- [37] J. N. Laneman, E. Martinian, G. W. Wornell, and J. G. Apostolopoulos. "Source-channel diversity for parallel channels." *IEEE Transactions on Information Theory*, vol. 51, no. 10, pp. 3518–3539, Oct 2005.
- [38] R. Liu, P. Spasojevic, and E. Soljanin. "Reliable channel regions for good binary codes transmitted over parallel channels." *IEEE Transactions on Information Theory*, vol. 52, no. 4, pp. 1405–1424, April 2006.
- [39] I. Sason and I. Goldenberg. "Coding for Parallel Channels: Gallager Bounds and Applications to Turbo-Like Codes." *IEEE Transactions on Information Theory*, vol. 53, no. 7, pp. 2394–2428, July 2007.
- [40] S. Vangala and H. Pishro-Nik. "A Highly Reliable FSO/RF Communication System Using Efficient Codes." In *IEEE GLOBECOM 2007 - IEEE Global Telecommunications Conference*, pp. 2232–2236. Nov 2007.
- [41] A. Abdulhusein, A. Oka, T. T. Nguyen, and L. Lampe. "Rateless coding for hybrid free-space optical and radio-frequency communication." *IEEE Transactions on Wireless Communications*, vol. 9, no. 3, pp. 907–913, March 2010.
- [42] C. Häfner, A. G. i. Amat, A. Alvarado, F. Brännström, and E. Agrell. "Optimized bit mappings for spatially coupled LDPC codes over parallel binary erasure channels." In *2014 IEEE International Conference on Communications (ICC)*, pp. 2064–2069. June 2014.
- [43] J. Song, S. Liu, G. Zhou, B. Yu, W. Ding, F. Yang, H. Zhang, X. Zhang, and A. Amara. "A cost-effective approach for ubiquitous broadband access based on hybrid PLC-VLC system." In *2016 IEEE International Symposium on Circuits and Systems (IS-CAS)*, pp. 2815–2818. May 2016.
- [44] A. R. Ndjiongue, T. Shongwe, H. C. Ferreira, T. M. N. Ngatched, and A. J. H. Vinck. "Cascaded PLC-VLC Channel Using OFDM and CSK Techniques." In *2015 IEEE Global Communications Conference (GLOBECOM)*, pp. 1–6. Dec 2015.

- [45] T. Komine and M. Nakagawa. “Integrated system of white LED visible-light communication and power-line communication.” *IEEE Transactions on Consumer Electronics*, vol. 49, no. 1, pp. 71–79, Feb 2003.
- [46] H. Ma, L. Lampe, and S. Hranilovic. “Subcarrier allocation in hybrid visible light and power line communication system.” In *2016 IEEE International Symposium on Circuits and Systems (ISCAS)*, pp. 2819–2822. May 2016.
- [47] N. Cen, Z. Guan, and T. Melodia. “Joint decoding of independently encoded compressive multi-view video streams.” In *2013 Picture Coding Symposium (PCS)*, pp. 341–344. Dec 2013.
- [48] A. Grant. “Joint decoding and channel estimation for linear MIMO channels.” In *2000 IEEE Wireless Communications and Networking Conference. Conference Record (Cat. No.00TH8540)*, vol. 3, pp. 1009–1012 vol.3. 2000.
- [49] C. Schlegel, D. Truhachev, and Ł. Krzymie. “On Joint Decoding and Random CDMA Demodulation.” *Computer Engineering*.
- [50] T. Yabe, M. Inamori, and Y. Sanada. “Experimental investigation of joint decoding in overloaded MIMO-OFDM system.” In *2013 International Symposium on Intelligent Signal Processing and Communication Systems*, pp. 585–589. Nov 2013.
- [51] Y. Sanada. “Performance of joint maximum-likelihood decoding for block coded signal streams in overloaded MIMO-OFDM system.” In *2013 International Symposium on Intelligent Signal Processing and Communication Systems*, pp. 775–780. Nov 2013.
- [52] O. A. Gonzalez, J. Urminsky, M. Calvo, and L. de Haro. “Performance analysis of hybrid broadband access technologies using PLC and Wi-Fi.” In *2005 International Conference on Wireless Networks, Communications and Mobile Computing*, vol. 1, pp. 564–569 vol.1. June 2005.
- [53] P. Wang, A. Marshall, K. A. Noordin, X. Huo, and G. Markarian. “Hybrid network combining PLC and IEEE802.16 for hospital environment.” In *ISPLC2010*, pp. 267–272. March 2010.

- [54] G. Bianchi, L. Fratta, and M. Oliveri. “Performance evaluation and enhancement of the CSMA/CA MAC protocol for 802.11 wireless LANs.” In *Personal, Indoor and Mobile Radio Communications, 1996. PIMRC’96., Seventh IEEE International Symposium on*, vol. 2, pp. 392–396 vol.2. Oct 1996.
- [55] C. Barney, A. Dich, and D. Koufos. “Visible Light Communication Systems: A Major Qualifying Project Report:.”, March 2014.
- [56] S. Shao, A. Khreishah, M. Ayyash, M. B. Rahaim, H. Elgala, V. Jungnickel, D. Schulz, T. D. C. Little, J. Hilt, and R. Freund. “Design and analysis of a visible-light-communication enhanced WiFi system.” *IEEE/OSA Journal of Optical Communications and Networking*, vol. 7, no. 10, pp. 960–973, October 2015.
- [57] Z. He, S. Roy, and P. Fortier. “FPGA Implementation of LDPC Decoders Based on Joint Row-column Decoding Algorithm.” In *2007 IEEE International Symposium on Circuits and Systems*, pp. 1653–1656. May 2007.
- [58] F. Daneshgaran, M. Laddomada, and M. Mondin. “Iterative joint channel decoding of correlated sources employing serially concatenated convolutional codes.” *IEEE Transactions on Information Theory*, vol. 51, no. 7, pp. 2721–2731, July 2005.
- [59] S. Shao, A. Khreishah, M. B. Rahaim, H. Elgala, M. Ayyash, T. D. C. Little, and J. Wu. “An Indoor Hybrid WiFi-VLC Internet Access System.” In *2014 IEEE 11th International Conference on Mobile Ad Hoc and Sensor Systems*, pp. 569–574. Oct 2014.
- [60] A. R. Ndjiongue, H. Ferreira, J. Song, F. Yang, and L. Cheng. “Hybrid PLC-VLC Channel Model and Spectral Estimation Using a Non-Parametric Approach.” vol. 28, July 2017.
- [61] M. S. Yousuf, S. Z. Rizvi, and M. El-Shafei. “Power Line Communications: An Overview - Part II.” In *2008 3rd International Conference on Information and Communication Technologies: From Theory to Applications*, pp. 1–6. April 2008.
- [62] ERDF. “Electricity metering - Data exchange over powerline – Part 2 : Lower layer profile using OFDM modulation type 2.” pp. 1–144, April 2011. URL <http://www.openmeter.com>.

- [63] J. M. Tang, P. M. Lane, and K. A. Shore. "Transmission performance of adaptively modulated optical OFDM signals in multimode fiber links." *IEEE Photonics Technology Letters*, vol. 18, no. 1, pp. 205–207, Jan 2006.
- [64] J. Armstrong. "OFDM for Optical Communications." *Journal of Lightwave Technology*, vol. 27, no. 3, pp. 189–204, Feb 2009.
- [65] J. Haring and A. Vinck. "OFDM transmission corrupted by impulsive noise."
- [66] O. G. Hooijen. "A channel model for the residential power circuit used as a digital communications medium." *IEEE Transactions on Electromagnetic Compatibility*, vol. 40, no. 4, pp. 331–336, Nov 1998.
- [67] C. Chauvenet, G. Etheve, M. Sedjai, and M. Sharma. "G3-PLC based IoT sensor networks for SmartGrid." In *2017 IEEE International Symposium on Power Line Communications and its Applications (ISPLC)*, pp. 1–6. April 2017.
- [68] S. A. Bhatti, Q. Shan, I. A. Glover, R. Atkinson, I. E. Portugues, P. J. Moore, and R. Rutherford. "Impulsive noise modelling and prediction of its impact on the performance of WLAN receiver." In *2009 17th European Signal Processing Conference*, pp. 1680–1684. Aug 2009.
- [69] A. D. Familua, A. O. Qatarey, P. A. J. V. Rensburg, and L. Cheng. "Error pattern/behavior of noise in in-house CENELEC A-Band PLC channel." In *2012 IEEE International Symposium on Power Line Communications and Its Applications*, pp. 114–119. March 2012.
- [70] M. Hoch. "Comparison of PLC G3 and PRIME." In *2011 IEEE International Symposium on Power Line Communications and Its Applications*, pp. 165–169. April 2011.
- [71] A. Sanz, D. Sancho, C. Guemes, and J. A. Cortá's. "A physical layer model for G3-PLC networks simulation." In *2017 IEEE International Symposium on Power Line Communications and its Applications (ISPLC)*, pp. 1–6. April 2017.

- [72] T. Shongwe and A. J. H. Vinck. “Interleaving and nulling to combat narrow-band interference in PLC standard technologies PLC G3 and PRIME.” In *2013 IEEE 17th International Symposium on Power Line Communications and Its Applications*, pp. 258–262. March 2013.
- [73] P. Mlynek, M. Koutny, J. Misurec, and Z. Kolka. “Measurements and evaluation of PLC modem with G3 and PRIME standards for Street Lighting Control.” In *18th IEEE International Symposium on Power Line Communications and Its Applications*, pp. 238–243. March 2014.
- [74] A. D. Familua, K. Ogunyanda, T. G. Swart, H. C. Ferreira, R. V. Olst, and L. Cheng. “Narrowband PLC channel modeling using USRP and PSK modulations.” In *18th IEEE International Symposium on Power Line Communications and Its Applications*, pp. 156–161. March 2014.
- [75] K. Razazian, M. Umari, and A. Kamalizad. “Error correction mechanism in the new G3-PLC specification for powerline communication.” In *ISPLC2010*, pp. 50–55. March 2010.
- [76] U. Demir and O. Aktas. “Raptor versus Reed Solomon forward error correction codes.” In *2006 International Symposium on Computer Networks*, pp. 264–269. 2006.
- [77] T. C. Chuah. “On Reed Solomon Coding for Data Communications Over Power-Line Channels.” *IEEE Transactions on Power Delivery*, vol. 24, no. 2, pp. 614–620, April 2009.
- [78] F. Daneshgaran, M. Laddomada, and M. Mondin. “Interleaver design for serially concatenated convolutional codes: theory and application.” *IEEE Transactions on Information Theory*, vol. 50, no. 6, pp. 1177–1188, June 2004.
- [79] M. Cao, K. R. Subramanian, and V. K. Dubey. “Optimal interleaver design for concatenated coding in DSL systems.” *Electronics Letters*, vol. 35, no. 19, pp. 1630–1631, Sep 1999.

- [80] I. C. Society. "IEEE Standard for Broadband over Power Line Networks: Medium Access Control and Physical Layer Specifications." *IEEE Std 1901-2010*, pp. 1–1586, Dec 2010.
- [81] B. Fong, P. B. Rapajic, G. Y. Hong, and A. C. M. Fong. "Forward error correction with Reed-Solomon codes for wearable computers." *IEEE Transactions on Consumer Electronics*, vol. 49, no. 4, pp. 917–921, Nov 2003.
- [82] T. Lerner. "Analysis of Digital Communications Systems Using Binary Error Correcting Codes." *IEEE Transactions on Communication Technology*, vol. 15, no. 1, pp. 17–22, February 1967.
- [83] J. Massey. "Step-by-step decoding of the Bose-Chaudhuri-Hocquenghem codes." *IEEE Transactions on Information Theory*, vol. 11, no. 4, pp. 580–585, October 1965.
- [84] S.-W. Wei and C.-H. Wei. "High-speed decoder of Reed-Solomon codes." *IEEE Transactions on Communications*, vol. 41, no. 11, pp. 1588–1593, Nov 1993.
- [85] G. Forney. "Burst-Correcting Codes for the Classic Bursty Channel." *IEEE Transactions on Communication Technology*, vol. 19, no. 5, pp. 772–781, October 1971.
- [86] T. Agrawal, A. Kumar, and S. K. Saraswat. "Comparative analysis of convolutional codes based on ML decoding." In *2016 2nd International Conference on Communication Control and Intelligent Systems (CCIS)*, pp. 41–45. Nov 2016.
- [87] A. Babu. "From Convolutional Codes To Turbo Codes.", Jan 2015.
- [88] Y. Aikawa and H. Uenohara. "Demonstration of Optical FEC Coding Scheme With Convolutional Code Consisting of a Signal Source." *IEEE Photonics Technology Letters*, vol. 29, no. 1, pp. 165–168, Jan 2017.
- [89] E. Krouk and S. Semenov. *Convolutional Codes and Turbo Codes*, pp. 680–700. Wiley Telecom, 2011. URL <http://ieeexplore.ieee.org/xpl/articleDetails.jsp?arnumber=8043357>.

- [90] E. Liu. “Convolutional Coding & Viterbi Algorithm.” *Postgraduate Seminar on Radio Communications*, pp. 1–17, Nov 2004. URL http://www.comlab.hut.fi/opetus/333/2004_2005_slides/Convolutional_Coding_Viterbi_Algorithm.pdf.
- [91] B. Tahir, S. Schwarz, and M. Rupp. “BER comparison between Convolutional, Turbo, LDPC, and Polar codes.” In *2017 24th International Conference on Telecommunications (ICT)*, pp. 1–7. May 2017.
- [92] M. Ndlovu and L. Cheng. “An OFDM inter-subcarrier permutation coding scheme for power-line communication.” In *18th IEEE International Symposium on Power Line Communications and Its Applications*, pp. 196–201. March 2014.
- [93] T. Murakawa, G. Cincotti, S. Shimizu, T. Nagashima, M. Hasegawa, K. Hattori, M. Okuno, S. Mino, A. Himeno, N. Wada, H. Uenohara, and T. Konishi. “Fractional OFDM based transmitter and receiver for time/frequency multiplexing in gridless, elastic networks.” In *2015 Optical Fiber Communications Conference and Exhibition (OFC)*, pp. 1–3. March 2015.
- [94] K. Al-majdi, R. S. Al-moussawy, and L. A. Hasan. “Reed Solomon Coding in Orthogonal Frequency Division Multiplexing (OFDM) Communication Systems.” *Journal of Engineering and Development*, vol. 16, no. 3, pp. 162–174, Sept 2012.
- [95] A. Mecwan and D. Shah. “Implementation of OFDM transceiver on FPGA.” In *2013 Nirma University International Conference on Engineering (NUiCONE)*, pp. 1–5. Nov 2013.
- [96] L. Zou. “Detection of the guard interval length in OFDM systems.” In *CCNC 2006. 2006 3rd IEEE Consumer Communications and Networking Conference, 2006.*, vol. 2, pp. 1048–1051. Jan 2006.
- [97] A. H. Najarkolaei, W. Hosny, and J. Lota. “Bit Error Rate Performance in Power Line Communication Channels with Impulsive Noise.” In *2015 17th UKSim-AMSS International Conference on Modelling and Simulation (UKSim)*, pp. 248–251. March 2015.

- [98] J. Armstrong and B. J. C. Schmidt. "Comparison of Asymmetrically Clipped Optical OFDM and DC-Biased Optical OFDM in AWGN." *IEEE Communications Letters*, vol. 12, no. 5, pp. 343–345, May 2008.
- [99] M. A. Khan, S. Pal, and A. Jose. "BER Performance of BPSK , QPSK & 16 QAM with and without using OFDM over AWGN , Rayleigh and Rician Fading Channel." vol. 4, no. 7, pp. 64–69, 2015.
- [100] V. Valenta. "Performance of BPSK and QPSK in Satellite Communications." URL <http://www.xvalen07@stud.feec.vutbr.cz>.
- [101] C. Langton. "All About Modulation - Part I Basic Concepts of modulation.", 2002. URL <http://www.complextoreal.com>.
- [102] S. Loyka. "Differential Phase Shift Keying (DPSK)." *ELG4179: Wireless Communication Fundamentals*, vol. 5, no. 4, pp. 1–26, Oct 2013.
- [103] J. Armstrong and A. J. Lowery. "Power efficient optical OFDM." *Electronics Letters*, vol. 42, no. 6, pp. 370–372, March 2006.
- [104] M. F. Sanya, C. Aupetit-Berthelemot, L. Djogbe, and A. Vianou. "D-C ACO-OFDM and DCO-OFDM for passive optical network: Performance comparison in IM/DD fiber link." In *2014 23rd Wireless and Optical Communication Conference (WOCC)*, pp. 1–5. May 2014.
- [105] S. D. Dissanayake and J. Armstrong. "Comparison of ACO-OFDM, DCO-OFDM and ADO-OFDM in IM/DD Systems." *Journal of Lightwave Technology*, vol. 31, no. 7, pp. 1063–1072, April 2013.
- [106] L. A. Berry. "Understanding Middleton's Canonical Formula for Class a Noise." *IEEE Transactions on Electromagnetic Compatibility*, vol. EMC-23, no. 4, pp. 337–344, Nov 1981.
- [107] J. Haring and A. J. H. Vinck. "Iterative decoding of codes over complex numbers for impulsive noise channels." *IEEE Transactions on Information Theory*, vol. 49, no. 5, pp. 1251–1260, May 2003.

- [108] M. Zimmermann and K. Dostert. “A multipath model for the powerline channel.” *IEEE Transactions on Communications*, vol. 50, no. 4, pp. 553–559, Apr 2002.
- [109] M. Tlich, A. Zeddou, F. Moulin, and F. Gauthier. “Indoor Power-Line Communications Channel Characterization up to 100 MHz; Part II: Time-Frequency Analysis.” *IEEE Transactions on Power Delivery*, vol. 23, no. 3, pp. 1402–1409, July 2008.
- [110] S. Galli. “A simplified model for the indoor power line channel.” In *2009 IEEE International Symposium on Power Line Communications and Its Applications*, pp. 13–19. March 2009.
- [111] S. Miyamoto, M. Katayama, and N. Morinaga. “Performance analysis of QAM systems under class A impulsive noise environment.” *IEEE Transactions on Electromagnetic Compatibility*, vol. 37, no. 2, pp. 260–267, May 1995.
- [112] R. Haring and A. J. H. Vinck. “Performance bounds for optimum and suboptimum reception under Class-A impulsive noise.” *IEEE Transactions on Communications*, vol. 50, no. 7, pp. 1130–1136, Jul 2002.
- [113] K. C. Wiklundh, P. F. Stenumgaard, and H. M. Tullberg. “Channel capacity of Middleton’s class A interference channel.” *Electronics Letters*, vol. 45, no. 24, pp. 1227–1229, November 2009.
- [114] J. A. Cortés, A. Sanz, P. Estopiñán, and J. I. García. “On the suitability of the Middleton class A noise model for narrowband PLC.” In *2016 International Symposium on Power Line Communications and its Applications (ISPLC)*, pp. 58–63. March 2016.
- [115] F. Rouissi, A. J. H. Vinck, H. Gassara, and A. Ghazel. “Statistical characterization and modelling of impulse noise on indoor narrowband PLC environment.” In *2017 IEEE International Symposium on Power Line Communications and its Applications (ISPLC)*, pp. 1–6. April 2017.
- [116] G. Ndo, F. Labeau, and M. Kassouf. “A Markov-Middleton Model for Bursty Impulsive Noise: Modeling and Receiver Design.” *IEEE Transactions on Power Delivery*, vol. 28, no. 4, pp. 2317–2325, Oct 2013.

- [117] W. Viriyasitavat, S. H. Yu, and H. M. Tsai. “Short paper: Channel model for visible light communications using off-the-shelf scooter taillight.” In *2013 IEEE Vehicular Networking Conference*, pp. 170–173. Dec 2013.
- [118] J. K. Kim and E. F. Schubert. “III-Nitride light-emitting diodes for solid state lighting revolution.” In *2009 Asia Communications and Photonics conference and Exhibition (ACP)*, pp. 1–2. Nov 2009.
- [119] J. M. Geusebroek, R. van den Boomgaard, A. W. M. Smeulders, and H. Geerts. “Color invariance.” *IEEE Transactions on Pattern Analysis and Machine Intelligence*, vol. 23, no. 12, pp. 1338–1350, Dec 2001.
- [120] H. L. Minh, D. O’Brien, G. Faulkner, L. Zeng, K. Lee, D. Jung, Y. Oh, and E. T. Won. “100-Mb/s NRZ Visible Light Communications Using a Postequalized White LED.” *IEEE Photonics Technology Letters*, vol. 21, no. 15, pp. 1063–1065, Aug 2009.
- [121] T. Komine and M. Nakagawa. “Fundamental analysis for visible-light communication system using LED lights.” *IEEE Transactions on Consumer Electronics*, vol. 50, no. 1, pp. 100–107, Feb 2004.
- [122] K. Lee and H. Park. “Channel model and modulation schemes for visible light communications.” In *2011 IEEE 54th International Midwest Symposium on Circuits and Systems (MWSCAS)*, pp. 1–4. Aug 2011.
- [123] F. R. Gfeller and U. Bapst. “Wireless in-house data communication via diffuse infrared radiation.” *Proceedings of the IEEE*, vol. 67, no. 11, pp. 1474–1486, Nov 1979.
- [124] M. Arai, A. Yamamoto, A. Yamaguchi, S. Fukumoto, and K. Iwasaki. “Analysis of using convolutional codes to recover packet losses over burst erasure channels.” In *Proceedings 2001 Pacific Rim International Symposium on Dependable Computing*, pp. 258–265. 2001.
- [125] J. Justesen. “On the complexity of decoding Reed-Solomon codes.” *IEEE Transactions on Information Theory*, vol. 22, no. 2, pp. 237–238, March 1976.

- [126] I. S. Reed, T. K. Truong, R. L. Miller, and J. P. Huang. “Fast transforms for decoding Reed-Solomon codes.” *Communications, Radar and Signal Processing, IEE Proceedings F*, vol. 128, no. 1, pp. 9–, February 1981.
- [127] L. Cheng and H. C. Ferreira. “Rate-compatible pruned convolutional codes and Viterbi decoding with the Levenshtein distance metric applied to channels with insertion, deletion, and substitution errors.” In *2004 IEEE Africon. 7th Africon Conference in Africa (IEEE Cat. No.04CH37590)*, vol. 1, pp. 137–143 Vol.1. Sept 2004.
- [128] A. A. Islamic. “Channel Coding Theory: Trellis Diagram and the Viterbi Algorithm.” pp. 1–12. URL <http://www.iugaza.edu.ps/ahdrouss/files>.
- [129] T. Panse and K. Saratkar. “Design of Trellis code modulation decoder using Hybrid Register Exchange Method.” In *2014 International Conference on Communication and Signal Processing*, pp. 265–269. April 2014.
- [130] X. Xiao, Y. Hong, E. Viterbo, and A. Gupta. “Trellis coded modulation for informed receivers.” In *2017 IEEE International Conference on Communications Workshops (ICC Workshops)*, pp. 955–960. May 2017.
- [131] Y. S. Han, P.-N. Chen, and H.-B. Wu. “A maximum-likelihood soft-decision sequential decoding algorithm for binary convolutional codes.” *IEEE Transactions on Communications*, vol. 50, no. 2, pp. 173–178, Feb 2002.
- [132] S. Jafarzadeh, M. Khatami, and F. Marvasti. “Decoding real numbered block and convolutional codes with erasure and impulsive noise channels.” In *2010 18th European Signal Processing Conference*, pp. 1419–1423. Aug 2010.
- [133] U. C. Fiebig and P. Robertson. “Soft-decision and erasure decoding in fast frequency-hopping systems with convolutional, turbo, and Reed-Solomon codes.” *IEEE Transactions on Communications*, vol. 47, no. 11, pp. 1646–1654, Nov 1999.

- [134] H. T. Wu, C. F. Wu, and W. W. Chang. “Iterative symbol decoding of variable-length codes with convolutional codes.” *Journal of Communications and Networks*, vol. 18, no. 1, pp. 40–49, Feb 2016.
- [135] C. Pimentel and L. C. Rego. “Analysis of soft decision decoding of interleaved convolutional codes over burst channels.” In *WCNC. 1999 IEEE Wireless Communications and Networking Conference (Cat. No.99TH8466)*, pp. 1090–1094 vol.3. 1999.
- [136] T. C. Hewavithana and M. Brookes. “Soft decisions for DQPSK demodulation for the Viterbi decoding of the convolutional codes.” In *Acoustics, Speech, and Signal Processing, 2003. Proceedings. (ICASSP '03). 2003 IEEE International Conference on*, vol. 4, pp. IV–17–20 vol.4. April 2003.
- [137] A. Neubauer, J. Freudenberger, and V. Kuhn. *Convolutional Codes*, pp. 362–. Wiley Telecom. URL <http://ieeexplore.ieee.org/xpl/articleDetails.jsp?arnumber=8040616>.
- [138] P. Dayal and R. Patial. “FPGA Implementation of Reed-Solomon Encoder and Decoder for Wireless Network 802 . 16.” *International Journal of Computer Applications*, vol. 68, no. 16, pp. 42–45, April 2013.
- [139] M. Shrestha and L. Xu. “Efficient Encoding for Generalized Reed Solomon Codes.” In *2011 IEEE 10th International Symposium on Network Computing and Applications*, pp. 302–305. Aug 2011.
- [140] S. Lin and D. J. Costello Jr. *Error Control Coding*. Pearson Education, Inc, 2nd ed., 2005.
- [141] B. Sklar. “Reed-Solomon Codes.” *Journal of the Society for Industrial and Applied Mathematics*, 1960.
- [142] B. Tiwari and R. Mehra. “Design and implementation of Reed Solomon Decoder for 802.16 network using FPGA.” In *2012 IEEE International Conference on Signal Processing, Computing and Control*, pp. 1–5. March 2012.

- [143] H. Matsui and S. Mita. “A New Encoding and Decoding System of Reed-Solomon Codes for HDD.” *IEEE Transactions on Magnetics*, vol. 45, no. 10, pp. 3757–3760, Oct 2009.
- [144] S.-W. Wei and C.-H. Wei. “High-speed decoder of Reed-Solomon codes.” *IEEE Transactions on Communications*, vol. 41, no. 11, pp. 1588–1593, Nov 1993.
- [145] T. C. Chen, C. H. Wei, and S. W. Wei. “Step-by-step decoding algorithm for Reed-Solomon codes.” *IEE Proceedings - Communications*, vol. 147, no. 1, pp. 8–12, Feb 2000.
- [146] R. L. Miller, T. K. Truong, and I. S. Reed. “Fast algorithm for encoding the (255, 223) Reed-Solomon code over GF(28).” *Electronics Letters*, vol. 16, no. 6, pp. 222–223, March 1980.
- [147] C. Senger, V. R. Sidorenko, S. Schober, M. Bossert, and V. V. Zyablov. “Adaptive single-trial error/erasure decoding of Reed-Solomon codes.” In *2011 12th Canadian Workshop on Information Theory*, pp. 47–51. May 2011.
- [148] S. W. Lee and B. V. K. V. Kumar. “Soft-Decision Decoding of Reed-Solomon Codes Using Successive Error-and-Erasure Decoding.” In *IEEE GLOBECOM 2008 - 2008 IEEE Global Telecommunications Conference*, pp. 1–5. Nov 2008.
- [149] W. E. Ryan and P. Conoval. “A method of analysis for interleaved Reed-Solomon coding with erasure decoding on burst error channels.” *IEEE Transactions on Communications*, vol. 41, no. 3, pp. 430–434, Mar 1993.
- [150] T.-C. Chen, C.-H. Wei, and S.-W. Wei. “Step-by-step error/erasure decoding Reed-Solomon codes.” In *The 8th International Conference on Communication Systems, 2002. ICCS 2002.*, vol. 1, pp. 322–326 vol.1. Nov 2002.
- [151] G. Forney. “On decoding BCH codes.” *IEEE Transactions on Information Theory*, vol. 11, no. 4, pp. 549–557, Oct 1965.
- [152] Z. Fei, J. Yuan, M. Xiao, B. Bai, S. Zhang, and D. Lin. “Recent development of error control codes for future communication and storage systems.” *China Communications*, vol. 14, no. 8, pp. iii–v, Aug 2017.

- [153] T. K. Moon and S. Budge. “Bit-level erasure decoding of Reed-Solomon codes over GF(2^m).” In *The Thrity-Seventh Asilomar Conference on Signals, Systems Computers, 2003*, vol. 2, pp. 1783–1787 Vol.2. Nov 2003.
- [154] M. H. L. Chan and R. W. Donaldson. “Attenuation of Communication Signals on Residential and Commercial Intrabuilding Power-Distribution Circuits.” *IEEE Transactions on Electromagnetic Compatibility*, vol. 28, no. 4, pp. 220–230, Nov 1986.
- [155] D. Duche and P. V. Gogate. “Signal Attenuation in Powerline Communication Channel AFFECTING COMMUNICATION THE.” vol. 3, no. 2, 2014.
- [156] I. H. Cavdar and E. Karadeniz. “Measurements of impedance and attenuation at CENELEC bands for power line communications systems.” *Sensors*, vol. 8, no. 12, pp. 8027–8036, 2008.
- [157] Z. Ghassemlooy, W. Popoola, and S. Rajbhandari. *Optical Wireless Communications: System and Channel Modelling with MATLAB*. 2012.
- [158] M. A. Herro, L. Hu, and J. M. Nowack. “Bit error probability calculations for convolutional codes with short constraint lengths on very noisy channels.” *IEEE Transactions on Communications*, vol. 36, no. 7, pp. 885–888, Jul 1988.
- [159] F. Chiaraluce, E. Gambi, M. Mazzone, and P. Pierleoni. “A technique to evaluate an exact formula for the bit error rate of convolutional codes in case of finite length words.” In *TENCON '97. IEEE Region 10 Annual Conference. Speech and Image Technologies for Computing and Telecommunications., Proceedings of IEEE*, vol. 1, pp. 113–116 vol.1. Dec 1997.
- [160] K. M. Cheung. “More on the decoder error probability for Reed-Solomon codes.” *IEEE Transactions on Information Theory*, vol. 35, no. 4, pp. 895–900, Jul 1989.
- [161] K.-M. Cheung and R. J. McEliece. “The undetected error probability for Reed-Solomon codes.” In *Military Communications Conference, 1988. MILCOM 88, Conference record. 21st Century Military Communications - What's Possible? 1988 IEEE*, pp. 163–167 vol.1. Oct 1988.

- [162] D. W. Matolak and S. G. Wilson. “Variable-complexity trellis decoding of binary convolutional codes.” *IEEE Transactions on Communications*, vol. 44, no. 2, pp. 121–126, Feb 1996.
- [163] V. Ponnampalam and B. Vucetic. “Soft decision decoding of Reed-Solomon codes.” *IEEE Transactions on Communications*, vol. 50, no. 11, pp. 1758–1768, Nov 2002.
- [164] G. Garrammone. “On Decoding Complexity of Reed-Solomon Codes on the Packet Erasure Channel.” *IEEE Communications Letters*, vol. 17, no. 4, pp. 773–776, April 2013.
- [165] R. W. P. Luk and R. I. Damper. “Computational complexity of a fast Viterbi decoding algorithm for stochastic letter-phoneme transduction.” *IEEE Transactions on Speech and Audio Processing*, vol. 6, no. 3, pp. 217–225, May 1998.
- [166] R. J. McEliece. “The Viterbi decoding complexity of linear block codes.” In *Proceedings of 1994 IEEE International Symposium on Information Theory*, pp. 341–. Jun 1994.
- [167] Y. Cassuto, J. Bruck, and R. J. McEliece. “On the Average Complexity of Reed-Solomon List Decoders.” *IEEE Transactions on Information Theory*, vol. 59, no. 4, pp. 2336–2351, April 2013.
- [168] T. Jokela and E. Lehtonen. “Reed-Solomon Decoding Algorithms and Their Complexities at the DVB-H Link-Layer.” In *2007 4th International Symposium on Wireless Communication Systems*, pp. 752–756. Oct 2007.
- [169] W. Jin and M. Fossorier. “Towards Maximum Likelihood Soft Decision Decoding of the (255,239) Reed Solomon Code.” *IEEE Transactions on Magnetics*, vol. 44, no. 3, pp. 423–428, March 2008.